Towards improved simulations of self-organising molecular materials

JUHO SAKARI LINTUVUORI

How to cite:

LINTUVUORI, JUHO SAKARI (2009) Towards improved simulations of self-organising molecular materials. Doctoral thesis, Durham University.

Towards improved simulations of self-organising molecular materials

Juho Sakari Lintuvuori

A Thesis is submitted in partial fulfilment of the requirements for the degree of Doctor of Philosophy

Durham
University

Department of Chemistry
University of Durham
England
Autumn 2009

Towards improved simulations of self-organising molecular materials

Juho Sakari Lintuvuori

A Thesis is submitted in partial fulfilment of the requirements for the
degree of Doctor of Philosophy
Autumn 2009

Abstract

Computer simulations can be used in parallel with experimental techniques to gain valuable insights into physical systems, test theoretical models or predict new behaviour of molecular materials. Long time and large length scales, in combination with problems of phase space sampling, present a grand challenge for simulations of self-organising molecular materials. In the work presented in this thesis, the aim has been to develop and apply new or recent simulation models and methods to address these issues, with the aim of producing improved simulations of molecular materials.

A new anisotropic model for simulating mesogenic systems has been developed, based on a soft core spherocylinder potential. This model is tested for single site systems and a multipedal liquid crystalline molecule, using conventional molecular dynamics simulations. It is used also to map out an approximate phase diagram for a main chain liquid crystalline polymer as a function of the volume fraction of the mesogenic unit; and to study the effects of a chiral medium on flexible achiral dopant molecules. Results here, show a preferential selection of conformations of similar chirality to the solvent. Later in the thesis, this new soft core spherocylinder model, is combined with a recently developed simulation methdology, Statistical Temperature Molecular Dynamics, to study the isotropic-nematic phase transition of a single site mesogen and the isotropic-lamellar phase transition of a model rod-coil diblock copolymer, using a single simulation to span the temperature window corresponding to the phase transition.

Additional simulations combine a mesoscopic simulation method, Stochastic Rotational Dynamics, with a coarse grained surfactant model. This allows a computationally efficient solvent description while maintaining correct hydrodynamics. Results presented here include the formation of a bilayer, via spontaneous self-assembly of surfactant molecules, and information on the pathways of micelle formation.

In the final result chapter of this thesis, Hamiltonian replica exchange simulations are performed employing soft-core replicas for a Gay-Berne system. The simulation results show an order of magnitude increase in equilibration speed of the ordered phase when compared to conventional simulations of a Gay-Berne fluid.

Declaration

The work in this thesis is mostly based on research carried out at University of Durham, England. Part of the research in chapters 5 and 7 has been carried out while the thesis author visited the University of Pittsburgh, USA (8 weeks) and the University of Bologna, Italy (4 weeks) as part of his Durham supervised research programme. The material contained in this thesis has not been previously submitted for any other degree at Durham or any other institution. The research within this thesis has been conducted by the author unless indicated otherwise. In chapters 5 and 7, the contributions from researchers from University of Pittsburgh and University of Bologna, are clearly indicated in the text.

Contents

List of Figures

List of Tables

Chapter 1

Introduction to self-ordering

In his book, The Physics of Liquid Crystals, [7] de Gennes gives the following description for a fourth state of the matter termed a liquid crystal: "Certain organic materials do not show a single transition from solid to liquid, but rather a cascade of transitions involving new phases; the mechanical properties and the symmetry properties of these phases are intermediate between those of a liquid and those of a crystal."

One key difference arises between the structure of a crystal and a liquid. In solid crystal, the molecules sit on a three dimensional lattice with long range periodic order. This can be observed experimentally by x-ray diffraction experiments where Bragg diffraction peaks occur when [8]

$$\lim_{|\mathbf{x}-\mathbf{x}'|\to\infty} \langle \rho(\mathbf{x})\rho(\mathbf{x}')\rangle = F(\mathbf{x}-\mathbf{x}'). \tag{1.1}$$

Here $\langle \rho(\mathbf{x})\rho(\mathbf{x}')\rangle$ is a pair correlation function and $F(\mathbf{x}-\mathbf{x}')$ is a periodic function of the lattice vectors corresponding to the crystal structure. In a liquid such long range order is missing. In an isotropic liquid the only way to describe the probability of finding similar molecules or structures at long separation is through the average particle density, $\bar{\rho}$ [8].

With the aid of these definitions, liquid crystals (LC) can be defined as systems where liquid like ordering exists at least in one dimension, and where the particle density pair correlation function is not only dependent on the distance $|\mathbf{x}-\mathbf{x}_0|$ but also on the orientation of the vector $\mathbf{x} - \mathbf{x}_0$ [8]. In addition to being intermediate states, LC mesophases have physical properties inherited from both isotropic liquids and solid crystal materials. For example, LC systems might have the ability to flow and the inability to resist stress (like an isotropic liquid) but also have the ability to transmit a torque (like a solid) [9].

Liquid crystalline systems can be roughly divided into two categories based on what acts as the driving force for phase transitions. In thermotropic liquid crystals the driving force for phase changes is provided by changes in temperature. For example, on cooling a system can move from an isotropic liquid to a nematic liquid crystal mesophase with orientational order. In lyotropic liquid crystals the changes between different mesophases are driven by a change in the concentration in addition to temperature changes.

In nature self-organisation is not only limited to liquid crystals, but is present in a wide variety of soft condensed matter systems [10, 11]. For example in a diblock copolymer system, which is the simplest case of a general block copolymer, the incompatibility of the two building blocks leads to phase segregation and to a wide cascade of different self-organised mesophases [12].

An other example of self organisation is provided by amphiphilic molecules in solution. Amphiphilic molecules (also known as surfactants) consists of hydrophobic and hydrophilic parts [11]. In aqueous solution, with favourable concentration and temperature, surfactant molecules can self-assemble to form micelles and a range of lyotropic liquid crystalline mesophases. Another example of systems exhibiting lyotropic liquid crystalline behaviour are rod like colloidal particles. For example colloidal suspension of Tobacco Mosaic virus will form liquid crystal phases at high concentration of particles.

1.1 Liquid crystalline phases

Liquid crystal particles, such as organic molecules which are able to form ordered LC mesophases, are called mesogens. Mesogens can be, very roughly, divided into two categories by their shape: calamitic (rod-like) and discotic (disc-like). Both of these classes have a strong anisotropy in molecular shape, normally thought of as a sufficient requirement for forming mesophases [9]. G. Friedel was the first to carry out a classification of different liquid crystal mesophases [13]. Liquid crystal molecules come with various chemical structures and a range of physical properties. This leads to a large number of different mesophases, some of which are very complex. Some of the most common mesophases will be discussed in more detail, in the next sections.

1.1.1 Nematic phases

The main characteristic of the nematic phase (N) is long range orientational order with a lack of long range translational order. In the uniaxial nematic phase particles are orientated such that, on average, their unique axis (long axis for calamitic mesogens figure 1.1 (b)) and short axis for discotic mesogens (figure 1.3) points in the same direction. This common direction can be identified as the director of the phase, $\hat{\mathbf{n}}$.

Normal nematics are uniaxial with one dimensional orientational symmetry. There exists also a type of nematic, which has orientational order for two unique axes, characterised as a short axis and a long axis. This type of nematic is called a biaxial nematic. It has been observed most often in lyotropic or polymeric systems, but recently it has been observed also in thermotropic systems [14–16].

1.1.2 Chiral nematic phase

A schematic representation of the chiral nematic (N^*) phase is presented in figure 1.2. In a chiral nematic phase, molecules exhibit a twist around a helical axis (dotted line in figure 1.2) perpendicular to the nematic director $\hat{\mathbf{n}}$. The twist arises from the molecules possessing a molecular chirality (normally conformational or electrostatic) inducing neighbouring molecules (on average) to align at a slight angle with respect to each other [7]. However, the existence of molecular chirality does not guarantee the formation of a chiral nematic phase. For example, for chiral tobacco mosaic virus particles [17] only a normal nematic phase is found [18].

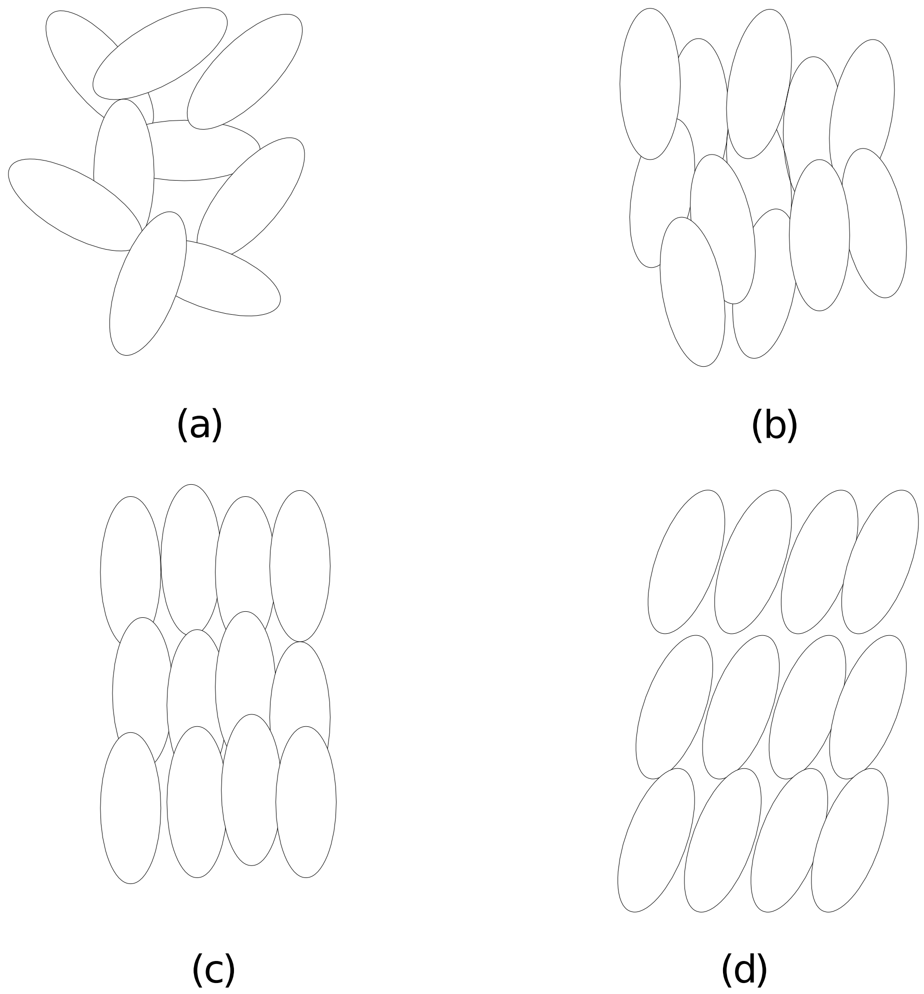

Figure 1.1: Schematic representation of phases formed by calamitic mesogens: isotropic liquid (a), nematic liquid crystal (b), smectic A liquid crystal (c) and smectic C liquid crystal (d).

The helical pitch of a chiral nematic phase can be defined as the length over which the director has completed a full 360^0 rotation. Figure 1.2 shows a 180^0 rotation, *i.e.* the length separating the top layer from bottom is a half pitch $p/2$.

1.1.3 Smectic phases

In smectic mesophases mesogens exhibit both rotational and translational order. A distinct structural feature of the smectic phase is a layered structure, with mesogens organised in layers with well-defined interlayer spacing. This can be observed with experimental techniques, for example x-ray diffraction. Compared to nematic phases, smectics have more order. This leads to them appearing at lower tempera-

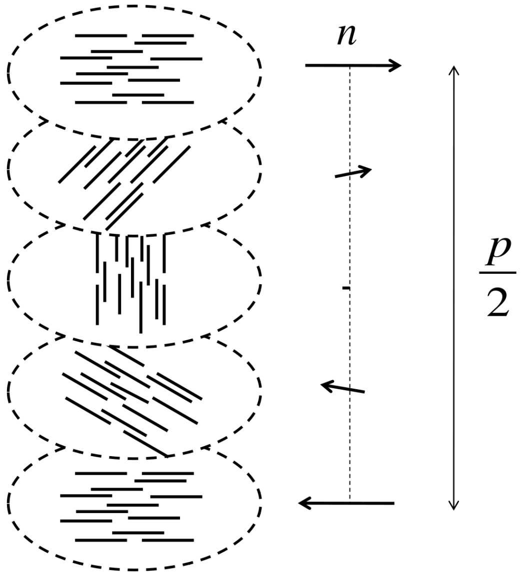

Figure 1.2: A Schematic representation of the chiral nematic (N*) phase.

tures than nematic phases for most thermotropic mesogens [7].

The simplest type of smectic, a smectic A (SmA) phase, is presented in figure 1.1 (c). In a SmA, molecules are oriented along the director, $\hat{\mathbf{n}}$, of the phase. The molecules are organised into layers perpendicular to the director, but there is no long range ordering inside layers or between layers. Therefore each layer approximates to a two dimensional liquid [19]. The smectic B (SmB) phase has similar ordering to the SmA, but in addition it has hexagonal ordering within the layers. There is no long range inter layer ordering, so this phase still has some liquid characteristics. The smectic C (SmC) phase, (figure 1.1 (d)), is a tilted analogue of the SmA phase. In the SmC phase a tilt angle exists between the director and the layer normal. The molecules do not possess long range intra-layer nor inter-layer order. In addition to these smectic phases, there exists a cascade of other smectics, including the hexatic mesophases smectic F (SmF) and smectic I (SmI) [19].

1.1.4 Discotic phases

The most common discotic phases are nematic and columnar (figure 1.3). In discotic nematic molecules are arranged such that their unique axis (short axis in this case) points on average along the phase director. As in its calamitic counterpart no long range translational order exists. The columnar phase is a discotic analogy

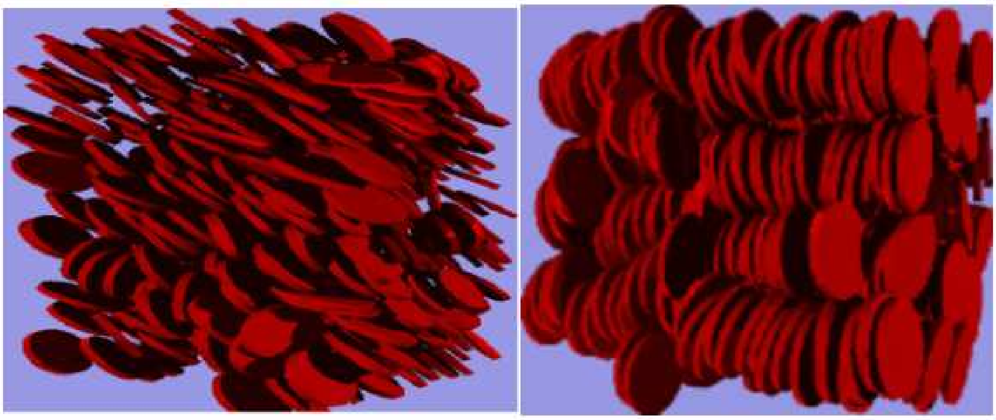

Figure 1.3: Liquid crystal phases formed by discotic mesogens: nematic (left) and columnar (right). Snapshots are taken from Monte Carlo simulations of hard cut spheres, courtesy of Dr Peter Duncan, Durham University.

of the calamitic smectic A phase. In the columnar phase the mesogens are packed in columns, with the columns arranged parallel to the director and packed on a two dimensional lattice. According to the arrangement of columns in a two dimensions, columnar phases can be classified into three different categories: hexagonal, rectangular and oblique [19].

1.2 Liquid crystal macromolecules

Alongside the progress made in experimental and computational techniques of simple organic liquid crystals, more complex systems exhibiting liquid crystal behaviour have also been studied. One area of interest are large macromolecular systems containing mesogenic groups. These can be divided into two categories, liquid crystal polymers and liquid crystal dendrimers.

Liquid crystal polymers (LCPs) are characterised by a polymer back bone with anisotropic mesogens attached to it. LCPs can generally be divided into two groups: main chain LCPs (MCLCPs) with mesogenic groups coupled linearly, or side chain LCPs (SCLCPs) with mesogenic groups attached terminally or laterally to a flexible spacer chain grafted to the polymeric back bone. Schematic representations are given in figure 1.4.

The building blocks of main chain LCPs are the flexible parts of the polymeric

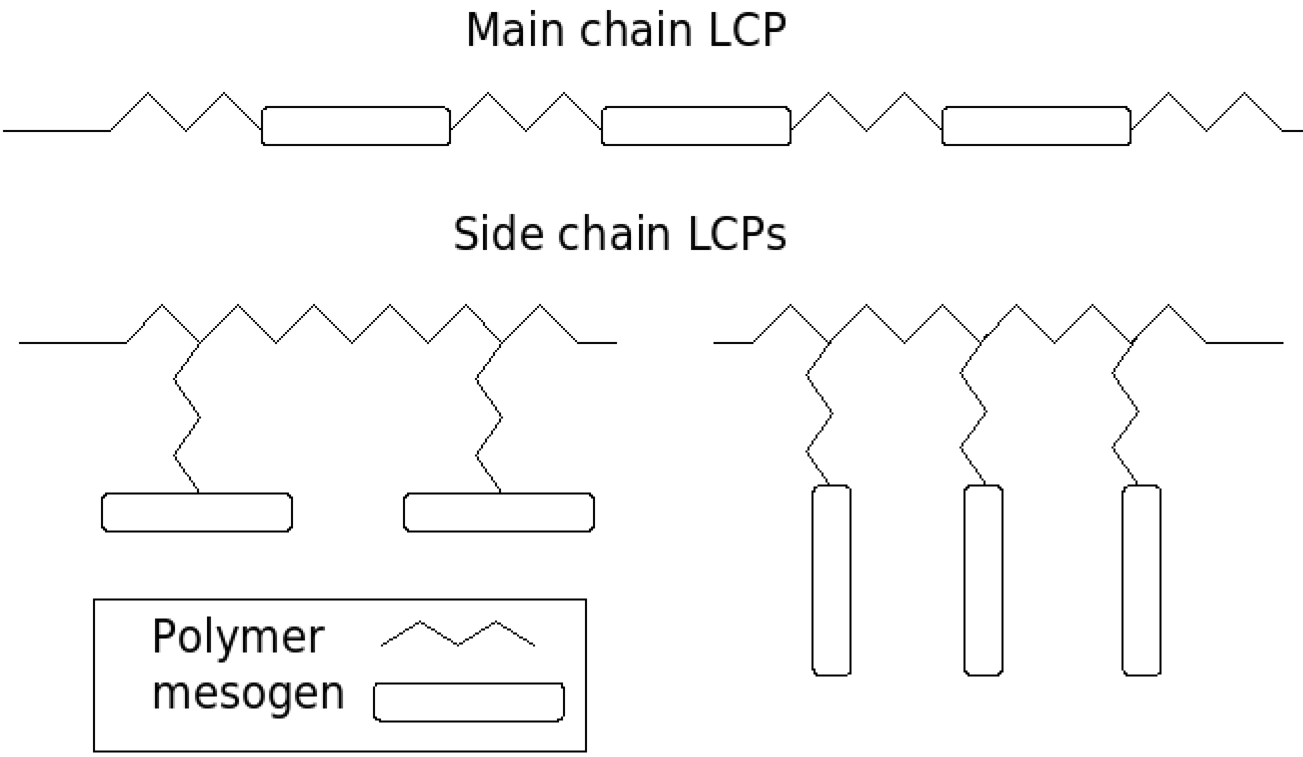

Figure 1.4: Schematic representation of Liquid Crystal Polymers (LCPs): Main chain LCP (top), side chain LCPs (bottom); laterally (left) and terminally (right) connected mesogenic groups.

backbone and mesogenic groups. Side chain LCPs have three main building blocks: mesogenic groups, flexible spacers and the polymeric backbone. The driving force for formation of liquid crystal mesophases are the anisotropic interactions between mesogenic groups. The flexible spacer works as a separator allowing mesogens to order, while the polymeric backbone adopts its random coil conformation [20]. Side chain LCPs are thought to have interesting applications, for example optical switching in electro optical applications [21].

Different types of dendritic and hyperbranched polymer systems have been of great interest for researchers and have been widely studied (for example [22–29]). Despite the breadth of the topic several common types can be identified [30]. These include dendrimers and hyperbranched polymers which are constructed in generations of branches in which the mesogenic units form part of each branching unit [30]. The branching structure can be seen in figure 1.5 for first and second generation dendrimers.

Dendrimers offer a nice spherical scaffold for supermolecule design. For example,

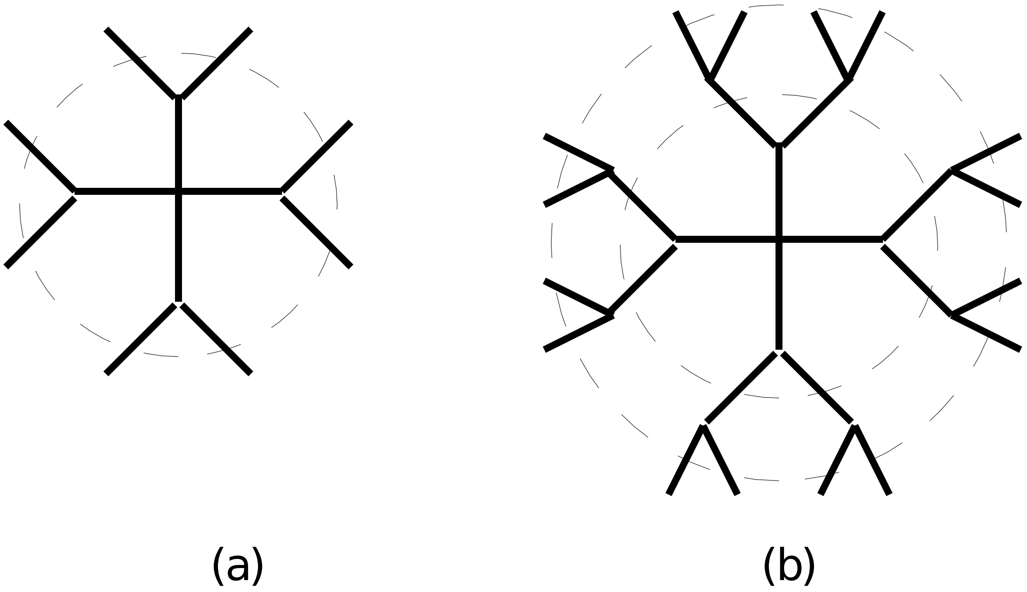

Figure 1.5: A stick model for dendrimers; first generation (a) and second generation (b).

by attaching mesogens to the end of each dendritic branch by means of flexible spacers (figure 1.6). Saez and Goodby [24] have studied a supermolecular Liquid Crystal Dendrimer (LCDr) with an octasilsesquioxane core. Eight separate branches were attached to the core, thus it can be considered as a first generation dendrimer with mesogenic units terminally attached. It was found to exhibit smectic A and tilted smectic C phases. With a similar core but laterally attached mesogens, the supermolecules were found to form a chiral nematic phase [31].

Liquid crystal polymers and dendrimers have also been objects of computational studies. A recent molecular dynamics study [32] of a polysiloxane side chain LCP demonstrated growth of a smectic A phase from an isotropic liquid with the help of small aligning field. Dendritic systems have also been studied previously by molecular simulations (for example [33–35]). These include the development of a 3-dimensional molecular structure builder for molecular simulation of dendrimers which uses Continuous Configuration Biased direct Monte Carlo Method [34]. Despite efforts, no molecular simulation have been able to produce the spontaneous self assembly of a bulk LCDr to ordered liquid crystalline phases, as observed in experiments. A recent coarse grained study of a third generation LCDr showed spontaneous microphase separation, but a small aligning field was needed to form

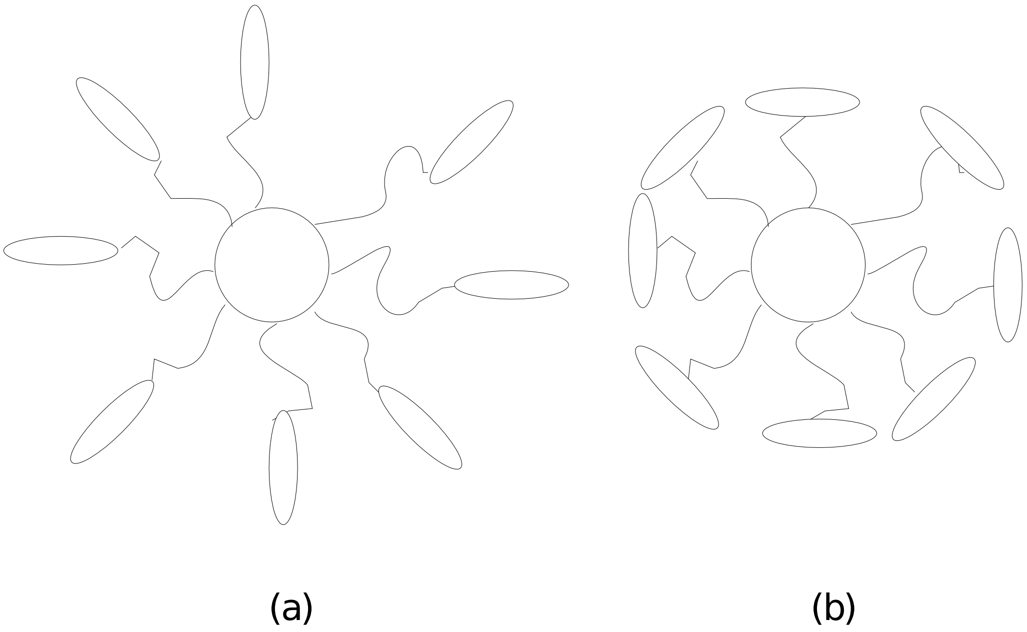

Figure 1.6: Cartoon representation of a supermolecule with a dendritic scaffold containing mesogens attached terminally (a) and laterally (b).

an ordered smectic A phase [36].

1.3 Surfactants in solution

Amphiphilic solute molecules consist of two parts: one which would be insoluble and another which would be highly soluble in a chosen solvent [11]. It is favourable for the insoluble parts to be separated from the solvent. In the presence of a surface or a boundary the amphiphilic molecules tend to concentrate to the solvent boundary thus they are also called surfactants.

For low concentrations in a water like solvent, surfactant molecules (composed of a hydrophilic head group and a hydrophobic tail group) can exist as free monomers. When the concentration of the surfactants is increased above threshold known as the *critical micelle concentration*, the surfactants aggregate to form micelles. The surfactants self-assemble in such way that the hydrophilic head groups form a shielding core around the hydrophobic tail groups. Examples of these aggregates include spherical micelles, worm like micelles, bilayers and vesicles [11]. In figure 1.7 cartoon representations of surfactant molecules composed of a spherical hydrophilic head group connected to a hydrophobic coil, are presented as free monomers 1.7(a),

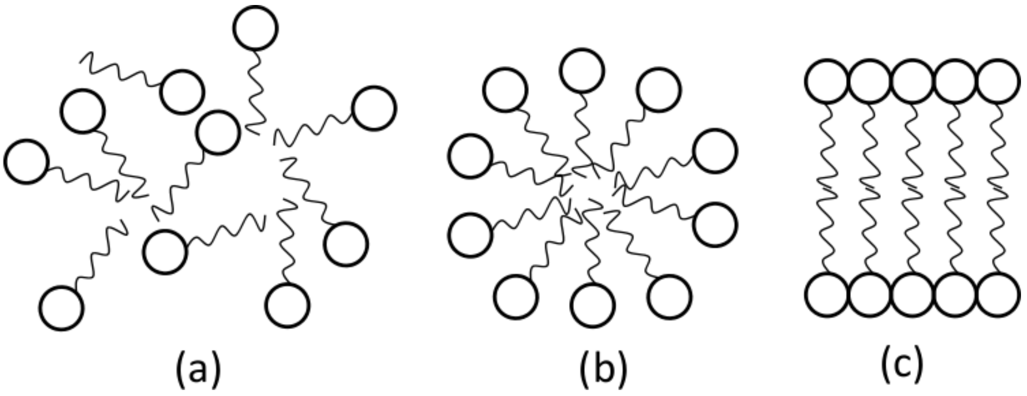

Figure 1.7: Examples of assemblies of surfactant molecules consisting of a hydrophilic head group represented by a sphere and a hydrophobic tail group represented by a coil: Free monomers (a), spherical micelle (b) and bilayer (c).

a spherical micelle 1.7(b) and as a bilayer 1.7(c).

1.4 Molecular simulations

At equilibrium, in a given thermodynamic state, the free energy is at a minimum. When the system goes through a phase transition, induced by a change in temperature, pressure or concentration, the structure of the state corresponding to the free energy minimum can change dramatically [10]. An example of this is the orientational order change at the isotropic-nematic phase transition.

In a system where volume, V, is constant, the relevant free energy is the Helmholtz free energy [37]

$$A = U - TS, \tag{1.2}$$

where U is the internal energy of the system and S is the entropy. Correspondingly, for a system where the volume is allowed to fluctuate, the relevant free energy is provided by the Gibbs free energy

$$G = U - TS + PV, \tag{1.3}$$

where the product, PV, of pressure, P, and volume, V, is added to the Helmholtz free energy.

Entropy changes play an important role in phase transitions. Entropy is a maximum when a system is totally disordered. Therefore at relatively high temperatures equation (1.2) has a minimum for the disordered liquid structure. When temperature is lowered the relative contribution of the entropy is reduced. If there exists a state where the reduction of internal energy outweighs the reduction of entropy, when moving from a less ordered structure to a more ordered one, the system will undergo a phase transition.

Computer simulations can be used to gain extra information for systems of experimental interest. They can also be used to test new theories, or even simulate totally new systems out of reach for current experimental techniques and too complex for theoretical studies. There is a wide cascade of different computational techniques for studying complex systems ranging from *ab initio* electronic structure calculations for individual molecules and nanostructures [38] to continuum models for fluids [39]. Between these two extremes there are molecular simulation techniques [40] in which the sampling of phase space is carried out by random number techniques (Monte Carlo simulations) or solving equations of motions (molecular dynamics) in a chosen thermodynamic ensemble [41]. These methods can be used to find the equilibrium structures minimising the free energies of equations (1.2) and (1.3). Interactions between particles are normally derived in pairwise additive fashion using effective pair potentials.

Figure 1.8 shows an example of morphologies obtained via molecular simulation of model diblock copolymer based on poly(styrene-b-isoprene) (PS-b-PI) diblock copolymer [1]. Here the simulation results demonstrate the formation of lamellar, gyroid, hexagonal packed cylinder and body-centred cubic phases for different compositions, $f_s = N_{\mathrm{PS}}/(N_{\mathrm{PS}} + N_{\mathrm{PI}})$.

As mentioned earlier, the aim of molecular simulations is to find the structure minimising the corresponding free energy, for given control parameters such as the temperature and/or pressure. However, for the self-assembly of complex molecules, this has two distinct, but somewhat connected problems: firstly, the structures may be separated by considerable free energy barriers, leading to poor sampling of phase space and secondly, a time scale problem for moving between structures. Self-assembling complex systems typically consists of millions of atoms with self-

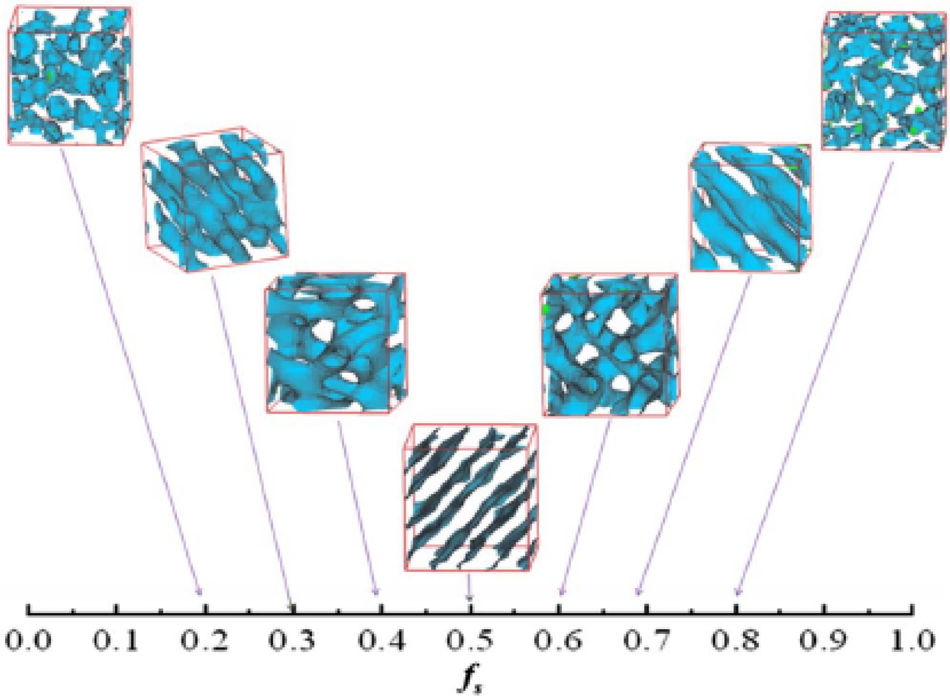

Figure 1.8: Examples of simulated morphologies for PS-b-PI diblock copolymer systems obtained from the molecular simulations (from middle; lamellar, gyroid, hexagonal and body-centred cubic) and their composition, $f_s = N_{\mathrm{PS}}/(N_{\mathrm{PS}} + N_{\mathrm{PI}})$, domains. Reprinted with permission from [1]. Copyright [2009], American Institute of Physics.

assembly times of milliseconds and beyond [42]. To a certain extent, the problem of large numbers of atoms has been and can be solved with the aid of modern high-performance computers by distributing the calculations over many thousands of processors. However, typically these large scale simulations are restricted to time scales of less than 100 ns [42]. Clearly, the time scale problem still exists. The aim of this work is to test and developed new and recent models and methods to aid in bridging the time and length scales associated with the self-assembly of complex materials and improve the sampling of the phase space.

In chapter 2, models *i.e.* effective pair potentials for the simulation of complex self-organising fluids relevant for this thesis will be discussed. Also relevant simulation methods, namely Monte Carlo (MC) and Molecular Dynamics (MD) will be introduced. Further, advanced (mesoscopic) simulation techniques such as Dissipative Particle Dynamics (DPD) and Stochastic Rotational Dynamics (SRD) will be discussed in some detail.

In chapter 3, a new anisotropic soft-core model is developed. This new model is by construction continuous and goes smoothly to zero making it usable in dynamics simulations. It also has a tunable attractive interaction and its soft-core nature eases problems of equilibration. It is used for simulation of single site systems and for simulation of a multipedal liquid crystalline supermolecule. The latter result demonstrate that the new anisotropic model can be used to probe phenomena occurring on fairly long time scales. Chapter 4, describes how the model developed in chapter 3, can be used to map out the phase diagram of a model main chain liquid crystalline polymer as a function of the length of the mesogenic unit. The chapter also presents a study of chiral induction effects seen in flexible achiral molecules within a chiral solvent.

In chapter 5 SRD is combined with a surfactant model to study the formation of micelles and pathways of micelle formation in a water-like solvent.[1] This scheme allows for a computationally efficient treatment of the solvent while still maintaining correct hydrodynamics, thus allowing the study of non equilibrium phenomena.

---

[1] Collaborative work with Prof. David J. Earl and Dr Christopher Adam Hixson, Department of Chemistry University of Pittsburgh, USA.

Chapter 6 introduces the recently developed Statistical Temperature Molecular Dynamics (STMD) simulation method. In chapter 6 STMD is combined with the soft-core model developed in chapter 3, to study isotropic-nematic and isotropic-lamellar phase transitions in greater detail. The STMD method allows the simulation of a fairly large temperature window by a single simulation and the thermodynamic quantities such as entropy and free energy are readily available.

In the final results chapter, chapter 7, the Hamiltonian Replica Exchange Molecular Dynamics (HREMD) method and another new anisotropic soft-core model developed Dr. Roberto Berardi in University of Bologna[2], will be introduced. This soft-core model will be used in connection with HREMD, to simulate the isotropic-nematic phase transition. The HREMD approach provides up to an order of magnitude speed up in equilibration, compared to a conventional model. Finally, the thesis results are concluded in chapter 8.

---

[2] Collaborative project with Prof. Claudio Zannoni and Dr Roberto Berardi, Department of Industrial Chemistry, University of Bologna, Italy.

Chapter 2

Computer simulations of self-organising soft matter

In order to effectively study ordered mesophases in soft-matter systems some level of simplification *i.e.* coarse graining (CG) is required. In CG models some details present in a "real" atomistic picture of a molecule are coarse grained away and only key features, such as shape or size, are preserved in the coarse grained representation. CG models can be roughly divided into two categories: single-site models or multi-site models. In a single-site CG system the whole molecule is described by a simple single-site potential. Popular choices for anisotropic molecules are the Gay-Berne potential [43] and spherocylinder potentials [44].

In this chapter, two common anisotropic models, the Gay-Berne and spherocylinder potentials, used in this work, will be introduced in sections 2.1.1 and 2.1.2, respectively. The relevant simulation methods for this thesis, Monte Carlo, molecular dynamics and Stochastic Rotational Dynamics will be discussed in sections, 2.2.1, 2.2.2 and 2.2.5, respectively. In section 2.3, it is explained how the formation of different mesophases can be identified from the data generated by molecular simulation, by means of order parameters and pair correlation functions. Finally, section 2.4 discusses how coarse grained molecules can be related to atomistic models of real molecules.

2.1 Types of anisotropic models for soft matter

At the heart of molecular simulation is the interaction between particles. For a simple system consisting of N particles the potential energy can be expressed as a summation over individual particles, pairs of particles, particle triplets and higher terms [45],

$$U = \sum_i u_1(\boldsymbol{r}_i) + \sum_i \sum_{j>i} u_2(\boldsymbol{r}_i, \boldsymbol{r}_j) + \sum_i \sum_{j>i} \sum_{k>j>i} u_3(\boldsymbol{r}_i, \boldsymbol{r}_j, \boldsymbol{r}_k) + \dots, \tag{2.1}$$

where the summation $\sum_{j>i}$ implies that every pair interaction is calculated only once. The first term in eq. (2.1) describes the effect of an external field, the second term is a pair potential and the third describes three body interactions. The three body terms are computationally very demanding, scaling as N^3, but (especially at fluid densities) have a considerable effect [45]. Four-body and higher order terms can be assumed to be considerable smaller than pair or three body interactions [45]. It has been discovered that three-body interactions can be partially included into a pair potential by defining an effective pair potential, which then can be used in simulations. Now the potential energy can be written [45]

$$U \approx \sum_i u_1(\boldsymbol{r}_i) + \sum_i \sum_{j>i} u_2^{\text{eff}}(\boldsymbol{r}_i, \boldsymbol{r}_j). \tag{2.2}$$

The simplest kind of LC models are lattice models where particles are confined to a two or three dimensional lattice. Particles interact with nearest neighbours through a simple anisotropic potential [46]. The lattice model for simulation of liquid crystals was originally developed by Lebwohl and Lasher [47]. In the method of Lebwohl and Lasher, sites interact through simple orientation dependent potential with head-to-tail symmetry. Since then many more lattice models have been developed. For a review see reference [44].

The next development in modelling liquid crystals involved the use of off-lattice single site models. In these, individual mesogens are modelled by continuous potentials with anisotropic terms. The most common choices include the Gay-Berne (GB) [43] potential, an anisotropic form of the Lennard-Jones potential with an anisotropic attractive well and short range repulsion, and other non-spherical potentials such as the spherocylinder model. These will be introduced in sections 2.1.1 and 2.1.2, respectively. The Gay-Berne potential [43] has four parameters, $(\kappa, \kappa', \mu, \nu)$, for describing the anisotropy of attractive and repulsive interactions. Due to the (in principle) infinite number of parametrisations available and the rich phase sequences exhibited, the Gay-Berne potential is probably the single most studied LC model. It has been used, for example, to model calamitic molecules [48–51] exhibiting isotropic, nematic, smectic A and smectic B phases. In the search for a tilted smectic C phase an internally rotated Gay-Berne model has been developed [52]. The versatility of the GB model has further been demonstrated by simulation of discotic GB particles [53, 54].

In contrast to the GB model, the spherocylinder potential is parametrised by a single parameter: the length to breadth ratio, L/D. The first computer simulations for hard spherocylinders were done by Vieillard-Baron in 1974 with elongations $L/D = 1$ and 2 [55]. No ordered phases were found. Since then, the model has been found to exhibit isotropic (I), nematic (N), smectic A (SmA) and solid (K) phases [56, 57], and the phase stability has been has been established as [57]: $k = 1 + L/D \geq 4.7$ for nematic and $k = 1 + L/D \geq 4.1$ for smectic A. A soft repulsive spherocylinder (SRS) model with Lennard-Jones type of potential has been also studied extensively, (for example [58, 59]) and it has been found to exhibit isotropic, nematic, smectic A and smectic B phases. Recently very soft potentials for SRSs have been developed [60]. For some of these new potential models phase formation was considerably faster than with conventional SRS potentials, while still preserving the rich phase behaviour.

Studies of ellipsoidal particles have also been carried out using hard ellipsoids [61]. These systems are found to exhibit a nematic phase, but no smectic phase was found for hard ellipsoids. There have also been attempts to adopt a continuous model for ellipsoidal shape [62, 63] between two mesogens. Paramonov and Yaliraki [63] developed a model to obtain the distance of closest approach between two arbitrary ellipsoids. Their method is valid for any orientation and separation along the vector between their centres.

To obtain more control of structural quantities and allow for more realistic description, multi-site models have been developed. In these, the LC molecule is typically described as a combination of isotropic (spheres) and anisotropic (for example GB or spherocylinder) sites. This kind of model allows a better description of complex LC molecules and still keeps computational costs reasonably low. Multi-site models have been applied recently to the simulation of a side chain liquid crystal polymer [32] and a third generation LC dendrimer [36].

2.1.1 The Gay-Berne potential

In the Gay-Berne (GB) model, liquid crystal molecules are considered to be rigid particles with axial symmetry [43]. In addition to the anisotropy parameters, $(\kappa, \kappa', \mu, \nu)$, the GB potential has two parameters $(\sigma_0,\ \epsilon_0)$, which are used to define length and energy scales. Molecule i is described by a centre of mass vector $\boldsymbol{r}_i$ and a unit vector along the long axis $\hat{\boldsymbol{u}}_i$. The interaction energy between two GB particles, i and j, can be written as [50]

$$U_{ij}^{\mathrm{GB}}\left(\boldsymbol{r}_{ij}, \hat{\boldsymbol{u}}_i, \hat{\boldsymbol{u}}_j\right) = 4\epsilon\left(\hat{\boldsymbol{r}}_{ij}\hat{\boldsymbol{u}}_i, \hat{\boldsymbol{u}}_j\right)\left(R^{-12} - R^{-6}\right), \tag{2.3}$$

where the anisotropic distance parameter is defined as

$$R = \left(r_{ij} - \sigma\left(\hat{\boldsymbol{r}}_{ij}, \hat{\boldsymbol{u}}_i, \hat{\boldsymbol{u}}_j\right) + \sigma_0\right)/\sigma_0. \tag{2.4}$$

The anisotropic contact distance $\sigma\left(\hat{\boldsymbol{r}}_{ij}, \hat{\boldsymbol{u}}_i, \hat{\boldsymbol{u}}_j\right)$ depends of the orientation of the inter-molecular vector $\boldsymbol{r}_{ij} = \boldsymbol{r}_i - \boldsymbol{r}_j$ and individual molecular orientations:

$$\sigma\left(\hat{\boldsymbol{r}}_{ij}, \hat{\boldsymbol{u}}_i, \hat{\boldsymbol{u}}_j\right) = \sigma_0\left[1 - \chi\left(\frac{\left(\hat{\boldsymbol{u}}_i \cdot \hat{\boldsymbol{r}}_{ij}\right)^2 + \left(\hat{\boldsymbol{u}}_j \cdot \hat{\boldsymbol{r}}_{ij}\right)^2 - 2\chi\left(\hat{\boldsymbol{u}}_i \cdot \hat{\boldsymbol{r}}_{ij}\right)\left(\hat{\boldsymbol{u}}_j \cdot \hat{\boldsymbol{r}}_{ij}\right)\left(\hat{\boldsymbol{u}}_i \cdot \hat{\boldsymbol{u}}_j\right)}{1 - \chi^2\left(\hat{\boldsymbol{u}}_i \cdot \hat{\boldsymbol{u}}_j\right)^2}\right)\right]^{-1/2}, \tag{2.5}$$

where σ_0 is the contact distance when particles are in the cross configuration when $\hat{\boldsymbol{r}}_{ij} \cdot \hat{\boldsymbol{u}}_i = \hat{\boldsymbol{r}}_{ij} \cdot \hat{\boldsymbol{u}}_j = \hat{\boldsymbol{u}}_i \cdot \hat{\boldsymbol{u}}_j = 0$. The parameter χ is function of the ratio $\kappa \equiv \sigma_e/\sigma_s$,

$$\chi = \frac{\kappa^2 - 1}{\kappa^2 + 1}. \tag{2.6}$$

Here, σ_s is the contact distance when molecules are side by side and σ_e is the contact distance for the end to end configuration. The lower limit of the parameter χ is minus one when the shape of the particle is an infinitely large disk, it vanishes for spheres and the corresponding upper limit is one which corresponds to an infinitely long rod [50].

The orientational dependence of the potential well depth can be expressed as a product of two functions

$$\epsilon\left(\hat{\boldsymbol{r}}_{ij}, \hat{\boldsymbol{u}}_i, \hat{\boldsymbol{u}}_j\right) = \epsilon_0 \epsilon^{\nu}\left(\hat{\boldsymbol{u}}_i, \hat{\boldsymbol{u}}_j\right) \epsilon'^{\mu}\left(\hat{\boldsymbol{r}}_{ij}, \hat{\boldsymbol{u}}_i, \hat{\boldsymbol{u}}_j\right), \tag{2.7}$$

where ϵ_0 is the well depth at side by side configuration. The first of these functions can be written as

$$\epsilon\left(\hat{\boldsymbol{u}}_i, \hat{\boldsymbol{u}}_j\right) = \left[1 - \chi^2\left(\hat{\boldsymbol{u}}_i \cdot \hat{\boldsymbol{u}}_j\right)\right]^{-1/2}. \tag{2.8}$$

This has a maximum value when $\left(\hat{\boldsymbol{u}}_i \cdot \hat{\boldsymbol{u}}_j\right)^2 = 1$, corresponding to a parallel orientation for the particles. The second function has a similar form to the anisotropic contact distance (2.5), so it has more effect on the anisotropy of the well depth

$$\epsilon'\left(\hat{\boldsymbol{r}}_{ij}, \hat{\boldsymbol{u}}_i, \hat{\boldsymbol{u}}_j\right) = 1 - \chi'\left(\frac{\left(\hat{\boldsymbol{u}}_i \cdot \hat{\boldsymbol{r}}_{ij}\right)^2 + \left(\hat{\boldsymbol{u}}_j \cdot \hat{\boldsymbol{r}}_{ij}\right)^2 - 2\chi'\left(\hat{\boldsymbol{u}}_i \cdot \hat{\boldsymbol{r}}_{ij}\right)\left(\hat{\boldsymbol{u}}_j \cdot \hat{\boldsymbol{r}}_{ij}\right)\left(\hat{\boldsymbol{u}}_i \cdot \hat{\boldsymbol{u}}_j\right)}{1 - \chi'^2\left(\hat{\boldsymbol{u}}_i \cdot \hat{\boldsymbol{u}}_j\right)^2}\right), \tag{2.9}$$

where parameter χ' is defined as a function of the well depths $\kappa' \equiv \epsilon_s/\epsilon_e$ as

$$\chi' = \frac{\kappa'^{1/\mu} - 1}{\kappa'^{1/\mu} + 1}. \tag{2.10}$$

It should be noted that when choosing $\kappa = \kappa' = 1$, the GB potential form will reduce into a normal Lennard-Jones potential with $\sigma = \sigma_0$ and $\epsilon = \epsilon_0$ for all choices of exponents μ, ν [51].

For the potential between two GB particles four basic configurations can be defined [5]. In the side by side configuration (s), the symmetry axes of both molecules are parallel and the vector joining the centre of masses is perpendicular to both symmetry axes. In the end to end configuration (e), both the symmetry axes and the vector between the two centre of masses are parallel. In the T-configuration

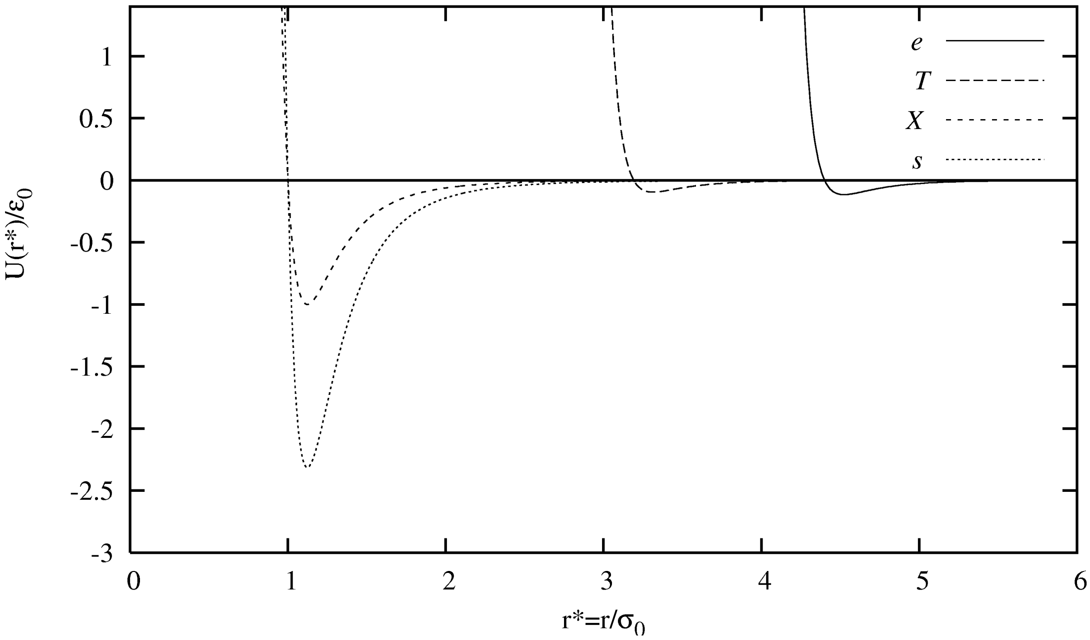

Figure 2.1: The distance dependence of the Gay-Berne potential in reduced units, $U^*(r^*) = (r^*)/\epsilon_0$ and $r^* = r/\sigma_0$, for four different configurations: end to end (e), T-configuration (T), cross configuration (X) and side by side (s), with parameterisation $\kappa = 4.4$, $\kappa' = 20.0$ and $\mu = \nu = 1$ ie. GB(4.4, 20.0, $1, 1$).

(T), one symmetry axis is parallel to the vector joining the centre of masses while the other symmetry axis is perpendicular to both. The final configuration is the cross-configuration (X) where the symmetry axes and the vector between centre of masses are perpendicular. For these four configurations the distance dependence of a GB-potential with parameterisation GB$(\kappa, \kappa', \mu, \nu)$ = GB(4.4, 20.0, 1, 1) is presented in figure 2.1.

Chapter 7 of this thesis, discusses a replica exchange method, which provides an efficient way of improving the speed of equilibration of simulations using Gay-Berne potentials.

2.1.2 Spherocylinder potentials

A spherocylindrical particle can be realised as a cylindrical rod of length L and diameter D, with each end of the cylinder capped by a hemisphere of diameter D (figure 2.2) [64]. The total length of spherocylinder can be written as a function of the diameter D as $k = 1 + L/D$. The limits for the aspect ratio $L/D = 0$

Table 2.1: The well depth $\epsilon\left(\hat{\boldsymbol{r}}_{ij}, \hat{\boldsymbol{u}}_i, \hat{\boldsymbol{u}}_j\right)$ and the contact distance between particles $\sigma\left(\hat{\boldsymbol{r}}_{ij}, \hat{\boldsymbol{u}}_i, \hat{\boldsymbol{u}}_j\right)$ for the Gay-Berne potential in four different configurations [5].

Configuration	$\sigma\left(\hat{\boldsymbol{r}}_{ij}, \hat{\mathbf{u}}_i, \hat{\boldsymbol{u}}_j\right)$	$\epsilon\left(\hat{\mathbf{r}}_{ij}, \hat{\boldsymbol{u}}_i, \hat{\boldsymbol{u}}_j\right)$
e	$\sigma_0\sigma_e/\sigma_s\left(\equiv\sigma_e\right)$	$\epsilon_0\left(\epsilon_e/\epsilon_s\right)\left(1-\chi^2\right)^{-\nu/2}$
s	$\sigma_0\left(\equiv\sigma_s\right)$	$\epsilon_0\left(1-\chi^2\right)^{-\nu/2}$
X	$\sigma_0\left(\equiv\sigma_s\right)$	ϵ_0
T	$\sigma_0\left[\left\{\left(\sigma_e/\sigma_s\right)^2+1\right\}/2\right]^{1/2}$	$\epsilon_0\left[2/\left\{\left(\epsilon_s/\epsilon_e\right)^{1/\mu}+1\right\}\right]^{\nu}$

and $L/D = \infty$ corresponds to a sphere of diameter D and to infinitely long rod respectively. A pair potential between spherocylinders is calculated as a function of the shortest distance between line segments, $\mathbf{d}_{ij}$, of particles i and j. As a function of $\mathbf{d}_{ij}$ the interaction takes the same form as two spheres of diameter D at separation d_{ij}. This gives the spherocylinder an advantage over, for example GB-potentials, by allowing a choice of an effective pair potential.

The first spherocylinder model studied was a hard spherocylinder (HRS) [65]. In the HRS model the particles are considered as hard particles and the potential energy can be written as

$$U(d_{ij}) = \begin{cases} \infty & , \quad d_{ij} \leq D \\ 0 & , \quad d_{ij} > D. \end{cases} \tag{2.11}$$

In this case the factor influencing phase formation is the elongation, L/D, as the phase formation is dependent on excluded volume interactions and the competition between translational and rotational entropy [46].

In order to achieve a model with a continuous potential energy surface, a soft repulsive spherocylinder (SRS) can be considered. In the SRS model the pair potential is a cut and shifted Lennard-Jones potential [66],

$$U(d_{ij}) = \begin{cases} 4\epsilon\left[\left(\frac{\sigma_0}{d_{ij}}\right)^{12} - \left(\frac{\sigma_0}{d_{ij}}\right)^{6} + \frac{1}{4}\right] & , \quad d_{ij} \leq d_{\text{cut}} \\ 0 & , \quad d_{ij} > d_{\text{cut}}, \end{cases} \tag{2.12}$$

where $\sigma_0 = D$ and d_{cut} is the cutoff radius with value $d_{\text{cut}} = 2^{1/6}\sigma_0$. This system with elongation $L/D = 4$ was observed in MD simulations to exhibit mesophase behaviour

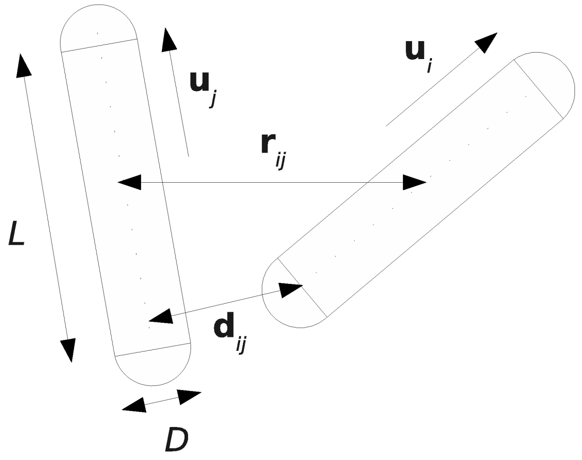

Figure 2.2: Spherocylinders i and j characterised by the cylinder length L, width D and orientations $\hat{\mathbf{u}}_i$, $\hat{\mathbf{u}}_j$. $\mathbf{r}_{ij}$ is vector between the centre of masses and $\mathbf{d}_{ij}$ is the shortest vector between line segments.

including the phases: Isotropic, nematic, smectic A and solid [66]. The SRS model has a strong advantage over the HRS model in its usability in conventional MD simulations, namely it is smooth and continuous and it goes smoothly to zero at the cutoff. So it could be employed as an effective potential for coarse grained mesogenic groups in a multi-site model as presented in recent simulations of a dendrimer system [36].

Despite some success with the SRS model in molecular simulations the (12, 6) Lennard-Jones shape makes its curvature very steep and therefore a limiting factor in terms of bigger timesteps (MD) or bigger trial moves (MC). To improve this, a recent study [60] considered some “ultrasoft “ repulsive models for spherocylinders. Collectively each pair potential had a finite value at zero separation, $U_{\max}$, and thus allowed particles, at least in theory, to fully overlap and move through each other. The most promising results were obtained from a repulsive quadratic potential

$$U(d_{ij}) = \begin{cases} U_{\max}\left(1 - \frac{d_{ij}}{\sigma_0}\right)^2 & , \quad d_{ij} \le d_{\text{cut}} \\ 0 & , \quad d_{ij} > d_{\text{cut}}. \end{cases} \tag{2.13}$$

where $d_{\text{cut}} = \sigma_0 = D$. This potential produces a linear force, so it could be considered the softest possible potential with sensible equations of motion. For choice of elongations of $L/D = 5$ and 7, MD simulations yielded the formation of isotropic, nematic and smectic A phases. With a reasonable choice of energy at zero separation, $U_{\max}/k_BT = U^*_{\max} \in [10,\ 35]$, a considerably longer time step was successfully employed compared to the SRS model [60]. The results presented in [60] showed a speed-up of approximately 20-30 times for a growing nematic phase from an isotropic liquid were possible, when a model of equation (2.13) with $U_{\max} = 35k_BT$ was compared to a standard SRS potential.

Making potentials softer does have drawbacks. The finite value of the potential energy at full overlap, $U_{\max}$, does, in theory, allow particles to go through each other. Therefore $U_{\max}$ must chosen to be sufficiently high. In a study of nematic phase with $L/D = 5$ spherocylinders modelled with equation (2.13), showed that realistic structural features could only be achieved by choosing $U_{\max} \geq 35k_BT$ [60]. Because of the complete lack of anisotropic forces, phase formation is driven by excluded volume interactions and competition between rotational and translational entropy. Making potentials very soft effectively removes the excluded volume interaction. Moreover, at very high densities particles will be driven to overlap, to reduce the excluded volume rather than to align with each other via the usual excluded volume mechanism.

There also exists a spherocylinder model with anisotropic attractive forces, namely a Kihara potential with GB-type epsilon [67]. This potential has the same disadvantage as the SRS potential; the curvature is too steep to allow the long time steps used with ultrasoft potentials. Therefore a very soft spherocylinder potential, with anisotropic attractive interactions, could prove to be very useful model for use in effective coarse graining of complex systems. Chapter 3 describes the development of such a model based on the quadratic form of equation (2.13) and its uses in range of simulation problems are described in chapters 3 and 4.

2.2 Simulation techniques

The previous section introduced models for coarse grained anisotropic particles used in the course of this thesis. In order to study the phase behaviour of bulk systems consisting of these particles *i.e.* finding the structure corresponding to a free energy minimum for a set value of external control parameters such as the temperature

Table 2.2: Some differences between Monte Carlo (MC) and Molecular Dynamics (MD) methods, taken form reference [6].

Property	MC	MD
Basic information needed	Energy	Gradient (forces)
Particles moved in each step	One	All
Coordinates	Any	Cartesian
Constraints	Easy	Difficult
Atomic velocities	No	Yes
Time dimension	No	Yes
Deterministic	No	(Yes)
Sampling	Non-physical	Physical
Natural ensemble	NVT	NVE

or pressure, molecular simulations need to be performed. Molecular simulations for soft matter systems are normally carried out by using either Monte Carlo techniques (trial configurations are created using random numbers) or molecular dynamics (MD) methods (Newton's equations of motion are solved for particle trajectories.)

2.2.1 Monte Carlo methods

The ensemble average of a function $f(\boldsymbol{r})$ can be calculated as a weighted integral [68]

$$\langle f \rangle = \frac{\int d\boldsymbol{r}^N \exp\left[-\beta U\left(\boldsymbol{r}^N\right)\right] f\left(\boldsymbol{r}^N\right)}{\int d\boldsymbol{r}^N \exp\left[-\beta U\left(\boldsymbol{r}^N\right)\right]}, \tag{2.14}$$

where $f(\boldsymbol{r})$ is the value of the function f at configuration $\boldsymbol{r}$ and $U(\boldsymbol{r})$ is the potential energy of a system of N particles at the same configuration. Apart from a few very simple cases, integrals cannot be calculated analytically. The simplest way of calculating the integral by a Monte Carlo (MC) method would be to generate random configurations for all particles and then calculate the total energy for the whole system. After that the configuration could be weighted by the Boltzmann factor $\exp[-\beta U]$. This procedure would then be repeated until satisfactory sampling had been reached. Unfortunately this method is very inefficient. At liquid densities most of the random configurations generated would have Boltzmann factors that would be really small. In 1953 Metropolis et al. [69] showed that choosing configurations with a probability $\exp[-\beta U]$ and giving them equal weights speeds up the integration significantly. This, the *Metropolis method,* proceeds as follows: Calculate the energy, E_o, of the old state, $\boldsymbol{r}^N$. Generate a new (random) state, $\boldsymbol{r}'^N = \boldsymbol{r}^N + \Delta\boldsymbol{r}^N$ and calculate the new energy E_n. If the energy difference is negative, $\Delta E = E_n - E_o$, the new state is accepted, otherwise the new state is accepted with a probability $e^{-\Delta E/k_BT}$. This results in configurations being chosen according to a Boltzmann distribution. Now the average in equation (2.14) can be approximated as,

$$\langle f\rangle \approx \frac{1}{L}\sum_{i=1}^{L} f\left(r_i^N\right), \tag{2.15}$$

where L is the total number of sampled configurations [68].

The natural ensemble for MC simulations is the canonical ensemble, this corresponds to fixed number of particles, N, with the volume of the simulation box, V, and temperature, T, as constants. Hence the acronym, NVT. At equilibrium in the NVT ensemble the Helmholtz free energy, equation (1.2) has a minimum. It is possible to generate other ensembles also. One very popular ensemble is the isothermal-isobaric (NPT) ensemble, in which the number of particles, pressure P and temperature are kept constant. The requirement of pressure being constant leads to the need for the volume to fluctuate. This can be achieved by introducing a new type of trial move in addition to normal particle trial moves. In a volume move the energy term is accompanied by two additional terms [6] $\Delta E \rightarrow \Delta E + P\Delta V - Nk_BT\ln(1+\Delta V/V)$, where ΔV is the difference between old and new volumes. Equilibrium corresponds to a minimum in the Gibbs free energy, described by equation (1.3).

In addition to taking place in a chosen ensemble, the MC trial moves have to fulfil important additional criterion: they should follow detailed balance [6]. This means that the random chain known as a Markov chain must arise from a symmetric acceptance decision. Further this means each step must be reversible, that is that the probability of undoing the step at the next move is same as taking the step in the first place. This said one popular MC scheme is one where trial moves are done sequentially to particles running from 1 to N. It is clear that this does not strictly obey the detailed balance. In fact it has been shown recently [70] that the detailed balance condition is overly strict and a weaker balance condition is sufficient.

Moreover, it has been shown that sequential updating schemes are correct and they leave the Boltzmann distribution unaffected [70].

In the work presented in this thesis, MC is not used on its own, but has been combined with molecular dynamics to allow sampling of volume space. This is explained in more detail in section 2.2.2.

2.2.2 Molecular dynamics

In molecular dynamics particle trajectories are followed which arise from interactions between particles. The force due to a potential $U(r)$ is $\mathbf{f}(r) = -\nabla_r U(r)$. Now the equation of motion for particle i arises from Newton's second law [71]

$$m\frac{d^2}{dr^2}\mathbf{r}_i = \mathbf{F}_i = \sum_{j=1}^{N} \mathbf{f}_{ij} \tag{2.16}$$

where the sum is taken over all N particles excluding the self interaction $j = i$. Due to the Newton's third law, $\boldsymbol{f}_{ij} = -\boldsymbol{f}_{ji}$ every particle pair needs to be evaluated only once. Integration of these equations gives rise to particle trajectories as a function of time, t.

Making a Taylor expansion for positions $\boldsymbol{r}(t+\delta t)$ and $\boldsymbol{r}(t-\delta t)$ at times $t+\delta t$ and $t-\delta t$ respectively about position $\boldsymbol{r}(t)$ [72],

$$\begin{aligned} \boldsymbol{r}(t+\delta t) &= \boldsymbol{r}(t) + \delta t\mathbf{v}(t) + 1/2\delta t^2\mathbf{a}(t) + \ldots \\ \boldsymbol{r}(t-\delta t) &= \boldsymbol{r}(t) - \delta t\mathbf{v}(t) + 1/2\delta t^2\mathbf{a}(t) - \ldots \end{aligned} \tag{2.17}$$

if truncating at δt^2, adding these two equations together and solving for $\boldsymbol{r}(t+\delta t)$ one arrives with an integration scheme known as the Verlet algorithm [73]

$$\boldsymbol{r}(t+\delta t) = 2\boldsymbol{r}(t) - \boldsymbol{r}(t-\delta t) + \delta t^2\mathbf{a}(t). \tag{2.18}$$

As seen above, velocities do not appear in the equation (2.18) explicitly, but they can be solved for the midpoint,

$$\mathbf{v}(t) = \frac{\boldsymbol{r}(t+\delta t) - \boldsymbol{r}(t-\delta t)}{2\delta t}. \tag{2.19}$$

The basic problem of the Verlet algorithm is now apparent. Solving of positions, equation (2.18), have errors of order δt^4, while the velocities, equation (2.19), have error of order δt^2. As velocities are used to estimate the kinetic energy, and as this contributes to the total energy, the errors may lead to considerable drift in the total energy.

More accurate integrators have been developed, for example the leap-frog algorithm [72] and velocity Verlet algorithm [74]. The essence of the leap-frog algorithm is to use half step, $t \pm 1/2\delta t$, velocities in integrating the positions. This leads to accelerations, velocities and positions not being stored at the same time t. Even though the leap-frog algorithm has better (smaller) errors than the original Verlet algorithm, the problem with velocities does not make it completely satisfactory. The velocity Verlet algorithm uses the same idea as the leap-frog algorithm but it has been developed such that positions, velocities and accelerations are all stored at the same time t, making it time reversible [72].

Anisotropic particles introduce new challenges for handling forces and for integrating the equations of motion. Solving the equations of motion for rotational degrees of freedom give rise to a new constraint between the direction of the rotational velocity and orientation of the particle, namely they must be constrained to be perpendicular to each other [75]. Leap-frog and Velocity Verlet algorithms for non-spherical sites are presented in reference [75].

MD is used throughout this thesis work. In chapters 3 and 4, it is used as a stand alone method. In chapter 5 it is combined with Stochastic Rotational dynamics. The basis for this will be introduced in this chapter in section 2.2.5. Chapter 6 presents simulations with relatively new advanced sampling technique Statistical Temperature MD [76], where standard molecular dynamics is the underlying method. Finally in chapter 7, MD is combined with replica exchange method [77, 78]. The next section describes how MD can be realised in different ensembles, corresponding to fluctuations in desired thermodynamic variables.

MD in different ensembles

The natural ensemble for MD is the micro-canonical, NVE, in which the number of particles, N, volume, V and the total energy E are conserved [6]. If different ensembles are desired, for example the const-NVT or const-NPT, a thermostat or thermo- and barostat respectively, needs to be applied to keep the temperature, T, and the pressure,P, constant thus allowing the sampling of energy or energy and volume V phase space, respectively. Popular choices for thermostats include the Berendsen [79], Andersen [80] and Nosè-Hoover thermostats [81]. In the Berendsen method the old velocities are scaled to new velocities, $\mathbf{v}_{new} = \chi \mathbf{v}_{old}$, by a scaling parameter given by,

$$\chi = \left[1 + \frac{\delta t}{\tau}\left(\frac{T}{T_0} - 1\right)\right]^{\frac{1}{2}}, \tag{2.20}$$

where T is the current temperature, T_0 is desired temperature, δt is timestep and τ is a time constant. The Berendsen thermostat is very efficient in reaching the desired temperature. However, at equilibrium the temperature is expected to fluctuate around the correct value, and therefore the damping by thermostat might lead to incorrect sampling of the canonical ensemble.

In the other two methods, due to Andersen and Nosè-Hoover, the temperature is kept constant by collisions with a heat bath. In the Andersen method, the collision with a heat bath is achieved by giving to a particle (or particles) a new velocity randomly sampled from a Maxwell-Boltzmann distribution corresponding to the desired temperature. The Nosè-Hoover algorithm works in a similar fashion. The main difference is that instead of just replacing the old velocities, energy is allowed to flow between the heat bath and the system.

For keeping the pressure constant, there exists a Berendsen barostat [79], which works on same principle as his thermostat. The box volume, V, and therefore particle centre of mass coordinates, $\boldsymbol{r}$, are scaled according to a scaling factor derived from the rate of pressure change. The scaling factor takes the form

$$\mu = 1 - \frac{\beta \delta t}{3\tau_p}\left(P_0 - P\right), \tag{2.21}$$

where β is the isothermal compressibility, P_0 is the desired pressure and P is the current pressure calculated for example through virial equation. Toxvaerd [82] developed a barostat which works in a similar fashion to the Nosè-Hoover thermostat. Here a friction coefficient is introduced so that the analogue to the heat bath would be a piston which interacts with the system to keep the pressure constant.

Pressure can also be kept constant by using a simple Monte Carlo move performed periodically after a certain number of MD steps. Here a new volume would be generated by adding a small (random) volume perturbation term, $\Delta V \in [-\Delta V_{\mathrm{max}},\, \Delta V_{\mathrm{max}}]$, to the old volume as, $V_{\mathrm{new}} = V_{\mathrm{old}} + \Delta V$. Centre of mass vectors would be scaled as $\boldsymbol{r}_{\mathrm{new}} = \left(V_{\mathrm{new}}/V_{\mathrm{old}}\right)^{1/3} \boldsymbol{r}_{\mathrm{old}}$. After evaluating the potential energy change, the new volume could be accepted by a MC volume acceptance criteria as presented in section (2.2.1).

2.2.3 Dissipative particle dynamics

Dissipative particle dynamics (DPD) was originally formulated by Hoogerbrugge and Koelman in 1992 [83]. It can be understood to be a type of MD with additional forces to work as a thermostat. DPD was originally developed to model solvents using soft repulsive pair potentials between individual solvent particles. The thermostat is local and conserves momentum. This leads to the correct hydrodynamics at sufficiently long time and length scales. In the DPD framework the equations of motion are given by a set of stochastic differential equations [84]

$$\begin{aligned} d\boldsymbol{r}_i &= \boldsymbol{v}_i dt, \\ d\boldsymbol{v}_i &= \frac{1}{m_i}\left(\left[\sum_{i\neq j}\left(\boldsymbol{F}^{\mathrm{C}}_{ij}(\boldsymbol{r}_{ij}) + \boldsymbol{F}^{\mathrm{D}}_{ij}(\boldsymbol{r}_{ij},\boldsymbol{v}_{ij})\right)\right] dt + \left[\sum_{i\neq j}\boldsymbol{F}^{\mathrm{R}}_{ij}(\boldsymbol{r}_{ij})\right]\sqrt{dt}\right), \end{aligned} \tag{2.22}$$

where $\boldsymbol{r}_{ij}$ is the vector between the centre of mass of particles i and j, $\boldsymbol{r}_{ij} \equiv \boldsymbol{r}_i - \boldsymbol{r}_j$ and for the centre of mass velocities respectively, $\boldsymbol{v}_{ij} \equiv \boldsymbol{v}_i - \boldsymbol{v}_j$. The first of the three forces, $\boldsymbol{F}^{\mathrm{C}}_{ij}$, is the conservative force normally present in MD simulations, between particles j and i. It can be chosen independently of any other forces. The two other forces, dissipative $\boldsymbol{F}_{ij}^{\mathrm{D}}(\boldsymbol{r}_{ij}, \boldsymbol{v}_{ij})$ and random $\boldsymbol{F}_{ij}^{\mathrm{R}}(\boldsymbol{r}_{ij})$ take the form

$$\begin{aligned} \boldsymbol{F}_{ij}^{\mathrm{D}} &\equiv -\gamma\omega^{D}(r_{ij})(\boldsymbol{v}_{ij} \cdot \hat{\boldsymbol{r}}_{ij})\hat{\boldsymbol{r}}_{ij} \\ \boldsymbol{F}_{ij}^{\mathrm{R}} &\equiv \sigma\omega^{R}(r_{ij})\hat{\boldsymbol{r}}_{ij}\xi_{ij}, \end{aligned} \tag{2.23}$$

where $\hat{\boldsymbol{r}}_{ij} \equiv \boldsymbol{r}_{ij}/r_{ij}$ and ξ_{ij} is a gaussian-distributed random variable around zero with unit variance. In order to achieve momentum conservation, a condition $\xi_{ij} = \xi_{ji}$ is imposed [85]. In order to ensure the desired equilibrium distribution the dissipative and random forces must obey the fluctuation-dissipation relation. It has been shown [86] that the relation $\omega^{\mathrm{D}}(r) = \left[\omega^{\mathrm{R}}(r)\right]^2$ for the weight functions and $\sigma^2 = 2\gamma k_B T^*$ for the strengths of the random and dissipative forces, leads to correct sampling of the canonical ensemble. The latter relation also connects the system temperature $T^* = k_B T/\epsilon$ (with k_B being Boltzmann constant), to the amplitudes σ and γ of the random and dissipative forces. In the most common form of DPD, forces are chosen to be soft and repulsive,

$$\omega(r_{ij}) = \begin{cases} 1 - \frac{r_{ij}}{r_{\mathrm{cut}}} & , \quad r_{ij} < r_{\mathrm{cut}} \\ 0 & , \quad r_{ij} \geq r_{\mathrm{cut}} \end{cases} \tag{2.24}$$

where r_{cut} is a cut off distance and weight functions are defined as $\omega^{\mathrm{D}}(r_{ij}) = \left[\omega^{\mathrm{R}}(r_{ij})\right]^2 = [\omega(r_{ij})]^2$. The conservative force is taken to be $F^{\mathrm{C}}(r_{ij}) = A\omega(r_{ij})$ with the amplitude of the force typically taken to be $A = 25$ [87]. The force of the type described by equation (2.24) corresponds to a potential with quadratic repulsions described by equation (2.13) in section 2.1.2.

Probably the biggest challenge in the practical use of DPD is integrating the equations of motion. There are two main difficulties to be considered [84]; the nature of the dissipative force, *i.e.* it is dependent on pairwise velocities of all the pairs of particles. The second difficulty is related to the stochastic nature of the pair interactions, which then leads to the problem that time reversibility is not guaranteed anymore. A lot of work has been done on developing different integration routines and also comparing different suggestions [84, 87, 88].

DPD is not used in the work presented in this thesis. However, the potential developed in chapter 3, employes a quadratic repulsion typically used in DPD simulations. The next section, 2.2.4, describes an alternative method for momentum conserving thermostat, which can be directly implemented into the conventional MD framework described in section 2.2.2, thus allowing the simulation of non equilibrium phenomena where correct hydrodynamics plays an important role.

2.2.4 Lowe-Andersen thermostat

The dissipative particle dynamics method can be thought of as momentum conserving MD with correct hydrodynamics where the thermostat is coupled to equations of motion with random and dissipative forces. The method allows for the study, of a system in the NVT ensemble. Lowe [85] describes a thermostat which preserves the nice points of DPD (conserving momentum and locality) but which would also be, by construction, a valid Monte Carlo scheme. The Lowe approach does not use any dissipative nor random forces. Newton's equations of motion arising from the conservative pair force, $\boldsymbol{F}^{\mathrm{C}}(r_{ij})$ are integrated using a time step Δt as in normal MD. The thermalisation is carried out for pairwise velocities using the Andersen thermostat [80]: hence the name Lowe-Andersen thermostat.

The Lowe-Andersen thermostat acts on pairs of particles located within an interaction radius R_{T}. The bath collision follows Andersen's idea giving the new relative velocities from a Maxwell Boltzmann distribution for the relative velocities [89]. This is done in such a way that linear momentum is conserved. Further, the heat bath collision is performed only for the relative velocity component parallel to the vector between centres of the two particles. This ensures the conservation of angular momentum [89]. Now for a single pair of particles i and j with velocities $\boldsymbol{v}_i$, $\boldsymbol{v}_j$, masses m_i, m_j and unit separation $\hat{\boldsymbol{r}}_{ij} \equiv \boldsymbol{r}_{ij}/r_{ij}$ with $\boldsymbol{r}_{ij} \equiv \boldsymbol{r}_i - \boldsymbol{r}_j$, heat bath collisions can be written [89]

$$\begin{aligned} \mathbf{v}_i^*(t) &= \begin{cases} \mathbf{v}_i(t) & , \quad \Gamma\Delta t < \zeta_1 \\ \mathbf{v}_i(t) + \left(\frac{\mu_{ij}}{m_i}\right)(\lambda - (\mathbf{v}_i - \mathbf{v}_j)\cdot\widehat{\mathbf{r}}_{ij})\,\widehat{\mathbf{r}}_{ij} & , \quad \Gamma\Delta t \geq \zeta_1 \end{cases} \\ \mathbf{v}_j^*(t) &= \begin{cases} \mathbf{v}_j(t) & , \quad \Gamma\Delta t < \zeta_1 \\ \mathbf{v}_j(t) - \left(\frac{\mu_{ij}}{m_j}\right)(\lambda - (\mathbf{v}_i - \mathbf{v}_j)\cdot\widehat{\mathbf{r}}_{ij})\,\widehat{\mathbf{r}}_{ij} & , \quad \Gamma\Delta t \geq \zeta_1, \end{cases} \end{aligned} \tag{2.25}$$

where $\mu_{ij} \equiv m_i m_j/(m_i + m_j)$ is the reduced mass and $\lambda = \zeta_2\sqrt{(k_B T/\mu_{ij})}$ is a stochastic variable with k_B Boltzmann constant and T the desired temperature. ζ_1 and ζ_2 are random numbers where ζ_1 is uniformly distributed, $\zeta_1 \in [0, 1]$ and ζ_2 gaussian distributed with unit variance and zero mean. This procedure is carried out sequentially for all pairs of particles. It is important to notice that the velocity appearing in right hand side of (2.25) is always the current value. This means that it can itself be a post collisional value from some previous pair [89].

Even though the Lowe-Andersen thermostat was originally introduced as an alternative approach to dissipative particle dynamics it can also be useful in normal MD. It has been showed to perturb systems considerably less at high thermostating rates than the Andersen approach [89]. The Lowe-Andersen thermostat works only at liquid densities. For a gas-like system a different thermostat needs to be chosen. One possibility is the thermostat developed by Stoyanov and Groot [90]. In their method the system is thermostatted either (with probability P) with the pairwise Lowe-Andersen method, or (with probability $1-P$) with the pairwise "Nosé-Hoover" like method described in [90]. Another suggestion has come from Allen and Schmid [91] who derived a true pairwise Nosé-Hoover thermostat. These methods provide the possibility to simulate a wide variety of systems where hydrodynamics plays an important role.

The Lowe-Andersen thermostat is applied, to provide a stochastic element, in some of the state points for the main chain liquid crystalline polymer simulations, presented in chapter 4. In the next section, 2.2.5, another momentum conserving method, Stochastic Rotational Dynamics (SRD), will be introduced. SRD is essentially a mesoscopic method, but it can be combined with a microscopic picture (including conservative forces) as will be described below.

2.2.5 Stochastic rotational dynamics

Stochastic rotational dynamics (SRD) algorithm (also known as multi-particle collision dynamics) introduced by Malevanets and Kapral [92] is a mesoscopic method to the simulation of fluids that correctly incorporates hydrodynamics [93–95]. Considering a fluid composed of particles, i, with mass m, position $\mathbf{r}_i(t)$ and velocity

$\mathbf{v}_i(t)$ at time t, the SRD algorithm can be realised in two steps, streaming and collision. During the streaming step the particle positions are updated at discrete time intervals, δt, similar to molecular dynamics

$$\mathbf{r}_i(t+\delta t) = \mathbf{r}_i(t) + \mathbf{v}_i(t)\delta t. \tag{2.26}$$

At the collision step the SRD particles interact through multiparticle collisions. These collisions locally conserve energy, mass and momentum and are performed by dividing the simulation box into a grid of cubic cells with sides of length a. The velocity for particle i relative to the mean velocity of the cell $\mathbf{v}_{\mathrm{c.m.}}$ is rotated, according to

$$\mathbf{v}_i(t) = \mathbf{v}_{\mathrm{c.m.}}(t) + \mathbf{R}\left[\mathbf{v}_i(t) - \mathbf{v}_{\mathrm{c.m}}(t)\right], \tag{2.27}$$

where $\mathbf{R}$ is a rotation matrix through a fixed angle α, about an axis that is randomly generated at each collision step. The cubic grid can be randomly shifted each collision step to improve the Galilean invariance of the algorithm [93].

Now considering the case where the solute particles are introduced into the SRD bath, a question arises of how to treat the solvent-solute interactions. One choice is to treat the solute particles in the same way as the SRD solvent. Thus, the velocities of the solute are mixed with the solvent through the streaming and collision scheme described above. This approach is valid when the details of the interaction between the solute and the solvent are not important, but maintaining the proper hydrodynamics is the primary concern. This method has been used successfully in variety of applications [96–98]. Another possibility is to allow the SRD solvent to directly interact with the solute particles via a non-bonded interaction such as a Lennard-Jones or Weeks-Chandler-Andersen (WCA) potential. This hybrid molecular dynamics scheme was originally suggested by the original authors of SRD in a follow up paper [99]. Later the description was expanded and applied to colloidal suspension by Padding and Louis [100].

In chapter 5, simulations of model coarse grained surfactants coupled to a SRD solvent will be presented. The results demonstrate the formation of bilayers and micelles at different solvent qualities with a direct observation of the merger of two micelles.

2.3 Analysis of the simulation data

2.3.1 Order parameters

In order to identify different mesophases and phase change state points from computer simulations, tools are needed to measure different kinds of molecular ordering. Order parameters S_2, τ_1 and ψ_6 can be used to measure orientational order, one dimensional translational order and intralayer ordering respectively.

The orientational order parameter, S_2, is the largest eigenvalue of an orientational order tensor [51]

$$Q_{\alpha\beta} = \frac{1}{2N_{\mathrm{GB}}} \sum_{i=1}^{i=N_{\mathrm{G}B}} \left(3u_{i\alpha}u_{i\beta} - \delta_{\alpha\beta}\right), \tag{2.28}$$

where $\hat{\mathbf{u}}_i$ is the unit vector along the long axis of ith particle, α and β are the cartesian axis x, y, z and N_{GB} is the number of anisotropic sites. The orientational order parameter, S_2, can be used to differentiate between an isotropic phase, which has no orientational order and therefore $S_2 \approx 0$, and a nematic phase for which $S_2 \neq 0$. The director of the phase, $\hat{\mathbf{n}}$, can be identified as being the eigenvector corresponding to the largest eigenvalue of the orientational order tensor (2.28). The vector representing the long axis (unique axis) of the molecule can be found by diagonalising the moment of inertia tensor for the corresponding molecule [101]

$$I_{\alpha\beta} = \sum_i m_i \left(\boldsymbol{s}_i^2 \delta_{\alpha\beta} - s_{i\alpha}s_{i\beta}\right) \tag{2.29}$$

where m_i is the mass of the atom i, $\boldsymbol{s}_i$ is the atomic distance vector from the molecules centre of mass and α, β are the cartesian axis. The long axis can be identified as being the eigenvector corresponding to the smallest eigenvalue of the moment of inertia tensor [101].

One dimensional translational order of the centre of masses along the director of the phase can be measured with the parameter [50]

$$\tau_1 = \left|\left\langle \exp\left(2\pi \mathrm{i} r_{\|}/d\right)\right\rangle\right|, \tag{2.30}$$

where $r_{\|}$ is the projection of centre of mass coordinate along the director $\hat{\boldsymbol{n}}$ and d is a yet unknown layer spacing. τ_1 can be obtained by calculating it for a series of layer spacings, $d = d_{\min} \ldots d_{\max}$, and then taking the maximum value of $\left|\left\langle \exp\left(2\pi \mathrm{i} r_{\|}/d\right)\right\rangle\right|$ as the translational order parameter τ_1 [50]. The order parameter can be used to distinguish between a nematic phase with no translational order, $\tau_1 \approx 0$ and a smectic phases with layer structure and $\tau_1 \neq 0$.

Hexagonal intralayer ordering can be measured by using the parameter [50]

$$\psi_6\left(\mathbf{r}_i\right) = \frac{\sum_j w\left(r_{ij}\right)\exp\left(6\mathrm{i}\theta_{ij}\right)}{\sum_j w\left(r_{ij}\right)} \tag{2.31}$$

where the summation runs over the neighbouring particles j of particle i. θ_{ij} is the angle between the projection of the vector, $\mathbf{r}_i - \mathbf{r}_j$, to a plane normal to the director $\hat{\mathbf{n}}$ and a fixed reference axis [50]. To overcome the difficulty of choosing nearest neighbours a cutoff function, $w(r_{ij})$, can be used. Typically it is chosen to be unity for separations smaller than the chosen $r_{\min}$ and zero for separations greater than the chosen $r_{\max}$ with linear interpolation between these values [50]. A bulk bond orientational order parameter can be calculated by averaging the the local parameters (2.31) over all anisotropic particles [51]

$$\psi_6 = \mathrm{Re}\left(\frac{1}{N_{\mathrm{GB}}}\sum_i \psi_6\left(\boldsymbol{r}_i\right)\right). \tag{2.32}$$

With the aid of ψ_6 one can distinguish between a smectic A, with no hexagonal order and therefore $\psi_6 \approx 0$, from phases with intralayer hexagonal order, $\psi_6 \neq 0$, for example a smectic B or a crystal B phase.

2.3.2 Pair correlation functions

Calculation of pair correlation functions allows for the characterisation of the structure of a bulk phase. The pair distribution function, $g(r)$, gives the probability of

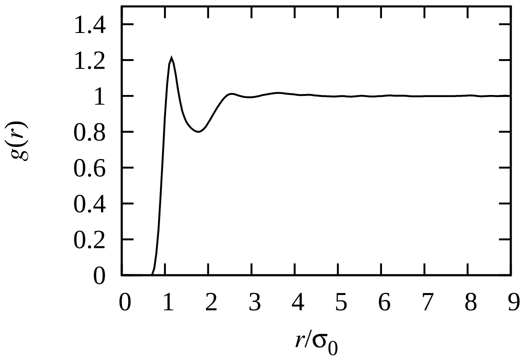

Figure 2.3: An example of a typical pair distribution function, $g(r)$, for an isotropic liquid.

finding a pair of particles at a distance, r, apart, compared to an ideal gas of the same density. Any deviations of $g(r)$ from unity means that there exists correlation between particles, typically arising from the potential energy interactions [68]. Thus it does provide information of the local structure of the liquid. The pair distribution function is defined as [102]

$$g(r) = V/N^2 \langle \sum_i \sum_{j \neq i} \delta(\mathbf{r} - \mathbf{r}_{ij}) \rangle, \tag{2.33}$$

where, V and N, are the volume and total number of particles, respectively. In computer simulations $g(r)$ can be calculated by replacing the $\delta(\mathbf{r} - \mathbf{r}_{ij})$ function in equation (2.33) by a small distance Δr and accumulating histogram bins with a distance $r = \text{int}(r_{ij}/\Delta r)$ [102]. For an isotropic liquid it is typical that $g(r)$ shows only a peak at separations corresponding to nearest neighbour interactions as shown in figure 2.3.

For characterisation of mesophases with orientational or translational order, it is useful to define pair distribution functions as functions of these quantities. A distribution function, $g_{||}(r)$ [103,104] can be realised by considering distances r projected along the system director $\hat{\mathbf{n}}$, defined in the previous section 2.3.1. In a layered mesophase, such as a smectic or lamellar, an intra-layer pair distribution function $g_l(r_\perp)$ can be defined, where only particles inside the same layer are considered with a distance perpendicular to the system director.

2.4 Coarse Graining of complex molecules

In coarse grained (CG) multi-site models the underlying "real molecule" is coarse-grained into smaller sub-units, super atoms, which then are connected with simple springs to represent bonds, bond angles and dihedral angles in a similar fashion to atomistic models [105]. The idea is to coarsen the picture, *i.e.* get rid of details which are less important for the system under study, but still preserve enough chemical and physical characteristics to provide a correct description of the behaviour occurring on the length scale of interest. With effective coarse graining time and length scales can be bridged, in the best cases by several orders of magnitude, and still preserve the key features of the molecular system. This then provides the possibility to study, for example, self assembly of supramolecular systems or to simulate spontaneous mesophase formation of complex supermolecules. For liquid crystal simulations there has been very little development in a systematic coarse-graining scheme to map between the atomistic and CG world. This is now starting to change with recent studies by Peter and co-workers [106]. However, in the field of polymer simulations, as discussed in references [107–111], there exists a number of coarse graining schemes, which should be applicable to liquid crystals [46].

The first step of coarse graining is to define the level of coarsening. This means defining how many real atoms are coarse grained into one super atom. In polymer systems it is typical to use a 10 to 1 coarse grained mapping, which means ten real atoms are coarse grained into one super atom [112]. Other important considerations include the position of the super atoms, for example at the centre of mass of the underlying real atoms or at the geometrical centre. The latter requires a careful choice of the correct regions and therefore the shape of the CG super atom. For simple liquid crystals and polymers choosing the regions might be a fairly simple task but when desiring to coarse grain large molecules with complex structures this becomes a less trivial task. Gohlke and Thorpe [113] present a "natural" way of coarse graining large biomolecules using rigid regions identified within the molecule as coarse grained elements. This gives the possibility of concentrating computational efforts to simulation of flexible connections between rigid units, which can be assumed to dominate the biomolecular motion [113].

The next, most important, step is to parametrise the intra- and intermolecular interactions. This problem is far from trivial and some level of compromise is almost always needed. There exist multiple methods for defining the parameters for the coarse grained force field, ranging from simple potentials of mean force or a simplex method to fit Lennard-Jones parameters while comparing the system density (as a function of these parameters) to experimentally observed density, to dynamic mapping, for example comparing a chain diffusion between CG and atomistic simulation [107] (and references therein). The choice of method depends on the system under study and what properties are desired to be reproduced. For example, studying the formation of equilibrium structures, *i.e.* mesophase formation, in a complex thermotropic liquid crystal most likely requires a different approach to studying the centre of mass diffusion of a polymer system at constant temperature.

A fairly simple, but still effective method for coarse graining includes the use of a potential of mean force. The idea is to consider a Boltzmann probability distribution [114]

$$P(\epsilon_i(r)) = q^{-1} e^{-\epsilon_i(r)/kT} \tag{2.34}$$

where $q = \sum_i^\infty e^{-\epsilon_i(r)/kT}$ is a partition function involving all possible states. Now considering a distribution function, $P(x)$, with degrees of freedom, x, obtained from atomistic simulation of a bulk system or from experiments, one can see that the underlying “potential of mean force” can be solved by Boltzmann inversion. This gives [112]

$$A(x) = -kT \ln [qP(x)] = -kT \ln [P(x)] + \text{constant}. \tag{2.35}$$

The resulting quantity, $A(x)$, is not a true potential energy but a free energy [112]. It can be used as a coarse grained potential but it has two main problems. Firstly, it includes effects from other (neglected) degrees of freedom. Secondly, (a problem that is common to all effective coarse graining schemes) it is not independent of temperature nor density. It still can be very good approximation for the potential energy of stiff interactions where the entropic contribution of the free energy is small. A good example of this is bond stretching between two adjacent superatoms [112].

For intermolecular pair interactions the use of a potential of mean force is particularly problematic. It is correct only for the theoretical case of zero density $\rho = 0$. In the intermolecular case the distribution function in question is the pair correlation function, $g(r)$, between particles. In order to find an effective CG pair potential which would reproduce, for very high precision, an atomistic $g(r)$, an *iterative Boltzmann inversion* method has been developed [109]. The idea is to iteratively alter the pair potential by using the difference between the current pair correlation function, $g_i(r)$, and the target function $g_{\text{target}}(r)$. It has been shown to converge in just a few iterations and reproduce the target function within the line width [109]. The main problem in this method is that $g_{\text{target}}(r)$ is state point dependent. In other words, if, for example, a simulation was carried out at a different temperature or a different density, then (strictly speaking) a new potential has to be defined.

Despite the short comings of the potential of mean force method to define the intermolecular interactions it can still be used to find out features of the underlying true pair potential. It has been used to study the mapping of self-avoiding walk polymers onto a fluid of soft particles [115]. The effective pair potential between the centre of mass was achieved by inverting the pair distribution function between the centres of mass of the original polymer chains. The key observation was that the resulting effective potential was ultra soft in nature, meaning it had a finite energy at zero separation, similar to the quadratic equation (2.13) in section 2.1.2. Guerrault *et al.* [116] did DPD simulations on coarse grained polymer melts. They coarse grained polyethylene (PE) and *cis*-polybutadene (*cis*-PB) by using the potential of mean force directly as the potential. Their coarse graining procedure showed that for the coarse graining level of eight monomers per super atom, $\lambda = 8$, for PE or four monomers per super atom, $\lambda = 4$, for *cis*-PB, the pair distribution functions shows a non-zero value at zero separation *i.e.* the coarse grained beads can overlap. Both of these results imply that the use of potentials of an ultrasoft nature might be useful also in liquid crystal simulations.

It should be stressed also that in some cases valuable insight can also be provided by rather cruder coarse grained models. Here, rather than attempting to directly derive CG potential from an atomistic description, it is possible instead to use coarse grained models which regenerate key features of a complex molecule. Examples include MD and DPD simulations of AB diblock copolymers, where it has proved possible to predict key phases formed by the use of a very simple model, with favourable interaction between like beads and repulsion between unlike beads [117–119]. For mesogenic systems useful insight has been provided by the work of Glotzer and co-workers [120–125] who studied mesophase behaviour of models consisting of rigid and flexible segments in various topologies, including end and laterally tethered nanorods and V-shaped particles.

In the next chapter a new coarse grained model for mesogenic system is developed. It is shown to work for single site systems producing phase diagram for model liquid crystals at low computational cost and qualitatively compared to Gay-Berne systems. It is then used as a part of multi-site model to simulate the self-assembly of a multipedal liquid crystalline molecule.

Chapter 3

An orientation-dependent potential model for a soft spherocylinder

3.1 Introduction

Single site models for pair interactions in molecular fluids have been very successful in describing the behaviour of mesogens and in studying liquid crystal phases [126]. They are comparably cheap to simulate but still manage to capture the essential physics of underlying real mesogens including, for example, excluded volume effects. Especially interesting models are rigid anisotropic models for modelling elongated or rodlike mesogens. These mesogens are of great interest due to their applicability in a wide range of biological and technological applications. Therefore different models have been introduced to explore their properties via computer simulations [127,128].

One interesting and widely studied model is to use a single site rigid potential with ellipsoidal symmetry. The most popular choice of model in this category is the Gay-Berne (GB) model [43], which has been described in more detail in section 2.1.1. It has been extensively studied, can be used with various parametrisations to model different single site mesogens and has been summarised in a recent review [126] and a book chapter [129]). It has been found to exhibit isotropic (I), nematic (N), smectic A (SmA) and smectic B (SmB) or crystal phases (Cr) [50, 51] for certain parametrisations.

There have also been studies of chain models composed of spherical sites bonded to each other to form a rod-like molecules. Here intermolecular pair interactions can be modelled by hard spheres [130] or soft spheres [131]. For many cases calamitic mesogens, or especially the rigid core of calamitic mesogen might be better modelled by spherocylinder model [67] which has been described in more detail in section 2.1.2. Spherocylinder potentials include hard particle models, hard spherocylinder (HSR) [57,61,64,132] and square-well [133,134] models. Soft particle models include a repulsive Kihara model *i.e.* soft repulsive (SRS) models [66, 132, 135] and the Kihara fluid itself [136]. There is also a model of the Gay-Berne-Kihara (GBK) fluid which employs the functional form of the Gay-Berne attractive well, giving the potential an anisotropic well depth [67]. A recent study [60] considered very soft repulsive spherocylinder model with finite energy at zero separation. The potential used was a repulsive quadratic potential, similar to those typically used in dissipative particle dynamics simulations. This very soft potential provides the possibility of using longer time step and therefore allowed more efficient sampling of the time- and lengths scales.

Despite the success of GB and spherocylinder models they possess some slightly unphysical characteristics. Namely the density changes associated with mesophase formation are, in worst cases, orders of magnitude greater than in real small organic molecules. The large density change at a transition is true for colloidal systems but usually not for thermotropic mesogens. Incidently, as shown in simulation studies of flexible molecules, real molecules can change conformation at the phase transition [137], which partly explain the smaller density change.

Another possible problem could be caused by the relatively large aspect ratios of single site anisotropic particles, due to the lack of anisotropic attractive forces. Fairly large elongations, L/D, must be used to achieve ordering of mesophases as mesophase formation relies on excluded volume effects and the competition between translational and rotational entropy. The former, has a maximum when the centre of mass movement is not restricted and the latter has a maximum when molecules rotate freely [46]. This can be especially a problem for ultra soft potentials, as making the potential very soft reduces the excluded volume effects.

The work presented in the remaining part of this chapter presents a new type of soft-core potential model for a spherocylinder. This new model has some nice features: it has adjustable attractive interactions. Further, it reduces the barriers in the free energy landscape and allows the use of considerably larger time step, thus leading to considerably faster sampling of phase space when compared with conventional models. This is especially convenient when modelling the bulk melt of complex multi-site molecules. It goes smoothly to zero at a cut-off distance, which is an essential requirement for a potential used in MD framework. The adjustable attractive interactions allow the parametrisation to favour different configurations between pairs of particles.

The potential and the adjustable parameters are introduced in section 3.2. Derivation of forces and torques needed for molecular dynamics simulations (MD) are presented in section 3.3 and results of MD simulations for two single site systems are reported in section 3.4. Variants of the potential can also be linked together to produce more complicated molecular structures. In section 3.5, as an example, results are provided for a model multipedal liquid crystal, which has eight liquid crystalline groups linked to a central core via semiflexible chains.[1]

3.2 A new soft-core potential model for anisotropic sites

The simple idea behind the new potential model is to use the typical quadratic form used in DPD simulations (section 2.2.3), $U^*_{\text{max}}(1-d^*)^2$, for the repulsive part of the potential and add a fourth order term, $U^*_{\text{attr}}(1-d^*)^4$, to control the attractive interaction. By making the magnitude of the attractive part, U^*_{attr}, angle dependent, an anisotropic well depth can be realised. Now a piecewise potential between particles

---

[1] Results of this chapter has been published as: A new anisotropic soft-core model for the simulation of liquid crystal mesophases. J. S. Lintuvuori and M. R. Wilson J. Chem. Phys. **128**, 044906 (2008).

i and j can be constructed

$$U^*(d) = \begin{cases} U^*_{\text{max}}\left(1-d^*\right)^2 + \epsilon^* & , \quad d^* < 1 \\ U^*_{\text{max}}\left(1-d^*\right)^2 - U^*_{\text{attr}}\left(\hat{\mathbf{r}}_{ij}, \hat{\mathbf{e}}_i, \hat{\mathbf{e}}_j\right)\left(1-d^*\right)^4 + \epsilon^* & , \quad 1 \leq d^* < d^*_{\text{cut}} \\ 0 & , \quad d^* \geq d^*_{\text{cut}} \end{cases} \tag{3.1}$$

where the notations U^* and d^* imply the the scaling of the energy and the line segment distance, $U^* \equiv U/\epsilon_0$, and $d^* \equiv d/\sigma_0$, respectively with $\sigma_0 = D$. ϵ^* is the associated well depth for the configuration. The magnitude of the attractive part, $U^*_{attr}\left(\hat{\mathbf{r}}_{ij}, \hat{\mathbf{e}}_i, \hat{\mathbf{e}}_j\right)$, as a function of the orientation of the vector between the centre of masses, $\hat{\mathbf{r}}_{ij}$, and the orientations of particles i and j, $\hat{\mathbf{e}}_i$, $\hat{\mathbf{e}}_j$ can be written as

$$U^*_{attr}\left(\hat{\mathbf{r}}_{ij}, \hat{\mathbf{e}}_i, \hat{\mathbf{e}}_j\right) = U^*_{attr} - \Psi\left(\hat{\mathbf{r}}_{ij}, \hat{\mathbf{e}}_i, \hat{\mathbf{e}}_j\right), \tag{3.2}$$

where $\Psi\left(\hat{\mathbf{r}}_{ij}, \hat{\mathbf{e}}_i, \hat{\mathbf{e}}_j\right)$ is given by [138]

$$\Psi\left(\hat{\mathbf{r}}_{ij}, \hat{\mathbf{e}}_i, \hat{\mathbf{e}}_j\right) = 5\epsilon_1 P_2\left(\hat{\mathbf{e}}_i \cdot \hat{\mathbf{e}}_j\right) + 5\epsilon_2\left[P_2\left(\hat{\mathbf{r}}_{ij} \cdot \hat{\mathbf{e}}_i\right) + P_2\left(\hat{\mathbf{r}}_{ij} \cdot \hat{\mathbf{e}}_j\right)\right]. \tag{3.3}$$

Here $P_2(x) = (3x^2 - 1)/2$ is the second order Legendre polynomial. It can also be noted that this form satisfies head to tail, $\hat{\mathbf{e}}_i = -\hat{\mathbf{e}}_i$, symmetry [138], typical of spherocylinders and most nematogens.

The well depth for a particular configuration, ϵ^*, and cut off distance, d^*_{cut}, can be solved from the requirements that the potential and its first derivative must go to zero at a cut-off, $U^*\left(d^* = d^*_{\text{cut}}\right) = 0$ and $U'^*\left(d^* = d^*_{\text{cut}}\right) = 0$. From these the expressions follow:

$$\epsilon^* \equiv \epsilon^*\left(\hat{\mathbf{r}}_{ij}, \hat{\mathbf{e}}_i, \hat{\mathbf{e}}_j\right) = -\frac{U^{*^2}_{\text{max}}}{4U^*_{\text{attr}}\left(\hat{\mathbf{r}}_{ij}, \hat{\mathbf{e}}_i, \hat{\mathbf{e}}_j\right)}, \tag{3.4}$$

and

$$d^*_{\text{cut}} \equiv d^*_{\text{cut}}\left(\hat{\mathbf{r}}_{ij}, \hat{\mathbf{e}}_i, \hat{\mathbf{e}}_j\right) = 1 + \sqrt{\frac{1}{2}\frac{U^*_{\text{max}}}{U^*_{\text{attr}}\left(\hat{\mathbf{r}}_{ij}, \hat{\mathbf{e}}_i, \hat{\mathbf{e}}_j\right)}}. \tag{3.5}$$

This resulting potential has the nice features of being continuous and having a continuous first derivative which are required for a force calculation in MD. Moreover, it can be tuned to model different type of interactions by altering its four parameters (U^*_{max}, U^*_{attr}, ϵ_1 and ϵ_2). The parameter U^*_{max} gives the interaction energy when particles are fully overlapping. The ratio $U^*_{\mathrm{max}}/U^*_{\mathrm{attr}}$ controls the well depth and ϵ_1 and ϵ_2 can be used to control the well depth anisotropy.

3.3 Force calculation

Equations of motion

For a linear rigid molecule the torque of the rotation can be written [72]

$$\boldsymbol{\tau}_i = \hat{\mathbf{e}}_i \times \mathbf{g}_i \tag{3.6}$$

where $\hat{\mathbf{e}}_i$ is the orientation of the long axis and $\mathbf{g}_i$ is the so called “gorque” on particle i due to the intermolecular forces from other particles acting on particle i, $\mathbf{g}_i = -\nabla_{\hat{\mathbf{e}}_i} U_{ij}$ [139]. $\mathbf{g}_i$ can be replaced by its component perpendicular to the molecular symmetry axis, without affecting the torque (3.6). So now the torque can be rewritten [72]

$$\boldsymbol{\tau}_i = \hat{\mathbf{e}}_i \times \mathbf{g}_i^{\perp}, \tag{3.7}$$

where the perpendicular component $\mathbf{g}_i^{\perp}$ is defined as

$$\mathbf{g}_i^{\perp} = \mathbf{g}_i - (\mathbf{g}_i \cdot \hat{\mathbf{e}}_i)\,\hat{\mathbf{e}}_i. \tag{3.8}$$

Now the rotational equations of motion can be written as functions of the orientation $\hat{\mathbf{e}}_i$ and rotational velocity $\mathbf{u}_i$ as [72]

$$\begin{aligned} \tfrac{d}{dt}\widehat{\mathbf{e}}_i &= \mathbf{u}_i, \\ \tfrac{d}{dt}\mathbf{u}_i &= \mathbf{g}_i^{\perp}/I_i + \lambda\widehat{\mathbf{e}}_i, \end{aligned} \tag{3.9}$$

where I_i is the moment of inertia and λ is Lagrange multiplier which is used to constrain the bond length and therefore molecule length to be a constant of the motion. The translational motion for this linear molecule straight-forwardly obeys

Newton's 2nd law

$$m_i \frac{d^2}{dt^2}\mathbf{r}_i = \mathbf{f}_i. \tag{3.10}$$

Equations (3.9) and (3.10) define the dynamics of a linear molecule [139] and can be solved by, for example, using leap-frog or velocity Verlet algorithms for anisotropic particles [75] to obtain the particle trajectories as function of time, t. To be able to do that, the pairwise additive forces and torques/gorques must be derived from the underlying anisotropic pair potential.

Forces and Torques

Considering an anisotropic pair potential, $U_{ij} \equiv U_{ij}\left(\mathbf{r}_{ij},\ \hat{\mathbf{e}}_i,\ \hat{\mathbf{e}}_j\right)$, of particles i and j, with orientations $\hat{\mathbf{e}}_i$ and $\hat{\mathbf{e}}_j$ and vector $\mathbf{r}_{ij}$ connecting the centres of mass, the force on molecule i due to the molecule j can be written

$$\mathbf{f}_{ij} = -\nabla_{\mathbf{r}_{ij}} U_{ij}\left(\mathbf{r}_{ij},\ \hat{\mathbf{e}}_i,\ \hat{\mathbf{e}}_j\right). \tag{3.11}$$

With help of the chain rule, the following expression can be obtained [139]

$$\mathbf{f}_{ij} \;=\; -\left(\frac{\partial U_{ij}}{\partial r_{ij}}\right)\nabla_{\mathbf{r}_{ij}} r_{ij} - \sum_{\alpha=i,j}\left(\frac{\partial U_{ij}}{\partial\left(\widehat{\mathbf{r}}_{ij}\cdot\widehat{\mathbf{e}}_\alpha\right)}\right)\nabla_{\mathbf{r}_{ij}}\left(\widehat{\mathbf{r}}_{ij}\cdot\widehat{\mathbf{e}}_\alpha\right). \tag{3.12}$$

Using the relation [139]

$$\nabla_{\mathbf{r}_{ij}}\left(\hat{\mathbf{r}}_{ij}\cdot\hat{\mathbf{e}}_\alpha\right) = -\left(\hat{\mathbf{r}}_{ij}\cdot\hat{\mathbf{e}}_\alpha\right)\frac{\mathbf{r}_{ij}}{r_{ij}^2} + \frac{\hat{\mathbf{e}}_\alpha}{r_{ij}}, \tag{3.13}$$

the force, $\mathbf{f}_{ij}$ can be written

$$\mathbf{f}_{ij} = -\left(\frac{\partial U_{ij}}{\partial r_{ij}}\right)\widehat{\mathbf{r}}_{ij} - \sum_{\alpha=i,j}\left(\frac{\partial U_{ij}}{\partial\left(\widehat{\mathbf{r}}_{ij}\cdot\widehat{\mathbf{e}}_\alpha\right)}\right)\left(\frac{\widehat{\mathbf{e}}_\alpha}{r_{ij}} - \mathbf{r}_{ij}\frac{\left(\widehat{\mathbf{r}}_{ij}\cdot\widehat{\mathbf{e}}_\alpha\right)}{r_{ij}^2}\right). \tag{3.14}$$

Similarly the gorque can be solved from $\mathbf{g}_{ij} = -\nabla_{\hat{\mathbf{e}}_i} U_{ij}$, to obtain [139]

$$\begin{aligned}
\mathbf{g}_{ij} \;&=\; -\left[\left(\frac{\partial\left(\hat{\mathbf{r}}_{ij}\cdot\hat{\mathbf{e}}_i\right)}{\partial\hat{\mathbf{e}}_i}\right)\left(\frac{\partial U_{ij}}{\partial\left(\hat{\mathbf{r}}_{ij}\cdot\hat{\mathbf{e}}_i\right)}\right) + \left(\frac{\partial\left(\hat{\mathbf{e}}_i\cdot\hat{\mathbf{e}}_j\right)}{\partial\hat{\mathbf{e}}_i}\right)\left(\frac{\partial U_{ij}}{\partial\left(\hat{\mathbf{e}}_i\cdot\hat{\mathbf{e}}_j\right)}\right)\right] \\
&=\; -\left[\hat{\mathbf{r}}_{ij}\left(\frac{\partial U_{ij}}{\partial\left(\hat{\mathbf{r}}_{ij}\cdot\hat{\mathbf{e}}_i\right)}\right) + \hat{\mathbf{e}}_j\left(\frac{\partial U_{ij}}{\partial\left(\hat{\mathbf{e}}_i\cdot\hat{\mathbf{e}}_j\right)}\right)\right].
\end{aligned} \tag{3.15}$$

It should be noticed that Newton's third law, $\mathbf{f}_{ij} = -\mathbf{f}_{ji}$, does not apply to gorques, *i.e.* $\mathbf{g}_{ij} \neq -\mathbf{g}_{ji}$. Now equations (3.14) and (3.15) can be used to solve the forces and gorques arising from the anisotropic pair potential (3.1).

For spherocylinders the potential, U_{ij}, is written in the terms of the shortest distance between the line segments, d_{ij}. The latter can be efficiently calculated using the algorithm of Vega and Lago [140]. Consequently, the first part of the force equation (3.14) with the partial derivative, $-\left(\partial U_{ij}/\partial r_{ij}\right)\hat{\mathbf{r}}_{ij}$, will now be written in terms of d_{ij} and the unit vector along the direction of the minimum distance of between the line segments, $\hat{\mathbf{d}}_{ij}$. Now the force acting on the centre of mass to particle i due to particle j can be written

$$\mathbf{f}_{ij}^{d_{ij}}(\mathbf{d}_{ij}) = \begin{cases} 2U^*_{\text{max}}\left(1 - d^*_{ij}\right)\widehat{\mathbf{d}}_{ij} & , \quad d^*_{ij} < 1 \\ 2U^*_{\text{max}}\left(1 - d^*_{ij}\right)\widehat{\mathbf{d}}_{ij} - 4U^*_{\text{attr}}\left(\hat{\mathbf{r}}_{ij}, \hat{\mathbf{e}}_i, \hat{\mathbf{e}}_j\right)(1 - d^*_{ij})^3\widehat{\mathbf{d}}_{ij} & , \quad 1 \leq d^*_{ij} < d^*_{\text{cut}} \\ 0 & , \quad d^*_{ij} \geq d^*_{\text{cut}}. \end{cases} \tag{3.16}$$

The gorques can be evaluated through the cross product using the relation $\boldsymbol{\tau} = \mathbf{l} \times \mathbf{f}$ for torque, where $\mathbf{l}$ is the vector between the centre of mass and the point where the force $\mathbf{f}_{ij}^{d_{ij}}$ is acting on the line segment and equation (3.6). By definition, [140] $\mathbf{l}$, for particles, i and j is given by $\mathbf{l}_i = \tau\hat{\mathbf{e}}_i$ and $\mathbf{l}_j = \mu\hat{\mathbf{e}}_j$, with $\tau, \mu \in \left[-\frac{1}{2}\frac{L}{D}, \frac{1}{2}\frac{L}{D}\right]$. Now comparing with equation (3.6) we can see that gorques arising from $\mathbf{f}_{ij}^{d_{ij}}$, can be calculated as

$$\begin{aligned} \mathbf{g}_{ij}^{d_{ij}} &= \tau\mathbf{f}_{ij}^{d_{ij}} \\ \mathbf{g}_{ji}^{d_{ij}} &= -\mu\mathbf{f}_{ij}^{d_{ij}}. \end{aligned} \tag{3.17}$$

The second part of equation (3.14) can be calculated with help of the following results, remembering $\partial/\partial x\left[P_2(x)\right] = 3x$,

$$\frac{\partial}{\partial(\hat{\mathbf{r}}_{ij}\cdot\hat{\mathbf{e}}_i)}\Psi(\hat{\mathbf{r}}_{ij},\ \hat{\mathbf{e}}_i,\ \hat{\mathbf{e}}_j) = \frac{\partial}{\partial(\hat{\mathbf{r}}_{ij}\cdot\hat{\mathbf{e}}_i)}\left[5\epsilon_2 P_2(\hat{\mathbf{r}}_{ij}\cdot\hat{\mathbf{e}}_i)\right] = 15\epsilon_2(\hat{\mathbf{r}}_{ij}\cdot\hat{\mathbf{e}}_i), \tag{3.18}$$

and

$$\begin{aligned}\frac{\partial}{\partial(\hat{\mathbf{r}}_{ij}\cdot\hat{\mathbf{e}}_i)}\epsilon^*(\hat{\mathbf{r}}_{ij},\ \hat{\mathbf{e}}_i,\ \hat{\mathbf{e}}_j) &= \frac{\partial}{\partial(\hat{\mathbf{r}}_{ij}\cdot\hat{\mathbf{e}}_i)}\left[-\frac{U^{*2}_{\mathrm{max}}}{4\left(U^*_{\mathrm{attr}}-\Psi(\hat{\mathbf{r}}_{ij},\ \hat{\mathbf{e}}_i,\ \hat{\mathbf{e}}_j)\right)}\right] \\ &= -\frac{U^{*2}_{\mathrm{max}}\left(4\times 15\epsilon_2(\hat{\mathbf{r}}_{ij}\cdot\hat{\mathbf{e}}_i)\right)}{\left[4\left(U^*_{\mathrm{attr}}-\Psi(\hat{\mathbf{r}}_{ij},\ \hat{\mathbf{e}}_i,\ \hat{\mathbf{e}}_j)\right)\right]^2}. \end{aligned} \tag{3.19}$$

Now the force due to the second part of the equation (3.14) can be written

$$\mathbf{f}^{r_{ij}}_{ij} = \begin{cases} -\sum_{\alpha=i,j}\left(-\frac{U^{*2}_{\mathrm{max}}(4\times 15\epsilon_2(\widehat{\mathbf{r}}\cdot\widehat{\mathbf{e}}_\alpha))}{[4(U^*_{\mathrm{attr}}-\Psi(\hat{\mathbf{r}}_{ij},\hat{\mathbf{e}}_i,\hat{\mathbf{e}}_j))]^2}\right)\left(\frac{\widehat{\mathbf{e}}_\alpha}{\mathbf{r}_{ij}}-\mathbf{r}_{ij}\frac{(\widehat{\mathbf{r}}_{ij}\cdot\widehat{\mathbf{e}}_\alpha)}{r^2_{ij}}\right) & , \quad d^*_{ij}<1 \\ \begin{cases} -\sum_{\alpha=i,j}\left(15\epsilon_2\left(\widehat{\mathbf{r}}\cdot\widehat{\mathbf{e}}_\alpha\right)\left(1-d^*_{ij}\right)^4\right. \\ \left.-\frac{U^{*2}_{\mathrm{max}}(4\times 15\epsilon_2(\widehat{\mathbf{r}}\cdot\widehat{\mathbf{e}}_\alpha))}{[4(U^*_{\mathrm{attr}}-\Psi(\hat{\mathbf{r}}_{ij},\hat{\mathbf{e}}_i,\hat{\mathbf{e}}_j))]^2}\right)\left(\frac{\widehat{\mathbf{e}}_\alpha}{\mathbf{r}_{ij}}-\mathbf{r}_{ij}\frac{(\widehat{\mathbf{r}}_{ij}\cdot\widehat{\mathbf{e}}_\alpha)}{r^2_{ij}}\right) \end{cases} & , \quad 1\le d^*_{ij}<d^*_{cut} \\ 0 & , \quad d^*_{ij}\ge d^*_{cut} \end{cases} \tag{3.20}$$

The total force on particle i due to particle j can now be solved as $\mathbf{f}_{ij} = \mathbf{f}^{d_{ij}}_{ij} + \mathbf{f}^{r_{ij}}_{ij}$, where components, $\mathbf{f}^{d_{ij}}_{ij}$ and $\mathbf{f}^{d_{ij}}_{ij}$, are defined by equations (3.16) and (3.20), respectively.

Similarly the gorque (3.15) acting on particle i due to particle j can be solved with help of equations (3.18) and (3.19) to give

$$\mathbf{g}^{r_{ij}}_{ij} = \begin{cases} \begin{cases} -\widehat{\mathbf{r}}_{ij}\left(-\frac{U^{*2}_{\mathrm{max}}(4\times 15\epsilon_2(\widehat{\mathbf{r}}_{ij}\cdot\widehat{\mathbf{e}}_i))}{[4(U^*_{\mathrm{attr}}-\Psi(\hat{\mathbf{r}}_{ij},\hat{\mathbf{e}}_i,\hat{\mathbf{e}}_j))]^2}\right) \\ -\widehat{\mathbf{e}}_j\left(-\frac{U^{*2}_{\mathrm{max}}(4\times 15\epsilon_1(\widehat{\mathbf{e}}_i\cdot\widehat{\mathbf{e}}_j))}{[4(U^*_{\mathrm{attr}}-\Psi(\hat{\mathbf{r}}_{ij},\hat{\mathbf{e}}_i,\hat{\mathbf{e}}_j))]^2}\right) \end{cases} & , \quad d^*_{ij}<1 \\ \begin{cases} -\widehat{\mathbf{r}}_{ij}\left(15\epsilon_2\left(\widehat{\mathbf{r}}_{ij}\cdot\widehat{\mathbf{e}}_i\right)\left(1-d^*_{ij}\right)^4-\frac{U^{*2}_{max}(4\times 15\epsilon_2(\widehat{\mathbf{r}}_{ij}\cdot\widehat{\mathbf{e}}_i))}{[4(U^*_{\mathrm{attr}}-\Psi(\hat{\mathbf{r}}_{ij},\hat{\mathbf{e}}_i,\hat{\mathbf{e}}_j))]^2}\right) \\ -\widehat{\mathbf{e}}_j\left(15\epsilon_1\left(\widehat{\mathbf{e}}_i\cdot\widehat{\mathbf{e}}_j\right)\left(1-d^*_{ij}\right)^4-\frac{U^{*2}_{max}(4\times 15\epsilon_1(\widehat{\mathbf{e}}_i\cdot\widehat{\mathbf{e}}_j))}{[4(U^*_{\mathrm{attr}}-\Psi(\hat{\mathbf{r}}_{ij},\hat{\mathbf{e}}_i,\hat{\mathbf{e}}_j))]^2}\right) \end{cases} & , \quad 1\le d^*_{ij}<d^*_{cut} \\ 0 & , \quad d^*_{ij}\ge d^*_{cut}. \end{cases} \tag{3.21}$$

The total gorque acting on the particle i due the particle j can now be solved as $\mathbf{g}_{ij} = \mathbf{g}^{d_{ij}}_{ij} + \mathbf{g}^{r_{ij}}_{ij}$ using the definitions (3.17) and (3.21).

The dynamics of the system is now described by equations (3.16), (3.20), (3.17) and (3.21). It should be noted that in practical use in computer simulations the force labelled $\mathbf{f}^{d_{ij}}_{ij}$ arising from the interactions between line segments (3.16) should be evaluated first or separately from (3.20). This is due to the fact that (3.16) gives rise to gorques through (3.17), but equation (3.20) works directly on centres of mass and therefore does not contribute to the torque.

Further, a comment on the energy at zero separation is appropriate, as it is equal to $U^*_{\max}$ only for the special case when the well depth $\epsilon^* = 0$, then the potential would reduce to a traditional DPD potential, otherwise, as clear from the top line of equation (3.1) the energy at full overlap is $U^*_{\max} + \epsilon^*$. It follows from the definition of the well depth equation (3.4) that magnitude of the repulsive interaction, $U^*_{\max}$ for $d^* < 1$ (top line of equation (3.1)) can be altered without effecting the well depth, for example $U^*_{\max} \rightarrow U^*_{\max} - \epsilon^*$, giving now $U^*(d^* = 0) = U^*_{\max}$. This would obviously affect the forces and gorque, but the calculation of new quantities should be straight forward within the framework given here.

3.4 Molecular dynamics simulations of the new soft-core spherocylinder model

3.4.1 Model A

A series of molecular dynamics (MD) runs were carried out on a bulk system of spherocylinders modelled with the new anisotropic potential given by equation (3.1). The chosen parametrisation was $U^*_{max} = 70.0$, $U^*_{attr} = 1500.0$, $\epsilon_1 = 120.0$ and $\epsilon_2 = -120.0$. This parametrisation strongly favours the side-by-side configuration with the next favourable configuration being the cross configuration. End to end and T-configurations are energetically equal and least favourable. The potential with chosen parametrisation and elongation $L/D = 3.0$ is presented in figures 3.1 and 3.2 as a function of the centre of mass distance, $r^* = r/\sigma$, and distance between line segments, $d^* = d/\sigma$, respectively, in four different configurations.

The simulations were carried out for a bulk system consisting of $N = 1000$ spherocylinders with length to breadth ratio $L/D = 3.0$ and therefore of an effective length of $k^* = 3.0 + 1.0$. Simulations were carried out in the isobaric-isothermal, const-NPT, ensemble as cooling runs starting from an isotropic melt, for an isobar, $P^* = 2.0$. Results are presented in reduced units, where lengths and energies are scaled as $\sigma = D = 1$ and $\epsilon = 1$: providing reduced density, temperature and

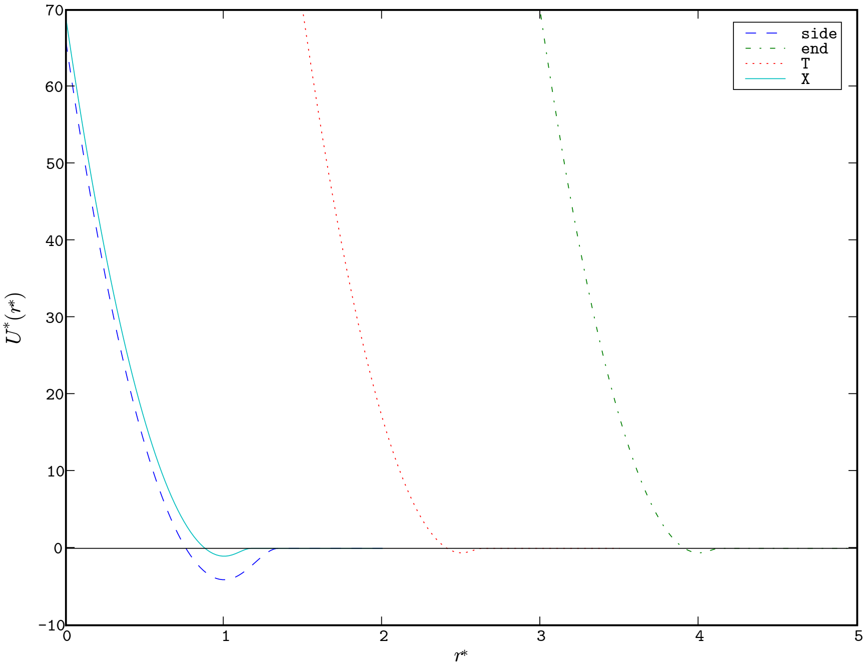

Figure 3.1: Anisotropic spherocylinder potential for elongation $L/D = 3$ with parametrisation $U^*_{max} = 70.0$, $U^*_{attr} = 1500.0$, $\epsilon_1 = 120.0$ and $\epsilon_2 = -120.0$ in four different configurations; side-by-side (dashed line), cross configuration (solid line), T-configuration (dotted line) and end-to-end (dot-dashed line)

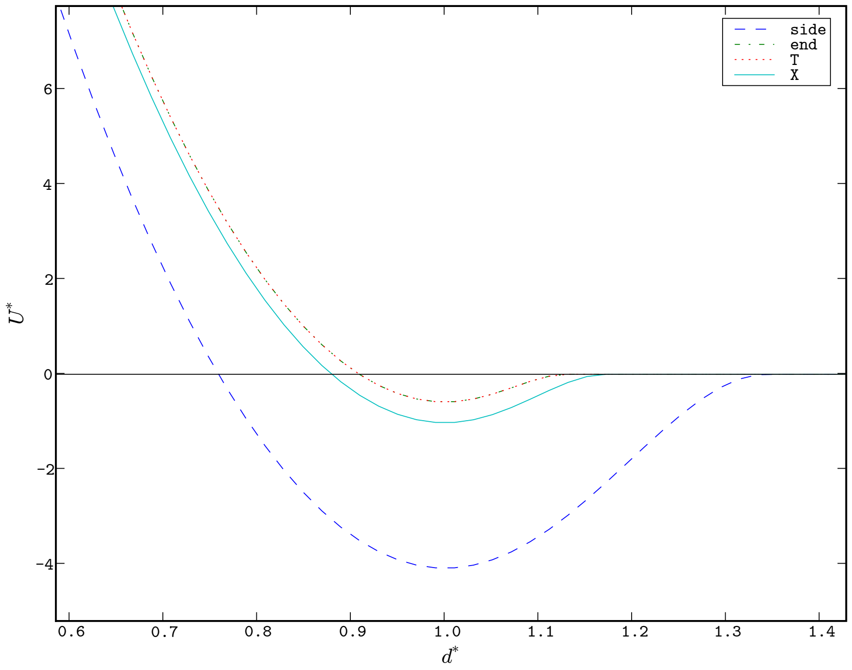

Figure 3.2: Anisotropic spherocylinder potential as a function of line segment distance d^* with parametrisation $U^*_{max} = 70.0$, $U^*_{attr} = 1500.0$, $\epsilon_1 = 120.0$ and $\epsilon_2 = -120.0$ in four different configurations; side-by-side (dashed line), cross configuration (solid line), T-configuration (dotted line) and end-to-end (dot-dashed line).

pressures as [141], $\rho^* = \rho\sigma^3$, $T^* = k_BT/\epsilon$ and $P^* = P\sigma^3/k_BT$, respectively. The temperature was kept constant, thermostatting the translational and rotational velocities with the Andersen thermostat every 100 MD steps. The volume of the simulation box was varied every 20 MD steps by a Monte Carlo box move as described in 2.2.1. Simulation runs were organised as a cooling series for both pressures such that the end configuration of a previous temperature was used as the starting configuration for a new temperature. The system was equilibrated for 200 000 MD steps in each temperature followed by 50 000 MD steps of production run for calculating desired equilibrium quantities. All state points were simulated with a time step $\Delta t(\epsilon/\sigma^2 m)^{1/2} = \Delta t^* = 0.01$ which is an order of magnitude larger than typically used in GB simulations. The equations of motion were integrated using the velocity Verlet algorithm for non-spherical sites [142]. The total energy was found to be well conserved, with fluctuations and drift under 0.2 %, over the course of 1000 MD steps in const-NVE ensemble. The moment of inertia of a spherocylinder, I, was approximated as a moment of inertia of a cylinder $I = \frac{1}{12}m(3r^2 + h^2)$, of mass m, radius r and height h. Here the values of $r = D/2$, $h = L$ and $m = 3$, were used.

3.4.1.1 Simulation results

The temperature dependence of the reduced number density, $\rho^* \equiv N/V^*$, and the orientational order parameter, $\langle S_2 \rangle$, for the cooling series is shown in figure 3.3. The figure shows a discontinuity between the temperatures $T^* = 1.7 \ldots 1.6$. This corresponds to a phase change between a higher temperature isotropic and lower temperature ordered phase, given a change of the orientation order parameter from $S_2(T^* = 1.7) \approx 0.070 \pm 0.004$ to $S_2(T^* = 1.6) \approx 0.9189 \pm 0.0006$. The identity of the low temperature phase was considered by evaluation of the pair correlation functions (introduced in section 2.3.2 of chapter 2) $g(r^*)$, $g_{||}(r^*)$ and the in-layer pair correlation function $g_l(r^*_\perp)$ (figure 3.4). The lower temperature phase shows smectic behaviour, with oscillations in $g_{||}(r^*)$ demonstrating layer structure with a layer spacing just under the molecular length of $4D$. The rapid decay in $g_l(r^*_\perp)$ for order perpendicular to the director within a layer, demonstrates liquid-like order within the layer. Together with a lack of layer tilt, the phase can be identified as a

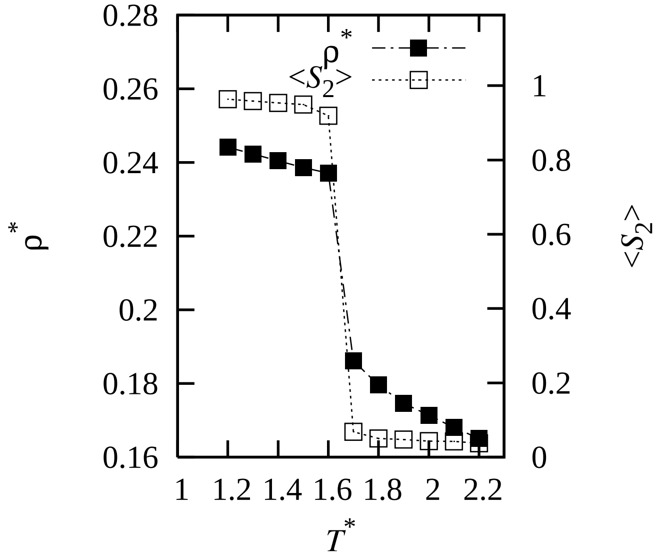

Figure 3.3: Particle number density $\rho^* \equiv N/V^*$ (filled symbols) and orientational order parameter $\langle S_2 \rangle$ as a function of temperature, T^*, for a cooling series with pressure $P^* = 2.0$. The statistical uncertainties are at the order of 10^{-3}.

smectic-A.

3.4.2 Model B

A second considerable softer model was considered with parametrisation; $U^*_{max} = 25.0$, $U^*_{attr} = 150.0$, $\epsilon_1 = 12.0$ and $\epsilon_2 = 0.0$. This parametrisation gives equal well depth for the T and cross configurations as well as side-by-side and end-to-end configurations, with the latter being more attractive. This should de-stabilise the T and cross configurations and enhance particles, on average, aligning along common director. For a similar type of anisotropy, Gay-Berne particles have been observed to exhibit fairly large nematic region [143]. The spherocylinders have an aspect ratio $L/D = 3$ *i.e.* considerably shorter than the minimum, $L/D = 3.7$ needed for a HRS potential to form a nematic phase (see section 2.1.2). The simulation details are the same as with model A (section 3.4.1).

3.4.2.1 Simulation results

In figure 3.5 the particle number density, ρ^*, and orientational order parameter, S_2, are presented as a function of temperature, T^*, for cooling along the isobar $P^* = 2.0$.

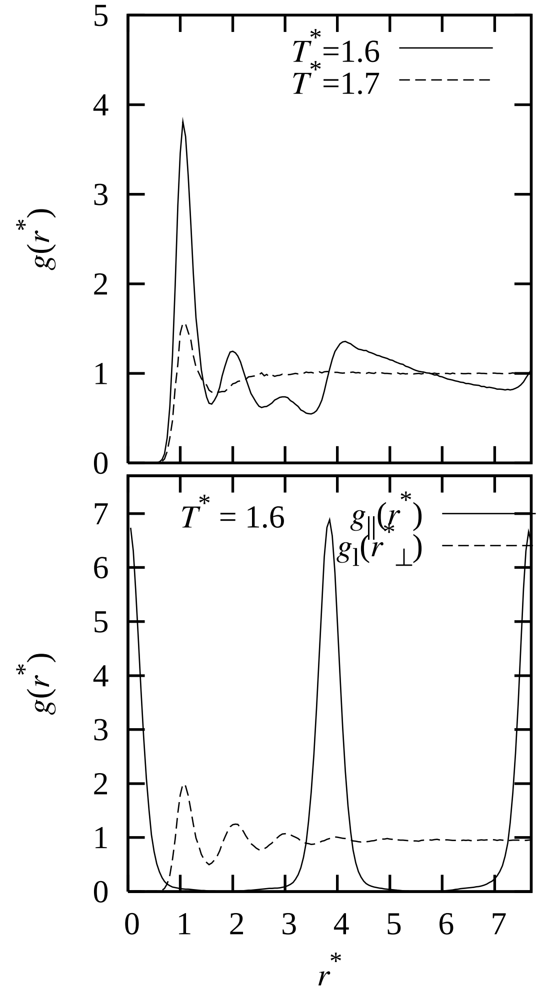

Figure 3.4: Pair correlation function $g(r^*)$ for isotropic, $T^* = 1.7$, and ordered phase, $T^* = 1.6$, (top) and pair correlation functions $g_{||}(r^*)$, $g_l(r^*_\perp)$ for ordered phase, $T^* = 1.6$, (bottom), for model A at the pressure $P^* = 2.0$.

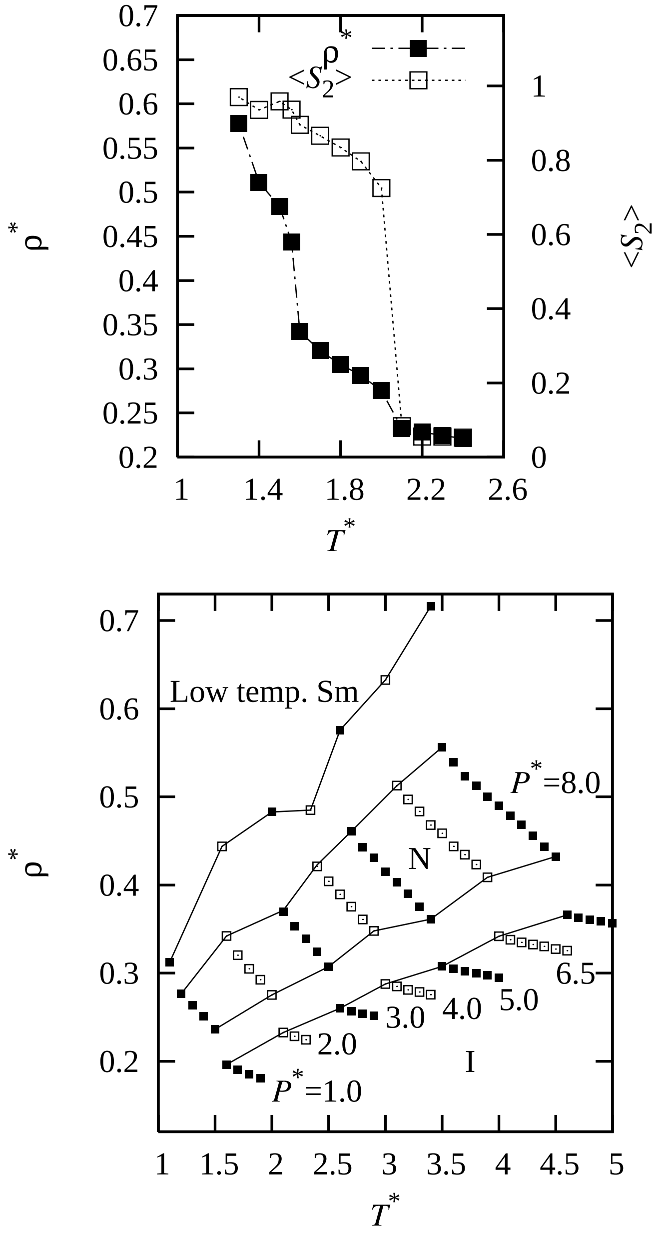

Figure 3.5: Top: particle number density, $\rho^* = N/V^*$ (filled symbols), and orientational order parameter, $\langle S_2 \rangle$ (open symbols), as a function of temperature, T^*, for model B along the isobar $P^* = 2.0$. Bottom: particle number density for model B as a function of temperature for a series of isobars. In the presence of hysteresis and the absence of good quality free energy calculations, the lines joining points to mark the boundaries between smectic-nematic and nematic-isotropic phases are meant as approximate guides only.

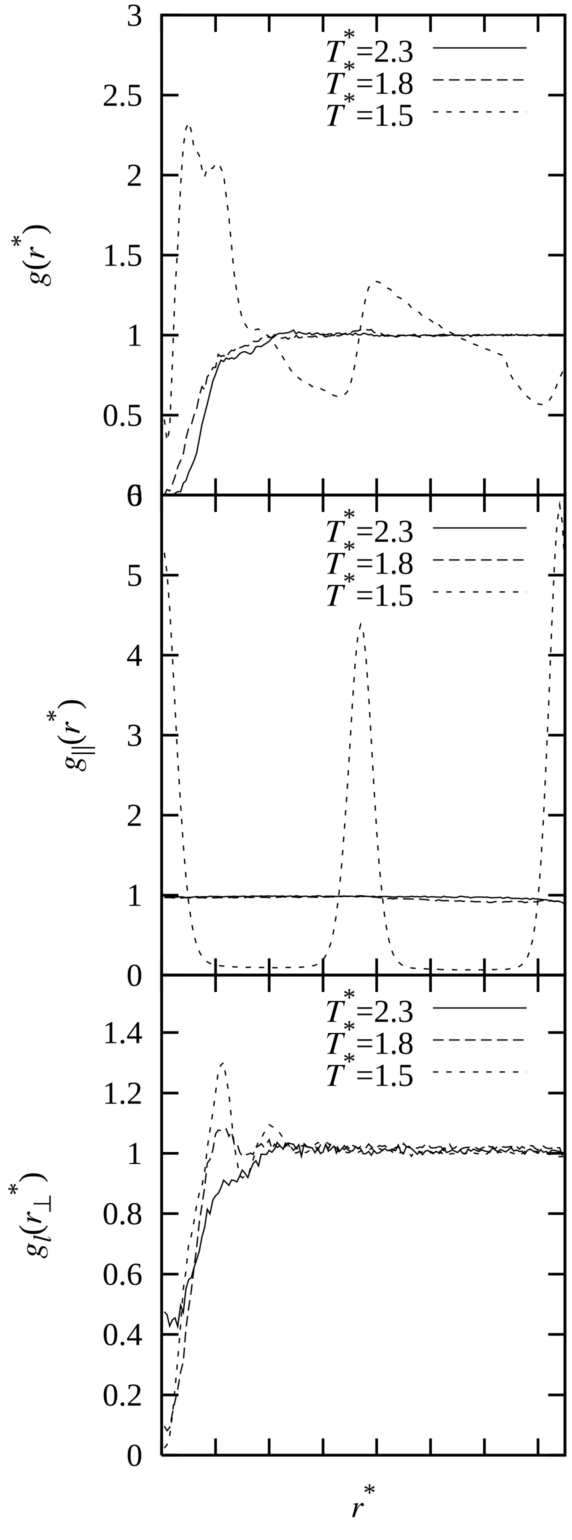

Figure 3.6: Pair correlation functions $g(r^*)$ (top), $g_{\|}(r^*)$ (middle) and $g_l(r_{\perp}^*)$ (bottom) for isotropic ($T^* = 2.3$), nematic ($T^* = 1.8$) and smectic/crystal ($T^* = 1.5$) phases along the isobar $P^* = 2.0$.

There can be observed two discontinuities at $T^* = 2.1 \ldots 2.0$ and $T^* = 1.6 \ldots 1.5$ corresponding to isotropic-nematic and nematic-smectic/crystal phase changes. The isotropic-nematic phase transition is also apparent from the plot of orientational order parameter, S_2, as a function of temperature, T^*. The order parameter jumps from $S_2 \approx 0.084 \pm 0.003$ at $T^* = 2.1$ to $S_2 \approx 0.725 \pm 0.004$ at $T^* = 2.0$ and continues to increase fairly linearly inside the nematic region, $T^* = 2.0 \ldots 1.6$ to a value of $S_2 \approx 0.896 \pm 0.001$ at $T^* = 1.6$.

The structure of the phases can be studied further with the aid of the pair correlation functions, $g(r^*)$, $g_{\|}(r^*)$ and $g_l(r^*_{\perp})$ presented in figure 3.6 for the three phases observed. The three dimensional pair correlation function, $g(r^*)$ (top panel in figure 3.6) shows typical soft fluid behaviour for isotropic fluid ($T^* = 2.3$) and nematic phase ($T^* = 1.8$) with monotonic growth until a separation of $r^* \approx 2.0$ and then settling into straight line along unity, suggesting that there is no three dimensional long range translational order. For the phase with highest order ($T^* = 1.5$) the correlation function shows a considerable amount of structure with nearest neighbour peaks at $r^* \approx 0.6$ and $r^* \approx 1.5$. There is also a strong overlap at very closed distances and also a nonzero value for zero separation, $g(r^* = 0) \neq 0$, implying that the potential is too soft for the state point. The pair correlation function parallel to the director of the phase, $g_{\|}(r^*)$ (middle fig. 3.6), shows no order in either the isotropic nor nematic phases, but in the low temperature phase an oscillation can be observed with peaks at separations $r* \approx 0.0$, $r^* \approx 3.7$ and $r^* \approx 7.3$ implying a layered structure with the layer spacing approximately 3.65 which is just under one molecular length (4.0σ). The intra-layer pair correlation function perpendicular to the phase director, $g_l(r^*_{\perp})$, can be used to establish correlations perpendicular to the director. The liquid like order of $g_l(r^*_{\perp})$ (bottom graph in figure 3.6), implies the formation of a smectic A phase.

3.4.3 Discussion

The phase behaviour of both models A and B are consistent with that expected from previous studies of the Gay-Berne potential, which have been observe to exhibit nematic and smectic phase regions depending on chosen parametrisation [9,143,144].

Moreover, changing the parametrisation from model A to model B, leads to changes in phase stability. To provide a comparison with the GB potential and the recent Gay-Berne-Kihara (GBK) potential [67,145], calculations were performed for a series of isobars across the phase diagram for the model B. These are presented in the bottom panel of figure 3.5, where a widening of the nematic region as the pressure increases can be observed.

For model B, with a similar well-depth for side-to-side and end-to-end configurations, the most comparable Gay-Berne diagram is provided by the work of de Miguel et al. [146] where the authors look at a 3:1 Gay-Berne with a similar ratio of well depths. As with model B, this Gay-Berne potential exhibits an extensive nematic range, which gives nematic-vapour coexistence at low pressures.

As expected from previous studies for anisotropic soft core potentials [60], the equilibration times are fairly rapid and in comparison to GB and GBK models, benefit from a long-time step. However it must be stressed that the soft-core nature of the potentials considered here means that they are not as useful as either the GB or GBK models for studying high density state points, simply because of particle overlaps at very high density.

This new model should, however, provide very useful computationally efficient reference models for liquid crystal phases that can be used for large system sizes, or as a solvent in combination with more complex models. In the next section, the model of equation (3.1) is used as part of a multi-site model for a multi-pedal liquid crystalline molecule. The simulation results presented in section 3.5, demonstrate, that despite the caveats of soft core models as discussed above, they can provide meaningful results and considerably bridge the time and length scales associated in self-assembly and growth of complex phases.

3.5 A simulation study of coarse grained dendritic supermolecule

3.5.1 Introduction

Supermolecules with dendritic scaffolds exhibiting liquid crystal behaviour or supramolecular assembly to nanostructures, are intriguing systems. Liquid crystal dendrimers (LCDrs) have qualities which leads to formation of anisotropic liquid crystal phases despite the seemingly isotropic shape of the supermolecule. The core of a LCDr is a dendritic scaffold with spherical symmetry as shown schematically in figure 1.5. There are many possible architectures for LCDr design depending on the generation of the dendrimer and how the mesogenic groups are attached [147]. It is possible to attach mesogenic groups to the dendrimer core in such a way that the supermolecule itself becomes anisotropic in shape. This sort of thermotropic LDRs have been seen to exhibit nematic, smectic and crystalline phases [148]. In another type, mesogenic groups are attached in such a way that the equilibrium structure forms an isotropic conformation. An experimental study of a fifth generation carbosilane dendrimer where mesogenic groups, terminally attached with flexible spacers to the dendritic scaffold, showed the formation of liquid crystal phases by the supermolecule, which originally was in isotropic shape [149]. For this type of system, changes in the conformation of the supermolecule will allow the mesogenic groups to organise into liquid crystal phases. Further, another experimental study of a first generation dendrimer with an octasilsesquioxane core with eight mesogenic units terminally attached, showed a formation of smectic A (SmA) and smectic C (SmC) phases [24].

Recent simulations of a hybrid model for a third generation carbosilane dendrimer in a liquid crystal solvent indeed showed for the first time, how the supermolecule is able to change shape in response to different solvent phases [150]. In this study the heavy atoms within the dendrimer scaffold were represented by united atom Lennard-Jones sites and terminally attached mesogenic groups were modelled by the Gay-Berne potential. The solvent was modelled with the same Gay-Berne particles as the mesogenic groups, with a parametrisation suitable for the formation of nematic and smectic-A phases. Results showed the dendrimer adopting a rod-like shape in the nematic phase with mesogenic units arranged along the director of the phase. Moreover, in a SmA phase, it was observed that the dendrimer tried to lie commensurate with the smectic layering of the solvent by placing mesogenic groups in five different smectic layers [150]. A follow up simulation study, using a more coarse grained model for the same carbosilane dendrimer, showed a spontaneous microphase separation with individuals dendrimers preferring a rodlike conformation in smectic phase [36].

In this section a new, computationally efficient model for a first generation LCDr (also called a multipedal LC molecule) is presented, using the new orientationally-dependent spherocylinder model for the mesogenic groups developed in section 3.2. The model is introduced in section 3.5.2 and the simulation results, showing a spontaneous self-assembly into an ordered structure with strong coupling between the order of the phase and the structure of the individual molecule, will be reported in section 3.5.3.

3.5.2 Coarse grained model and computational details

The coarse grained dendritic supermolecule was constructed with spherical and non-spherical (soft core spherocylinder) sites bonded together. The total potential energy can be expressed with the force field

$$U = \sum_{\text{pairs}} U_{\text{pair}} + \sum_{\text{bonds}} U_{\text{bond}} + \sum_{\text{angles}} U_{\text{angle}}. \tag{3.22}$$

Here, there are three different types of intermolecular interactions: sphere-sphere (sp-sp), sphere-spherocylinder (sp-sc) and spherocylinder-spherocylinder (sc-sc). For the sp-sp and sp-sc interactions a purely repulsive quadratic (equation 2.13) form is used for the pair potential, U_{pair}, with $U^*_{\text{max}} = 70.0$. For modelling the mesogenic groups, an interaction potential between two spherocylinders with the orientational-dependent potential (equation 3.1) with parameters $U^*_{\text{max}} = 70.0$, $U^*_{\text{attr}} = 1500.0$, $\epsilon_1 = 120.0$ and $\epsilon_2 = -120.0$ was employed. This is the same as model A, described in

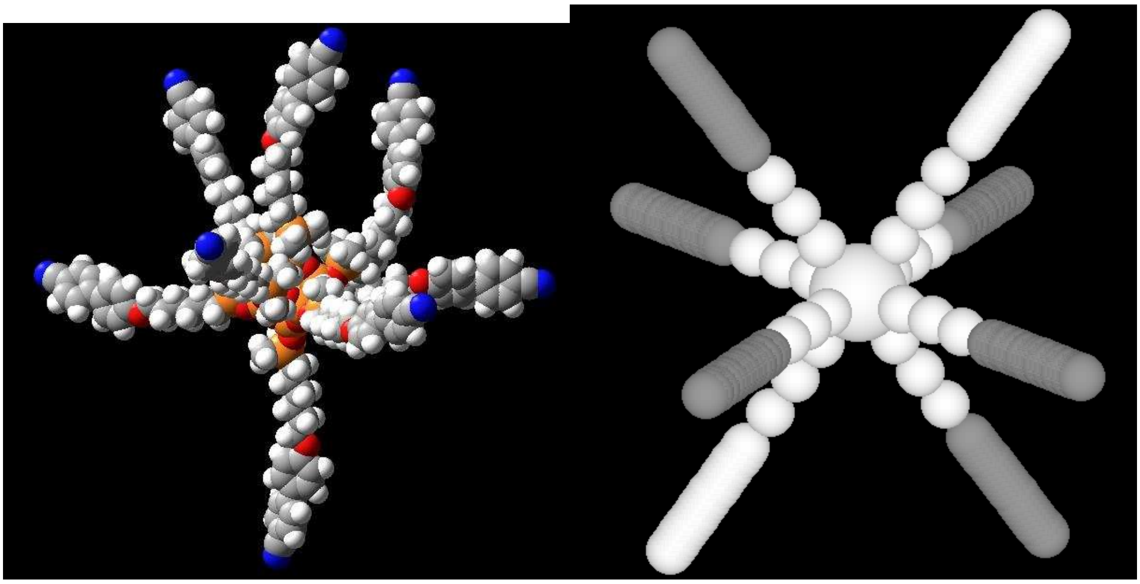

Figure 3.7: Structure of the multipedal liquid crystalline supermolecule studied in section 3.5. Left: a space-filling representation of the molecular structure of an octasilsesquioxane octamer from reference [2]. Right: the structure of the coarse-grained octamer studied in this work.

section 3.4.1. Adjacent sites, $i,\ j$, were bonded together with harmonic bonds

$$U_{\text{bond}}(r_{ij}) = \frac{1}{2}k_{\text{bond}}(r_{ij} - l_0)^2, \tag{3.23}$$

where k_{bond} is the force constant for the bond, r_{ij}, is the distance between centres of mass and l_0 is the equilibrium bond length. For angles, a similar type of harmonic potential was used

$$U_{\text{angle}}(\theta_{ijk}) = \frac{1}{2}k_{\text{angle}}(\theta_{ijk} - \theta_0)^2, \tag{3.24}$$

where k_{angle} is the corresponding force constant, θ_{ijk} is the angle corresponding to the centre of mass positions of three adjacent particles, $i,\ j,\ k$ and θ_0 is the equilibrium angle.

The model consisted of a spherical core (sp_1) and eight arms each having the same topology; a chain of three spheres (sp_2) connecting a spherocylinder (SCS) to the spherical core. These arms were uniformly distributed on the shell of the spherical core. An example of the equilibrium structure of the molecule can be seen in figure 3.7. To model the excluded volume effect of the dendritic scaffold, the size of the core sphere was taken to be twice as large as the chain spheres connecting

Table 3.1: The bonded parameters used to model the multipedal liquid crystal supermolecule.

Quantity	Value
k_{bond}	$50/\epsilon\,\sigma^{-2}$
$l_0(\text{sp}_1\text{-sp}_2)$	$1.5/\sigma$
$l_0(\text{sp}_2\text{-sp}_2)$	$1.0/\sigma$
$l_0(\text{sp}_2\text{-SCS})^a$	$1.0/\sigma$
k_{angle}	$5/\epsilon\,\text{rad}^{-2}$
$\theta_{ijk}(\text{sp}_2\text{-sp}_1\text{-sp}_2)$	180°, 70.5° or $109.5^{\circ b}$
$\theta_{ijk}(\text{sp}_1\text{-sp}_2\text{-sp}_2)$	180°
$\theta_{ijk}(\text{sp}_2\text{-sp}_2\text{-sp}_2)$	180°
$\theta_{ijk}(\text{sp}_2\text{-sp}_2\text{-SCS})$	$180^{\circ c}$

---

[a] The soft core spherocylinder is bonded via the end of the spherocylinder line segment.

[b] Three forms of angle are used depending on the connectivity of the chains about the central core.

[c] An additional angle term is also used to confine the angle between spherocylinder long axis and the spherocylinder bond to approximately 180°. This avoids free rotation of the spherocylinder

the mesogen, $\sigma_{\text{sp}_1} = 2\sigma_{\text{sp}_2} = \sigma$. The elongation for the spherocylinders was chosen to be $L/D = 3.0$, with $D = \sigma$. The elongation is similar to $L/D = 2.84$ found from coarse graining a third generation carbosilane dendrimer [36]. The bond length between the core sphere and the neighbouring sphere was set to $l_{\text{core-sp}} = 1.5\sigma$. The neighbouring sphere was bonded to the end of the spherocylinder line segment giving a bond length between spherocylinder and sphere, and between sphere and sphere, equal to $l_{\text{sp-sc}} = l_{\text{sp-sp}} = \sigma$, with force constant $k_{\text{bond}} = 50.0/\epsilon\sigma^{-2}$.

In order to ensure a uniform distribution of the arms on the shell of the core all the spheres adjacent to the core sphere were bonded with angle terms through the centre sphere, *i.e.* for the angle θ_{ijk} the j particle was the core particle and i, k were spheres adjacent to the core sphere. The equilibrium angles were defined in such a way that all connection combinations through the central core were taken care of, ensuring a uniform distribution. In the arms, the angle terms were taken to start from the core sphere and going all the way to the spherocylinder with equilibrium angle $\theta_0 = 180.0^o$, resulting to a equilibrium structure of straight arms. The angle terms were desired to be weaker than the bonds so force constant of $k_{\text{angle}} = 5.0/\epsilon\text{rad}^{-2}$ was applied. The bonded parameters are summarised in table 3.1.

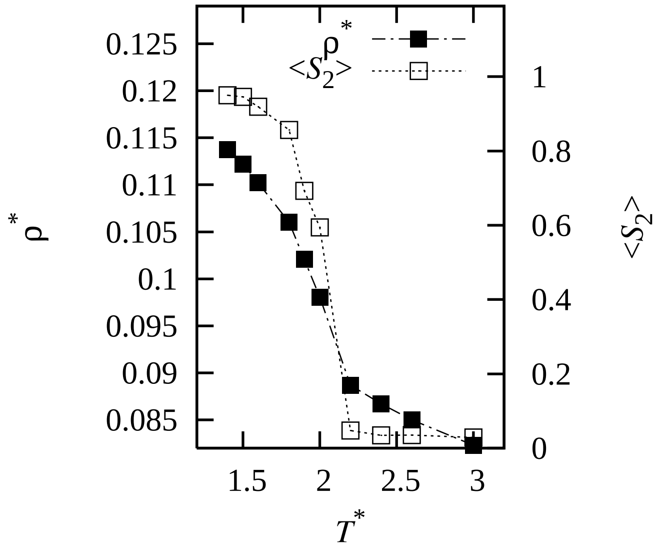

Figure 3.8: The particle number density , $\rho^* = N_{\mathrm{sc}}/V^*$, (closed symbols) and orientational order parameter, $\langle S_2 \rangle$, (open symbols) for spherocylinders along the isobar $P^* = 2.0$. Results from a cooling run, started initially from an isotropic phase.

The simulations were run for a bulk system consisting of $N = 125$ molecules, resulting in $N_{\mathrm{sphere}} = 125 + 125 \times 8 \times 3 = 3125$ spherical sites and $N_{\mathrm{sc}} = 125 \times 8 = 1000$ spherocylinders giving a total number of 4125 interaction sites. Simulations were run as a cooling series along the isobar $P^* = 2.0$ in the const-NPT ensemble. Equations of motion were integrated using the velocity Verlet algorithm, with a time step of $\Delta t^* = 0.01$. Initially, the conservation of total energy was checked with short simulation in the const-NVE ensemble. The system was equilibrated for $1-2$ million MD steps depending on the state point. To ensure constant temperature, the system was allowed to collide with an Andersen heat bath every 100 MD steps, constant pressure was achieved using attempted MC volume moves, using the Metropolis method introduced in section 2.2.2, every 20 MD steps. Translational and rotational temperatures as well as pressure (calculated through the pair virial) were monitored through the course of the simulation, ensuring that system had equilibrated properly.

3.5.3 Simulation results

In figure 3.8, particle number density, $\rho^* = N_{sc}/V^*$, and orientational order parameter, S_2, are presented for a cooling series for temperatures between $T^* = 3.0 \ldots 1.4$

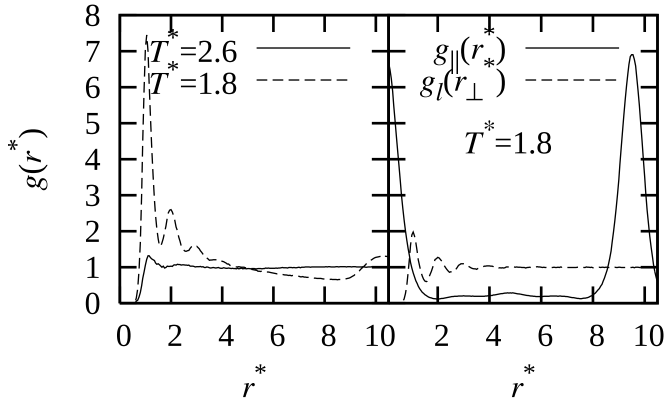

Figure 3.9: Pair correlation functions $g(r^*)$ for temperature $T^* = 2.6$, $T^* = 1.8$ (left) and $g_{||}(r^*)$ and $g_l(r^*_\perp)$ (right) for temperature $T^* = 1.8$.

along the isobar $P^* = 2.0$. From these results, there can be observed a discontinuity between $\rho^* = 0.089$ to $\rho^* = 0.10$ and $S_2 = 0.05$ to $S_2 = 0.59$, with errors of magnitude 10^{-5} and 10^{-3} respectively, between temperatures $T^* = 2.2$ and $T^* = 2.0$, corresponding to a phase change between a higher temperature isotropic phase and a lower temperature ordered phase.

To study the phase structure further, as previously in section 3.4, three different pair correlation functions, measuring three dimensional order, $g(r^*)$, order along the director of the phase, $g_{||}(r^*)$ and order perpendicular to the director $g_l(r^*_\perp)$ were calculated. These are presented in figure 3.9. The growth of an ordered mesophase can be observed with the growth of the nearest neighbour peak at $r^* \approx 1.0$ between temperatures $T^* = 2.6$ and $T^* = 1.8$ and the formation of a second nearest peak at $r^* \approx 2.0$ at lower temperature. Further, a growth of peaks in $g_{||}(r^*)$ can be observed. This corresponds to smectic layering with layer spacing (distance between peaks) of $d^* \approx 9.5$. Together with the liquid like order in $g_l(r^*_\perp)$, these suggests the formation of a smectic A phase.

The internal structure of the liquid crystal dendrimer was studied by calculating a radial distribution function for the different parts of the molecule with respect to the molecule core, $\rho(r^*)$. From $\rho(r^*)$ graphs (figure 3.10) it can be seen that the radially averaged structure of the individual chain does not change dramatically between phases, this is in agreement with observations in [36]. The third peak in $\rho(r^*)$ for spheres becomes more visible at lower temperatures compared to the higher

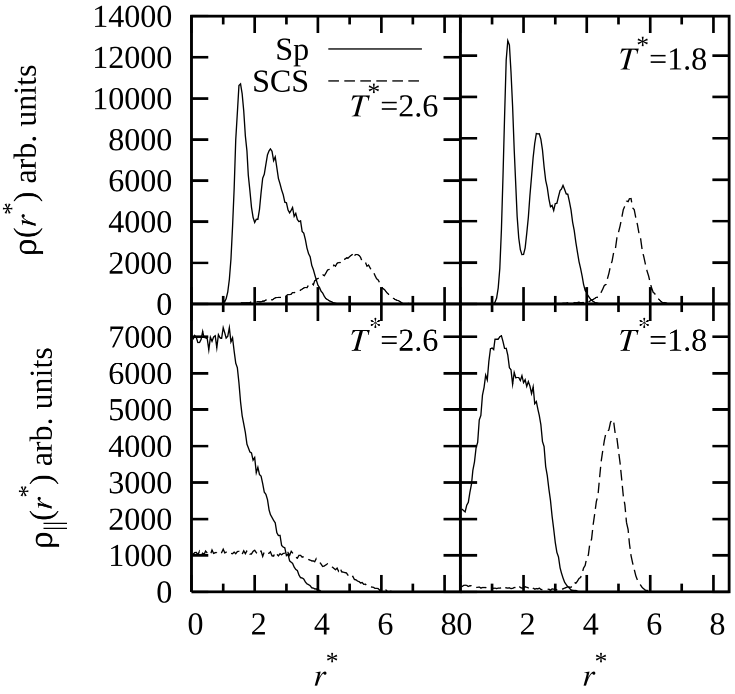

Figure 3.10: The radial distribution functions, $\rho(r^*)$ and $\rho_{\parallel}(r^*)$, for separate parts of the dendrimer, relative to the core sphere: isotropic phase (top) and ordered phase (bottom).

temperature isotropic phase. The biggest difference between the radially averaged structure, can be seen in sharpening of the spherocylinder peak with maximum approximately at $r^* = 5.5$, in the ordered phase. Both of these observations imply, given the consideration that the equilibrium distance from the middle of spherocylinder to the middle of the core sphere for a fully flexed arm is 6σ, that the arms are more flexed in the ordered smectic-phase. This can be observed in more detail from the radial distribution function calculated parallel to the system director $\rho_{\parallel}(r^*)$, shown in bottom panel of figure 3.10. Figure 3.11 shows two snapshots of bulk phases taken from the simulations. From these, the change of structure from the isotropic to the layered smectic-like phase can clearly be observed. From the snapshots of the single molecule, a clear change in structure can be observed. The simulations therefore demonstrate that there exists strong coupling between the structure of the molecule and the structure of the phase itself, with the molecule undergoing a transition to a rod-shaped structure at transition to the smectic phase.

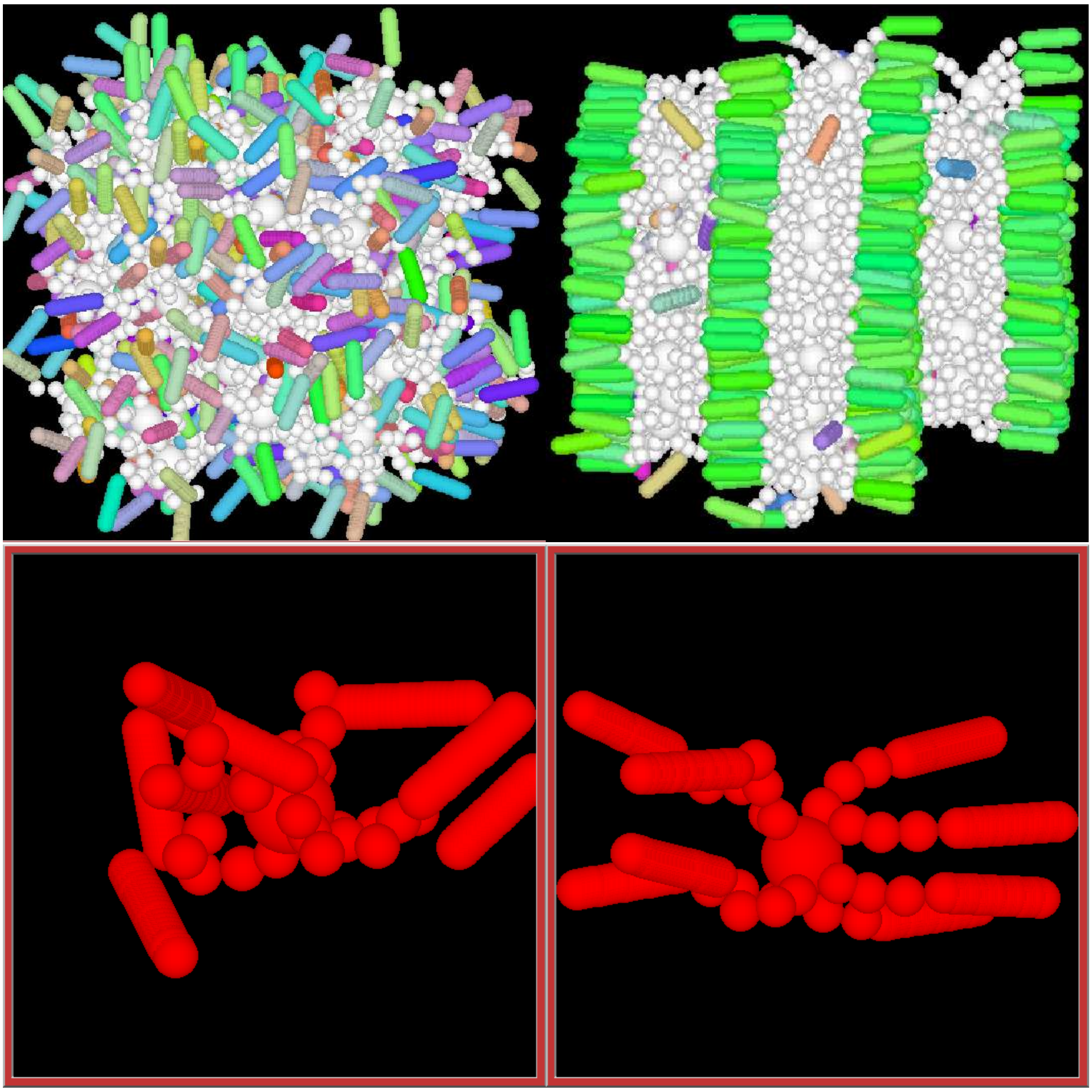

Figure 3.11: (Top) Snapshots of bulk phases from two different state points: isotropic phase, $T^* = 2.6$ (left) and smectic phase, $T^* = 1.8$ (right). (Bottom) Snapshots of a single molecule taken from each state point.

3.6 Conclusions

A new orientational-dependent model for ultra soft spherocylinders has been presented. Explicit expressions for the potential, forces and gorques are given, which should enable reasonably easy implementation of the potential into existing molecular dynamics programs.

The very soft nature of the potential allowed a long time step, $\Delta t = 0.01$, to be used in molecular dynamics simulations, which is an order of magnitude larger than typically employed in GB models. The potential has four parameters controlling the repulsive and attractive interactions, U^*_{max} , U^*_{attr}, and ϵ_1, ϵ_2 controlling the anisotropy. This flexibility allows a wide cascade of different system to be modelled. Moreover, the soft nature of the potential in combination with the long time step means it is much quicker to simulate model liquid crystal systems with this potential, than with conventional single site coarse grained models, such as the Gay-Berne or the SRS potentials. This means that the model provides an ideal "reference model" for use with other potentials (for example as a generic liquid crystal solvent for atomistic models) or for use with very large system sizes (for example to look at liquid crystal-surface interactions or defects in a liquid). The potential can also be used as part of a multi-site coarse grained supermolecule, allowing longer time steps and therefore increasing the length and time scales such that phenomena such as spontaneous self assembly can take place, as demonstrated in section 3.5. It is also useful to note that in the simulation of the $N = 125$ multipedal LC molecules, self-assembly took place for simulation runs between 1 to 2 million MD steps. The computational cost of 1 million MD steps with a single processor, was approximately 30 hours.

In chapter 4 this new anisotropic soft-core potential will be used to study the phase behaviour of a model main chain liquid crystalline polymer by mapping out a phase diagram as a function of the rod length and to study chiral induction. In chapter 6 the model will be combined with a relatively new simulation methodology, Statistical Temperature Molecular Dynamics, to study isotropic-nematic and isotropic-lamellar phase transitions in const-NVE and const-NVT ensembles.

Chapter 4

Applications of the anisotropic soft-core potential

Chapter 3 introduced a new soft-core model for the simulation of mesogenic systems. Key features of the new model were its speed of equilibration compared to conventional models for mesogens and the relative ease of using it in multisite models to study complex mesogenic systems. This chapter investigates the use of this new model for two systems where it would have been difficult to use conventional LC models because of equilibration and sampling difficulties.

Section 4.1 presents results for the phase diagram of a model main chain liquid crystalline polymer, as a function of length of the mesogenic unit. This included equilibration of approximately 100 different phase points, so relatively quick equilibration times were essential.[1] In the second case, presented in section 4.2, chiral induction was studied by solvating flexible achiral solute molecules within chiral solvents. For this system, very good sampling of different conformations was an essential requirement for reliable results.

---

[1] These results have been published as: A coarse-grained simulation study of mesophase formation in a series of rod-coil multiblock copolymers. J. S. Lintuvuori and M. R. Wilson, Phys. Chem. Chem. Phys. **11**, 2116 (2009).

4.1 Main chain liquid crystal polymer simulations

4.1.1 Introduction

The phase behaviour of simple block copolymers (BCPs) has been extensively studied experimentally [151], theoretically [152] and by means of computer simulation for flexible models [117] and for rod-coil models [121, 153]. In the simplest case of flexible diblocks composed of two different components A and B, one expects the well-known classical morphologies: lamellar (L) with alternating layers of A and B components, cylindrical (C) where the minority component forms cylinders packed on a hexagonal lattice, and spherical (S) where the minority blocks form spheres arranged on a bcc lattice. Also, formed is the more complex bicontinuous gyroid structure (G) where the minority component forms the tubes (connectors) and nodes of a three-fold coordinated lattice. The formation of the G phase in diblock copolymer systems has been extensively studied by means of computer simulations by Martinez-Veracoechea and Escobedo [118, 119, 154, 155].

BCPs provide a means of changing long-range order in a continuous way simply by varying the degree of polymerisation. The ability to use molecular interactions to tune self-assembly and hence control morphology in this way is particularly attractive from the point of view of potential applications [151].

Mesophase formation in simple block copolymers arises due to microphase separation of incompatible A and B components. However, small modifications of the basic structural blocks, by (for example) the introduction of rigidity [156] provides a second competing physical effect, i.e. in this case the presence of anisotropic interactions. In fact, in practice, many polymers (both natural and synthetic) can have rod-like components. These can arise due to extended π-conjugation or aromatic groups along the backbone, or alternatively can arise from common secondary structure (for example alpha helices or beta sheets), which also impart rigidity. In general, rod-coil systems are found in three main categories of polymers covering organic electronics of synthetic polymers [157–160], biological molecules (e.g. proteins and also synthetic-peptides [161, 162]). In all these systems, interplay between microphase separation of unlike blocks and the liquid crystalline order expected for rod-like units can potentially lead to rich phase behaviour. Such effects provide for the possibility of more exotic phase morphologies. For example, studies of rod-coil diblocks have reported the formation of honeycombs, arrowheads, zigzag lamellae, wavy lamellae, hollow spherical micelles, cylindrical micelles, smectic-C phases as well as more conventional phases [121, 156, 163–167].

A more complicated example of a rod-coil system is provided by typical multiblock copolymers, where the single rod-coil building block is repeated many times. Such materials are sometimes used in thermoplastic elastomers, blend compatibilizers and barrier materials [156]. Many main chain liquid crystalline polymers (MCLCPs) also fall into this category. Multiblock systems with flexible and rigid constituent parts are normally extremely difficult to study by simulation methods because of the problems of equilibrating structures in which there is often considerable coupling between the tertiary structure of the chain and the microphase separated structure of the mesophase.

4.1.2 Polymer model

The new anisotropic soft-core spherocylinder model, equation (3.1), has been used to study mesophase formation of multiblock copolymer systems. The coarse grained rod-coil multiblock copolymer is schematically represented in figure (4.1). The model polymer chain is composed of four repeat units, each of which consists of a flexible polymer chain and a rigid mesogenic rod. The combination of spherical and anisotropic sites (as shown in figure 4.1) mimics the structure of a typical rod-coil multiblock copolymer, which would typically exhibit preferential interactions between similar types of interaction centre within the main chain. This model allows (by altering the spherocylinder elongation L/D) the study of mesophase formation, as a function of rod volume fraction.

In all systems studied, a semi-flexible chain of five beads of diameter $\sigma_0 = D = 1$ was used. However, the length to breadth ratio of the spherocylindrical mesogenic unit was varied over a wide range of values, characterised by the spherocylinder L/D ratio (figure 4.1). In this work values of L/D between 0.1 and 11.0, corresponding to a total length to breadth ratio of between 1.1 and 12.0 for the rigid part of the

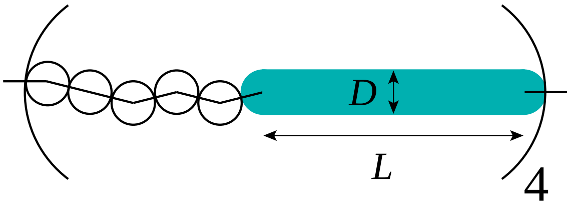

Figure 4.1: A schematic representation showing the molecular structure of the model liquid crystal block copolymer studied in this work. Values of L/D range between 0.1 and 11.

polymer, were used.

Non-bonded interactions were modelled as a sum of site-site pairwise interactions. The spherocylinder-spherocylinder interaction is based on a typical quadratic form (as used in dissipative particle dynamics (DPD) simulations) for the repulsive part with a fourth order angle dependent term to model attractive interactions as described by equation (3.1). As in chapter 3, reduced units are used, such that $U^* \equiv U/\epsilon$ and $d^* \equiv d/\sigma_0$, with $\epsilon = \sigma_0 = 1$.

For the spherocylinder-spherocylinder pair interaction a parameterisation of $U^*_{\text{max}} = 100.0$, $U^*_{\text{attr}} = 1200.0$, $\epsilon_1 = 60.0$ and $\epsilon_2 = -60.0$, was used. This results in maximum well depths of $\epsilon^* \approx 4.15$, $\epsilon^* \approx 2.37$, $\epsilon^* \approx 1.65$ and $\epsilon^* \approx 1.65$ for the side-by-side, cross, T and end-to-end configurations respectively (figure 4.2). The sphere-sphere interaction was parametrised with $U^*_{\text{max}} = 100.0$ and $U^*_{\text{attr}} = 2000.0$ resulting in a maximum well depth of $\epsilon^* \equiv U^{*2}/4U^*_{\text{attr}} \approx 1.25$. For the sphere-spherocylinder interaction a purely repulsive form of the potential, equation (3.1), was used with maximum energy at zero separation $U^*_{\text{max}} = 100.0$.

Simple harmonic potentials of the form described by equation (3.23) were used to link interaction sites together into a main polymer chain. Here, r_{ij} and r_0 are the distance between consecutive sites i and j in the chain and the equilibrium bond length respectively, with $k_{\text{bond}}/(\epsilon\sigma_0^{-2}) = 50.0$ as the bond force constant. The spherocylinders were bonded from the midpoint of the hemisphere capping the cylinder, therefore all the bonds had an equilibrium bond length of $r_0 = \sigma_0$. No angle or torsional terms were used for chain beads. However, all beads in a chain interacted through the same non bonded potential, meaning that excluded volume for chain beads was fully taken into account. Hence the chains are semi-flexible,

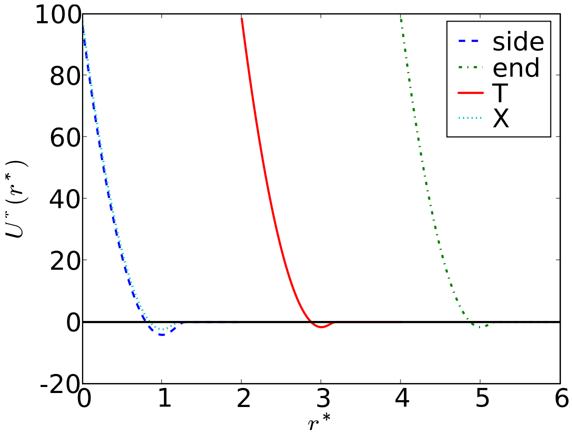

Figure 4.2: The anisotropic soft core spherocylinder potential used for this work. Here, the interaction potential is plotted as a function of separation of particle centres, r^*, for four different arrangements of two molecules: side-to-side, end-to-end, T-shape (side-to-end) and crossed.

rather than ideal.

4.1.3 Computational details

Phase behaviour was studied for a melt consisting of $N_m = 125$ polymer chains at an occupied volume fraction $\phi \equiv \frac{N_{\text{tot}}\pi\sigma_0^3}{6V_{\text{box}}} \approx 0.384$, where N_{tot} is the total number of spheres (with a spherocylinder approximated as $L/D + 1$ spheres). A rectangular simulation box, $L = L_x = L_y = L_z$ was used with volume $V = L^3$. The simulations were done as cooling runs in the canonical (const-NVT) ensemble starting from isotropic configurations. For each temperature simulated the system was initially equilibrated for $2.0 \times 10^6 - 5.0 \times 10^6$ MD steps depending on the state point simulated with a MD time step of $\Delta t^* = 0.01$. The equations of motion were integrated using a velocity Verlet integrator using the GBMOL molecular dynamics program [142, 168] and the temperature was kept constant by applying an Andersen thermostat every 100 MD steps. A Lowe-Andersen thermostat was also used for some runs, equation (2.25), to provide a stochastic element to the dynamics, though in practice both methodologies yielded similar results in similar time. Assessment of equilibration was carried out by measuring the change in a series of energetic and structural quantities, as indicated below. For well-equilibrated systems, configurations were written to disk every 1000 MD steps for further analysis and averaged quantities were computed over the final 50 000 MD steps. Also, a few additional calculations were carried out for systems, which were 8× larger than above (i.e. 1000 molecules). As for the smaller system, these larger simulations used a cubic box, and runs were started by cooling from an isotropic polymer melt.

4.1.4 Results

The self-assembly behaviour of a model MCLCP was studied in a constant occupied volume fraction of 0.384. The temperature and elongation, L/D, of the rod sections, were varied. In the results presented below, elongations of L/D =0.1, 1.0, 2.0, 3.0, 4.0, 5.0, 6.0, 7.0, 9.0 and 11.0, were considered. This covers a range of rod lengths either side of $L/D = 4.0$, which would correspond to a similar volume fraction of rods and spheres. In each case the simulations were carried out as a sequence of cooling runs starting from an isotropic melt, thus allowing the self-assembly to happen spontaneously.

Initially, mesophase formation was observed by visualising snapshots from different state points using the QMGA [3] molecular graphics package. The orientational order within the polymer system was characterised by means of the nematic order parameter for the rods, S_2, which was obtained by diagonalising the orientational order tensor $Q_{\alpha\beta}$, equation (2.28). To obtain structural information, the radial distribution function, $g(r)$, for the rods in each system along with its components parallel, $g_{||}(r)$, and perpendicular $g_{\iota}(r_{\perp})$ to the director (introduced in section 2.3.2) were calculated. In addition to the pair correlation functions, the structure factor, $S(k)$, was calculated, as a secondary means of identifying layers (or other structure) in the system. For a lamellar system the highest value of $S(k)$ occurs at a wave vector $\mathbf{k}_{\mathrm{max}}$, corresponding to a direction normal to the layering. As noted by Hughes et al. [36], from the direction of $\mathbf{k}_{\mathrm{max}}$, it is possible to define a layer normal vector, $\mathbf{p}$; and to calculate the mean tilt angle, $\langle\psi\rangle=\langle\mathbf{p}\cdot\mathbf{n}\rangle$, for the system. This allows a crude measure of tilt in the system and thus helped to identify if a tilted smectic C phase was formed.

Examples of typical radial distribution functions for rods are shown in figure 4.3 for the $L/D = 2$ system. $g(r^*)$ is plotted for reduced temperatures, $T^* = kT/\epsilon$, cor-

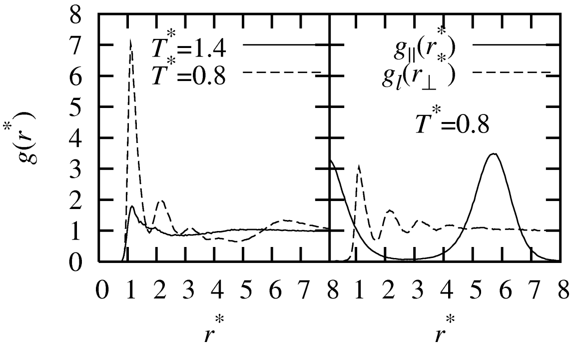

Figure 4.3: Radial distribution functions, $g(r^*)$, $g_{||}(r^*)$ and $g_l(r_\perp^*)$ for the $L/D = 2$ polymer at selected temperatures $T^* = 0.8$ and $T^* = 1.4$.

responding to the lamellar and isotropic phases ($T^* = 0.8$) and ($T^* = 1.4$), together with plots $g_{||}(r^*)$ and $g_l(r_\perp^*)$ for the lamellar system. The order-disorder transition (ODT) is characterised by a significant growth in the first peak of the spherocylinder radial distribution function. The layer structure of the lamellar is seen in the strong peaks in $g_{||}(r^*)$, which signify the distance of separation of the centres of the spherocylinder layers. In the case of the $L/D = 2$ system a layer spacing of $\delta_{\text{layer}} \approx 5.6\sigma_0$ relates to the approximate length of the spherocylinders ($3\sigma_0$) with a further $2.6\sigma_0$ representing the sublayer of coils separating each spherocylinder layer (see below). In contrast $g_{||}(r^*)$ provides a simple straight line ($g_{||}(r^*) = 1$, curves not shown) for a nematic phase or for an isotropic melt [169]. The form taken by $g_l(r_\perp^*)$ for the lamellar layer is very similar to that of a normal radial distribution of a dense liquid. An initial peak at the contact distance is followed by two further peaks of weakening intensity corresponding to second and third neighbours in the plane. Thereafter, $g_l(r_\perp^*)$ decays to a value of 1, indicating liquid-like order within each lamellar layer.

Using the information obtained from S_2, $g(r^*)$, $g_{||}(r^*)$, $g_l(r_\perp^*)$ and $S(k)$, a approximate phase diagram for the polymer was identified. This is presented in figure (4.4) as inverse temperature, $1/T^*$, vs the rod elongation, L/D, where the temperature, $T^* = kT/\epsilon$, is expressed in reduced units.

The phase diagram is dominated by the presence of lamellar phase for temperatures below the order disorder transition (ODT). Snapshots of the phases formed are presented in figure 4.5. For quite large rod volume fractions a small area of

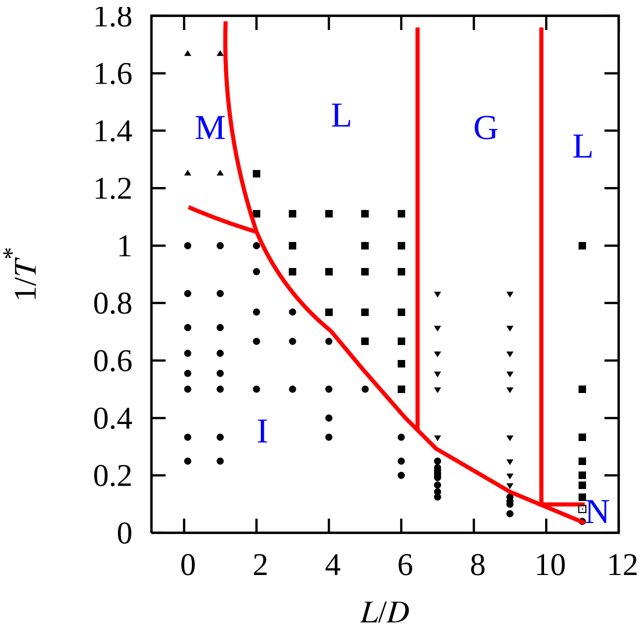

Figure 4.4: The phase diagram for the multiblock copolymer generated from the molecular dynamics simulations of $N = 125$ molecules at an occupied volume fraction $\phi \approx 0.384$. The following phases were observed: isotropic (closed circles), nematic (open squares), lamellar (closed squares), gyroid (closed downward triangles) and micellar phase (closed upward triangles). Lines marking phase boundaries are meant as a guide to the eye only and do not represent exact boundaries.

nematic stability was observed. For short rods evidence exists for the formation of elongated micelles. In the middle of the phase diagram, with rod aspect ratios L/D = 6 and 7, a gyroid phase was stabilised. As a general trend the ODT moves to higher temperatures as the rod elongation is increased. This is, as expected, due to increased mesophase stability caused by the rods when L/D is increased.

From previous theoretical studies of rod-coil diblocks [122,170] and triblocks [171] it comes as no surprise that there exists a large range of lamellar stability. The preferential A-A and B-B, interactions favour phase separation. The alignment of rods is favoured through energetic and entropic reasons. The rod-rod pair interaction, figure 4.2, favours the side-by-side configuration over the end-to-end configuration. These factors lead to the predominate ODT being from isotropic to lamellar.

For rod-coil-rod (and other multi block copolymers) at temperatures below the ODT there exists two possible coil configurations; bridging and looping [165]. To estimate the relative proportions of bridging and looping coils, a distribution function

$$f_{ij} = \langle \cos \theta_{ij} \rangle = \langle \mathbf{u}_i \boldsymbol{.} \mathbf{u}_j \rangle \, , \tag{4.1}$$

for the orientations $\mathbf{u}_i$ and $\mathbf{u}_j$ for the rods i and j within the same polymer chain was calculated. For a fully elongated chain, all rods are taken as pointing in the same direction. Figure 4.6 plots the functions f_{12}, f_{23}, f_{34}, f_{13}, f_{14}, for a typical state point corresponding to the $L/D = 5$ polymer in the lamellar phase. To minimise system size effects here, results are given for a system of 1000 molecules (corresponding to 5 full layers of spherocylinders). The functions all show two peaks corresponding to anti-parallel $f_{ij} \approx -1$ and parallel $f_{ij} \approx 1$ alignment of rods. The linear connectivity of the polymer guarantees that anti-parallel alignment between adjacent sites is a signature of the rods lying in the same lamellar layer, the flexible coil forms a loop between the two rods in same lamellar layer. Parallel alignment of adjacent rods means that the linking coil forms a bridge between two lamellar layers. The graphs of f_{12}, f_{23}, f_{34}, all show the same result, a slight preference for looping chains over bridges. Integrating the areas under the curves for $\cos(\theta) \in [-1, 0]$, and $\cos(\theta) \in [0, 1]$ an estimate of looping and bridging chains can be obtained. The statistics are only slightly in favour of the former: respectively 64%, 59% and 62% (with error bars of $\approx$ 2-3%) for 1-2, 2-3 and 3-4 spherocylinders. For the correlation functions, f_{13} and f_{14}, for rods separated by two and three coils, a slight growth of the $+1$ peak can be observed (top left in figure 4.6). For rods separated by two coils, f_{13}, the $\cos(\theta) = 1$ means that all the rods are in same lamellar layer or that all the rods are in different layers i.e. no bridging chains or two bridging chains. $\cos(\theta) = -1$ means that there exists one bridging chain. Similar behaviour was also obtained for system of $N = 125$ shorter rods with $L/D = 2$, although the preference for looping was reduced slightly by $\approx$ 1-3%.

In the bottom diagram of figure 4.6 the correlation function for the head and tail rods, f_{14}, is shown for a system of $N = 125$ polymers with long rods of $L/D = 11$. As expected, for the isotropic phase at temperature $T^* = 20.0$ there exists virtually no correlation between the head and tail rods due to the flexibility of the coil sections. However, in the nematic phase at temperature, $T^* = 12.0$, alignment of the rods along a common director, leads to a growth of two peaks in f_{14} corresponding to parallel and anti-parallel alignment, while the orientational order parameter remains relatively high $S_2 \approx 0.66$. This suggests the presence of hairpin conformations. The presence of such "defects" has also been noted in two previous simulation studies of MCLCPs [172, 173]. It must be noted that a system size of $N = 125$ for polymers with large rod elongations, such as $L/D = 11$, is too small to fit more than two fully grown lamellar layers into the simulation box (top part in figure 4.5), therefore rigorous statistical analysis was not carried out for the system with $L/D = 11$.

In the simulated lamellar systems, the orientational order parameter, S_2, was typically around 0.7-0.8. The order parameter was generally slightly higher for the longer rods, with the lowest calculated order parameter for the lamellar phase ($S_2 \approx 0.69$) was seen for the $L/D = 2$ system. Although the order parameters are relatively high, they still indicate that there exists a noticeable distribution of rod orientations.

Self-consistent field theory (SCFT) studies of rod-coil diblock copolymers have suggested formation of bilayers in a lamellar (smectic-A) phases [12] and formation of a tilted smectic-C phase when coil volume fraction is increased [12, 174]. The latter would be due to rods relieving the stress in the layers by tilting. Neither bilayer formation nor strong evidence for smectic-C formation was observed in the current study. The maximum tilt averaged over molecules was less than 5 degrees in all cases. It might be useful to note that in this model case coil chains are very flexible and rods are happy to adopt order parameters as low as $S_2 = 0.69$ (near the ODT) for the $L/D = 2$ case. Consequently the amount of strain caused by the lamellar structures is not overly high.

Chen and coworkers [163, 164] have demonstrated the formation of wavy lamellar-chevron-like structures in systems of polyhexyl isocyanate-polystyrene diblock copolymers. Recent SCFT work also suggests that chevron-like structures may be metastable with respect to a possible defect free smectic-C structure [174]. In quenching from the isotropic melt into the lamellar region, the simulations demonstrated some initial evidence for tilting of rods occurring in layers in different directions, creating chevron-like structures. However, this behaviour was only transient in the simulations, and tilted domains disappeared in favour of smectic-A layering

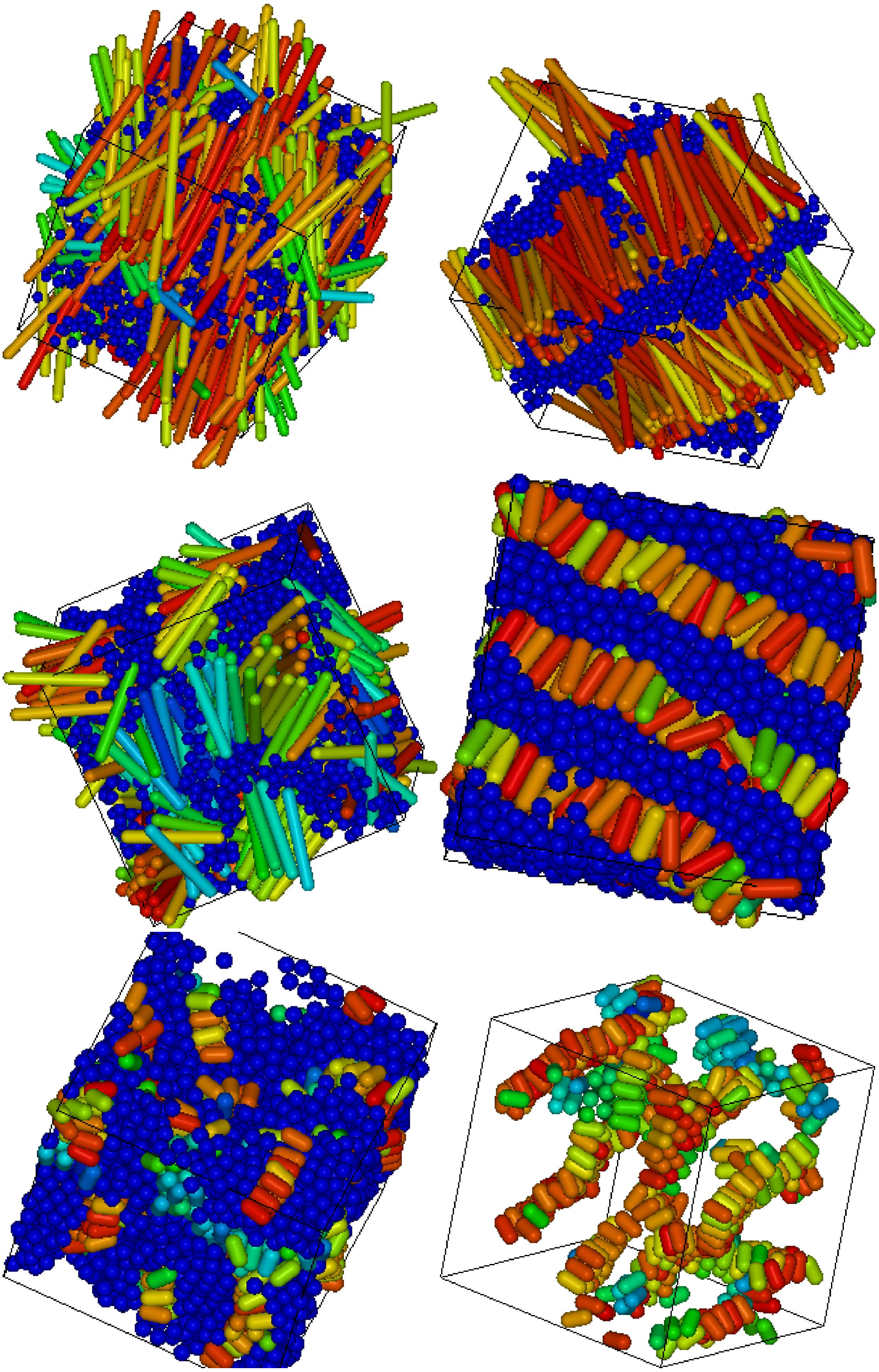

Figure 4.5: Snapshots from bulk simulations of $N = 125$ main chain liquid crystal polymers. Nematic phase from the system with elongation $L/D = 11$ at temperature $T^* = 12.0$ (top left), lamellar phase for $L/D = 11$ at $T^* = 4.0$ (top right), gyroid phase for $L/D = 7$ at $T^* = 3.0$ (middle left), lamellar phase for $L/D = 2$ at $T^* = 0.8$ (middle right), micellar phase for $L/D = 1$ at $T^* = 0.6$ with spheres (bottom left) and spheres removed (bottom right). The snapshots were produced with the QMGA [3] molecular graphics program.

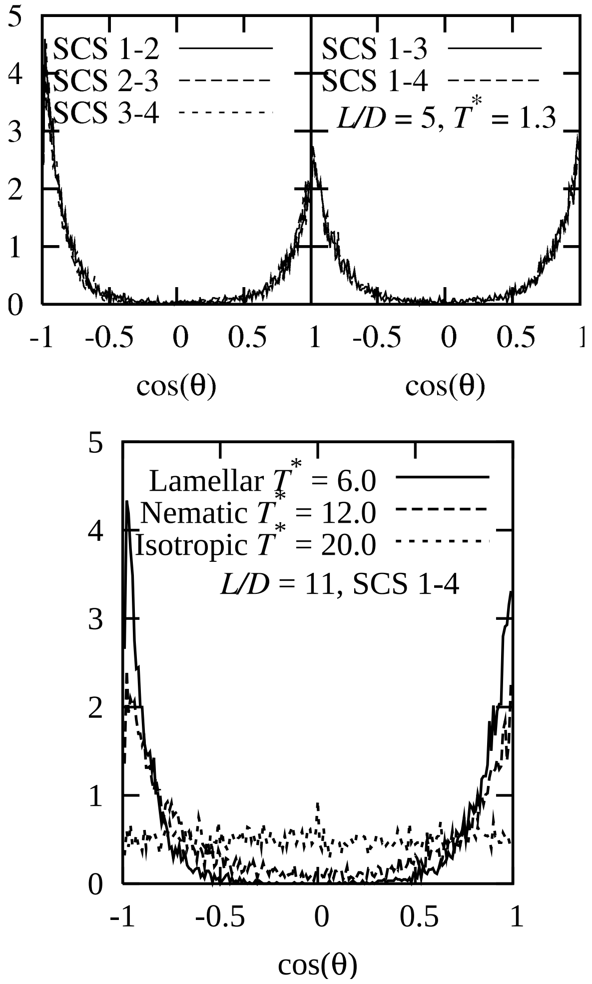

Figure 4.6: Plots of the angular distribution function $f_{ij} = \langle \cos\theta_{ij} \rangle$ in the lamellar phase for the $L/D = 5$ polymer at $T^* = 1.3$ (top graphs) and for the $L/D = 11$ polymer in three phases (bottom graphs). The top graphs show distribution functions for the three cases where spherocylinders are separated by one chain f_{12}, f_{23}, f_{34}, and by two and three chains f_{13}, f_{24}.

over long annealing runs.

In the model used in this work, as in the extended SCFT work of Pryamitsyn and Ganesan [174], when rods are aligned the anisotropic attractive interaction means that there is a strong tendency for rod-rod attraction. This greatly reduces the range of stability for a nematic region. However, increasing the length of the rods eventually leads to a situation in which excluded volume effects stabilise the nematic phase. A nematic thus occurs when the competition between translational and rotational entropy is won by the former, at comparatively high temperatures, in the situation where there is very weak segregation. In the case considered here, at an occupied volume fraction of 0.384, an isotropic-nematic phase transition starts to occur at $L/D = 11$. At the opposite side of the phase diagram, when the coil volume fraction is high and curvature effects are too great for the formation of lamellae, we see evidence for micellar ordering below the ODT. Here, as expected, we do not get spherical micelles (figure 4.5) but instead the relatively strong side-to-side interactions of the rods lead to elongated micelles.

In the middle of the phase diagram, for $L/D = 7$ and $L/D = 9$ systems, cooling below the ODT leads to microphase separation into structures which appear to represent a bicontinuous gyroid phase. To look in more detail at the phase segregated structures we mapped the distribution of spheres and spherocylinders as surfaces. This was carried out by first dividing the simulation box into a $10 \times 10 \times 10$ grid and calculating the local number density for each small cube. This was then plotted as an isosurface in figure 4.7. The isosurfaces show the presence of three tubes intersecting at each node, which would correspond to a gyroid bicontinuous structure (G), as opposed to a double diamond (DD) with four tubes intersecting at a node, or the plumber's nightmare phase (P) with six tubes intersecting at a node. To check on the stability of this phase, simulations were carried out for the $L/D = 7$ system with 1000 molecules. As with the smaller system the gyroid phase formed spontaneously on cooling from the isotropic melt and remained stable over simulations in excess of 1×10^6 MD steps. However, it must be noted, that this is still a relatively small system and for the "off-lattice" simulations, the model is relatively expensive, compared to an "on-lattice" model or compared to studies of diblocks.

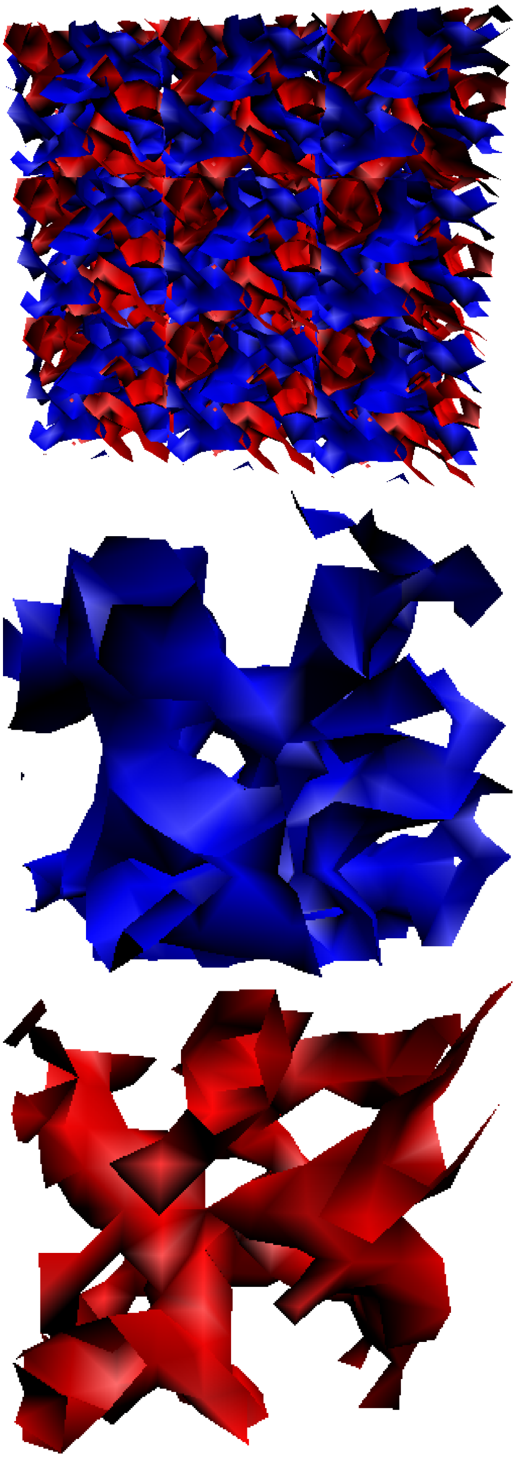

Figure 4.7: Isosurface plots for the density of spherocylinders (red) and spheres (blue) within the gyroid phase for a $L/D = 9$ system. [Top] 9 periodic boxes shown. [Middle] sphere surface from one period box. [Bottom] spherocylinder surface from one periodic box.

In a series of dissipative particle dynamics, Monte Carlo and free energy calculations of off-lattice diblock copolymer melts, Martinez-Veracoechea and Escobedo [118] have shown that the formation of a gyroid phase is remarkably sensitive to simulation conditions. It can be artificially induced by inappropriate size of the simulation box, thus the interactions with periodic images over the box sides could stabilise the phase [118]. To prove the phase stability, free energy calculations with possible competing phases, such as lamellar, should be carried out and free energies compared. Recent work shows that such calculations are indeed possible for simpler systems [118] but these would be very challenging for the multiple block copolymer molecules used in this work.

In a recent, theoretical study of coil-rod-coil and rod-coil-rod triblock copolymers, Chen *et al.* [171, 175] found that the gyroid phase was stable at a fairly high rod volume fraction of $f = 0.7$. This is in contrast to rod-coil diblocks where no gyroid phase, to my knowledge, has been reported. For the system considered here, despite the presence of multiple rod-coil blocks, the comparative flexibility of the chains means that separation of spheres from rods in a gyroid structure, does not cause excessive strain in the flexible chains leading to "packing frustration" at the connection points i.e. nodes [118, 119]. In theory, stability of this phase is possible for the system, up to the point where the nematic phase becomes the favoured mesophase at the ODT for longer rods.

Finally, few simulations were carried out at smaller occupied volume factions of 0.029 and 0.0072. Here, in some of the simulations a momentum conserving Lowe-Andersen thermostat was employed to provide a stochastic element to the dynamics in addition to calculations with the Andersen thermostat. The former both helps with equilibration of the system and also simulates the effect of solvent collisions. For a coarse-grained model, such as this, small occupancy volume fractions correspond to the polymer in solution with an implicit solvent. A snapshot from one of these simulations appears in figure 4.8, showing the presence of a self-assembled ordered nanowire in which we see lamellar domains with the layer normal running parallel to the direction of the wire. Such structures are seen in several independent simulations at low volume fractions. There has been considerable re-

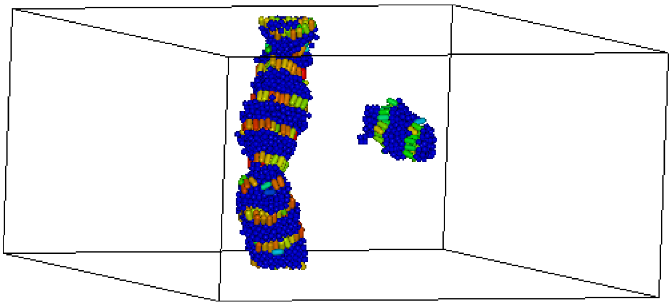

Figure 4.8: A snapshot showing simulation results for a $L/D = 1$ polymer with an occupied volume faction of 0.0072 at a temperature of $T^* = 0.6$.

cent interest in self-assembled block copolymer nanowires. This is particularly the case for conjugated polymer systems, which may offer possibly future applications in photoelectrical devices [176].

4.1.5 Conclusions

The new anisotropic soft core coarse-grained potential model, developed in chapter 3 (equation 3.1), was used successfully to study the phase behaviour of a rod-coil multiblock copolymer in constant occupied volume fraction. The simulations demonstrate the formation of micellar, nematic, lamellar and gyroid phases, which spontaneously form as the simulation is cooled through the ODT from an isotropic polymer melt. Increases in the length of the rod component stabilise mesophases, increasing the order-disorder transition temperature. Increases in rod length also stabilise the formation of a nematic phase. In the lamellar phase both looping and bridging coils occur between layers of rods, with a small preference seen for the former. At very low occupied volume fraction, corresponding to the solution phase for the coarse-grained model, self-assembly of the polymer chains into an ordered nanowire was observed.

4.2 Chiral induction

4.2.1 Introduction

Molecular chirality, resulting in a very small net twist between adjacent molecules, leads to a rich variety of liquid crystalline phases [7]. These include high twisting blue phases with cubic symmetry [177] (lying between isotropic liquid and conventional chiral nematic (cholesteric) phase), smectic blue phases [178] and twist grain boundary phases [179]. The formation of a chiral nematic phase has also been reported in biological systems such as an aqueous solution of DNA [180] and a suspension of rod-like viruses [181, 182] including the fd-viruses [18, 183].

Chiral nematic phases have been studied by the means of computer simulations using standard periodic boundary conditions [184], twisted periodic boundary conditions [185–188] and in the vicinity of a chiral wall [189]. Varga and Jackson studied the temperature dependence of a macroscopic pitch in a chiral nematic phase composed of hard spherocylinders with a chiral dispersion potential by confining the system between two structureless parallel hard walls [190]. Very recent reports include a molecular level simulation study of a twisted nematic cell consisting of approximately 1 million Gay-Berne particles [191] and a generalised van der Waals theory for the twist elastic modulus and the helical pitch of a chiral nematic phase [192].

Chiral nematic and normal uniform nematic can be considered as two branches of the same family with a molecular level difference [7]: racemic systems or systems consisting of only achiral molecules would lead to the formation of a nematic phase while systems with molecules different from their mirror image would lead to the formation of a chiral nematic phase. Generally, if a nematic phase is doped with chiral molecules the phase itself would become chiral. Likewise, when a chiral nematic is doped with achiral dopant molecules the helical twist of the chiral phase is reduced. However, in a recent experiment [193] a chiral nematic phase formed by a cholesterol derivative was doped with three different achiral banana shaped molecules. In each case the helical twist was observed to increase instead of decrease. Earl *et al.* studied one of these bent core molecules atomistically in a gas

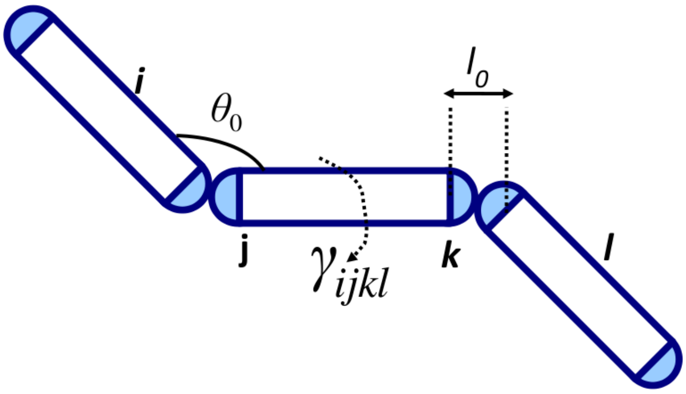

Figure 4.9: Schematic representation of the molecule.

phase [194]. It was found that the molecule is on average achiral, but it possesses conformations with extremely high helical twisting power. It was postulated that in a chiral field these highly twisting conformations would be preferentially selected over their mirror image, leading to an increase of the overall twist.

In the remaining part of this chapter a simple coarse grained model with control of conformational chirality is developed. The simulation results show the connection between conformational chirality of individual molecules and the helical pitch of the bulk phase. Further, the simulations show how an achiral molecule (which normally possesses equal and opposite chiral conformations with high twist) shows chiral selectivity when placed in a chiral environment. Conformations which twist in the same direction as the host phase are preferentially selected leading to an enhancement of the twist of the bulk phase.

4.2.2 Molecule model

The molecule used in this study was composed of three rod like units, represented by soft core spherocylinders joined together. The molecular model is presented schematically in figure 4.9. The spherocylinder elongation was chosen as $L/D = 4$ with $D = \sigma_0 = 1$. Adjacent spherocylinders were bonded together using a simple harmonic potential (equation (3.23) in chapter 3) using a force constant $k_{\text{bond}}/(\epsilon\sigma_0^{-2}) = 50.0$. The equilibrium bond length was set to $r_0 = 0.0\sigma_0$ to form a continuous "tube" molecule with flexible joints. The flexibility of the joints was controlled by introducing a harmonic angle potential; equation (3.24) in chapter 3. Now, the interactions sites i, j and k defining the bond angle θ_{ijk} were chosen from adjacent spherocylinders in following fashion; i was chosen to be the centre of mass of the spherocylinder 1. j was chosen to be that end of the line segment of spherocylinder 1, which was bonded to the spherocylinder 2. k was chosen to be the centre of mass of the spherocylinder 2. The equilibrium bond angle was chosen as $\theta_0 = 45^0$ and the force constant was chosen to $k_{\text{angle}}/(\epsilon\text{rad}^{-2}) = 200.0$. This is a considerably higher force constant than for bonds, and it was chosen to avoid the bond angles reaching (even instantaneously) a linear configuration during the simulations runs, thus this would cause a problem in the calculation of the dihedral angle.

In order to control the conformational chirality of the model molecule a "dihedral" potential was employed for rotation around the middle spherocylinder. The four interaction sites needed to calculate the "dihedral" angle, γ_{ijkl}, were chosen (as presented in figure 4.9) as follows: i the centre of mass of the first spherocylinder, j and k both ends of line segment of the middle spherocylinder and l the centre of mass of the third spherocylinder. During the course of the study two different dihedral potentials were considered

$$U_{\text{dihedral}}(\gamma_{ijkl}) = A\left[1 + \cos\left(n\gamma_{ijkl} - \gamma_0\right)\right] \tag{4.2}$$

and

$$U_{\text{dihedral}}(\gamma_{ijkl}) = -A\left[\cos\left(\frac{1}{2}\gamma_{ijkl} - \gamma_0\right)^n + \cos\left(\frac{1}{2}\gamma_{ijkl} + \gamma_0\right)^n\right] + A. \tag{4.3}$$

The parameter A controls the height of the barrier between the consecutive wells and γ_0 can be used to change the equilibrium dihedral angle. In the potential of equation (4.2) the integer, n, sets the number of wells and in the potential of equation (4.3) it controls the width of each of the two wells.

By employing the dihedral potentials, equations (4.2) and (4.3), a desired equilibrium conformation or conformations can be set. Setting the equilibrium dihedral to, $\gamma_{\text{eq}} = 180^0$, a linear, non chiral, conformation is favoured (left in figure 4.10). Changing the equilibrium dihedral angle away from 180^0, conformational chirality can be induced in the molecule. An example of a chiral conformation is presented

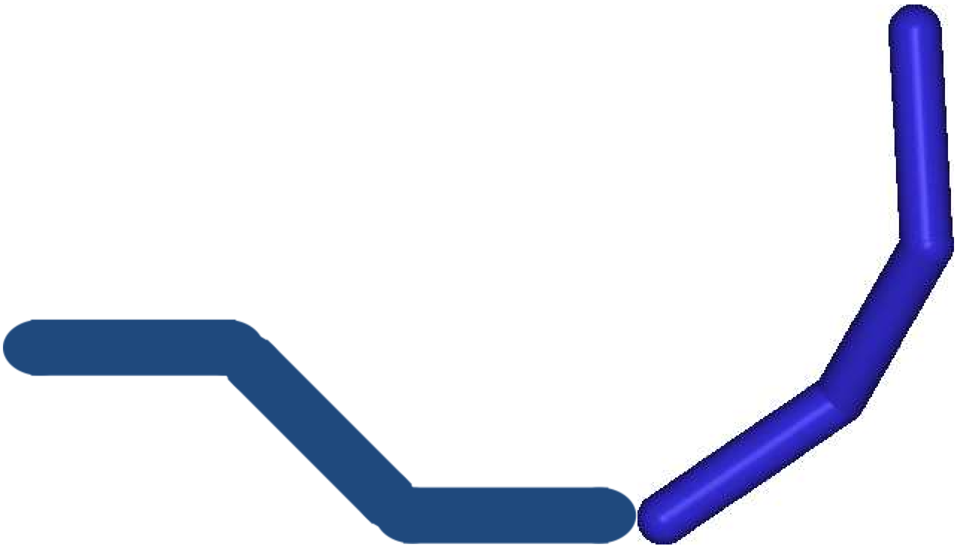

Figure 4.10: Two snapshots of individual molecules used in this study. An achiral planar molecule with $\gamma_{ijkl} = 180^0$ (left). A Chiral, "cork screw', molecule with $\gamma_{ijkl} = 120^0$ (right).

in the right hand panel of figure 4.10. Further, the equal but opposite dihedral angles around the achiral value of 180^0, can be used to distinguish between "left" and "right-handed" conformations with equal twist.

The calculations (energies, forces and torques) of the bonds between the end of a line segment between the two consecutive spherocylinders, bond angles and dihedrals as described above were implemented in the existing parallel MD program GBMOL, by the author of this thesis.

4.2.3 Computational details

To study a chiral nematic phase doped with achiral molecules a simulation system of $N = 4000$ molecules, totalling 12 000 interactions sites, as described in the section 4.2.2, was constructed. The non bonded interactions were described with the new anisotropic soft core spherocylinder model, equation (3.1), introduced in chapter 3. For the spherocylinder pair interaction, a parametrisation of $U^*_{\mathrm{max}} = 100.0$, $U^*_{\mathrm{attr}} = 2000.0$, $\epsilon_1 = 220.0$ and $\epsilon_2 = 0.0$, was used (left panel in figure 4.11). This parametrisation favours side-by-side and end-to-end configurations, destabilising the T and cross configurations. As with the model B single site system (studied in chapter 3, section 3.4.2) this parametrisation favours nematics. However,

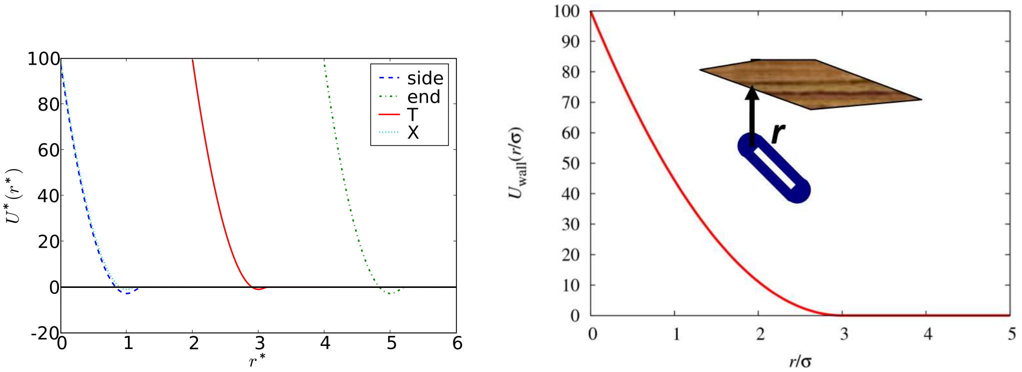

Figure 4.11: The soft-core potentials used in this study. The pair potential between two spherocylinders of elongation $L/D = 4$ (left). The potential between a spherocylinder and a soft wall positioned in the xy-plane (right).

the parametrisation used here is far more repulsive than model B of chapter 3.

The molecules were placed into a slightly elongated rectangular simulation box, $V = L_xL_yL_z$, with box lengths $L_x = L_y \approx 41.35\sigma_0$ and $L_z \approx 58.48\sigma_0$. Throughout the simulations length scales were fixed as $D = \sigma_0 = 1$.

Simulations of a chiral nematic phase using standard periodic boundary conditions (PBCs), in which the molecules (or parts of molecule) interact with periodic images on the opposite side of the box, pose a severe challenge. The dimension of the simulation box along the helical axis (figure 1.2 in chapter 1) should be a multiple of the helical pitch p. Otherwise the top and bottom layers perpendicular to the helical axis are not commensurate and the system is not able to relax, causing an artificial stress and defects [190]. In theory, it would, of course, be possible to define an ensemble where the box dimension along the helical axis could be varied while keeping the total volume constant by reducing/increasing the area perpendicular to the helical axis. For true molecular scales, the helical pitch of a chiral nematic system is in the order of some hundreds of nanometers [193], and millions of molecules would be needed to accommodate the pitch. The effect of PBCs can be removed by confining the system between two structureless walls perpendicular to the helical axis. Providing that the system is large enough that the confinement effect on the nematic ordering is small, a simulation of fraction of the pitch length can be carried out [190].

To achieve this in this work, a soft repulsive wall of quadratic form

$$U^*_{\mathrm{wall}}(r_z) = U^*_{\mathrm{wall}}(1 - r_z/\sigma_{\mathrm{wall-SCS}})^2 \tag{4.4}$$

was placed at both ends of the simulation box in the xy-plane. Similar to equation (3.1) the parameter, U^*_{wall}, sets the maximum energy at full overlap and $\sigma_{\mathrm{wall-SCS}}$ sets the interaction range of the wall (if $r_z \geq \sigma_{\mathrm{wall-SCS}}, U^*_{\mathrm{wall}}(r_z) = 0$). The walls were placed in the xy-plane, perpendicular to the $z - axis$. Therefore the shortest distance, r_z, between the wall and spherocylinder is always the distance between the nearest end of line segment of the corresponding spherocylinder along z-axis and the z-coordinate of the wall (right panel, figure 4.11). The resulting force, $-\nabla U^*_{\mathrm{wall}}(r^*_z)$, has only a z-component, $\mathbf{f}_{\mathrm{wall}} = (0,\ 0, \pm f_{\mathrm{wall}})$. This gives rise to a gorque $\mathbf{g}_{\mathrm{wall}} = (\pm\frac{1}{2}L/D)\mathbf{f}_{\mathrm{wall}}$. Calculation of these was incorporated into GBMOL md program by the thesis author.

Ideally, there would exist no anchoring at the wall. Initially parametrisations of $U^*_{\mathrm{max}} = 1000$ and $U^*_{\mathrm{max}} = 100$ with $\sigma_{\mathrm{wall-SCS}} = \sigma_0$ were tried. These lead to two chiral domains, with opposite twist, growing from each wall at the opposite side of the simulation box, along the z-axis. The domains met in the middle of the simulation box where a defect was formed. This was largely due to strong anchoring at the surface combined with the nature of conformational chirality of the molecules. If the molecules align the same “edge” to the wall on the opposite sides of the simulation box, they induce an equal but opposite twist. One possible solution, could be to let only the middle SCS interact with the wall. However, this led to homeotropic anchoring at the wall. To minimise the anchoring at the wall, a longer interaction range between the wall and SCSs was introduced. As apparent, from the right hand panel of figure 4.11, the parametrisation of $U^*_{\mathrm{wall}} = 100$ and $\sigma_{\mathrm{wall-SCS}} = 3\sigma_0$ allows a penetration of $1\sigma_0$ for an approximate energy penalty of $10k_BT$, thus reducing the anchoring.

The equations of motion were integrated using the velocity verlet algorithm using the GBMOL program [142,168], with timestep $\Delta t^* = 0.01$. The energy conservation was checked for small number of these molecules by simulations in the const-NVE

ensemble. Temperature was kept constant at $T^* = 3.0$ by applying an Andersen thermostat every 100 MD steps. The simulations were carried out for $2 - 3 \times 10^6$ MD steps followed by 50 000 MD steps of production run when configurations were written on disk every 1000 steps for analysis.

4.2.4 Results

4.2.4.1 Pure melts

The effect of the dihedral angle, γ_{ijkl}, for the formation of twisted nematic phase was studied for six pure melt systems using the dihedral potential of function equation (4.2) with parameters $A = 20.0$, $n = 1$ and $\gamma_0 = 0,\ 10^0,\ 30^0,\ 45^0,\ 60^0,\ 70^0$. These resulted in equilibrium dihedral angles of $\gamma_{\text{eq}} = 180^0,\ -170^0,\ -150^0,\ -135^0,\ -120^0,\ -110^0$, where $\gamma_{\text{eq}} = 180^0$ corresponds to an achiral (planar) equilibrium conformation, and the other extreme, $\gamma_{\text{eq}} = -110^0$, to a highly twisted conformation with 70^0 difference to the planar conformation. Examples of the observed phases are presented in figure (4.12). As expected, when a planar conformation is favoured, a normal, non-twisting, nematic phase is formed, top left in figure (4.12), with an orientational order parameter $S_2 \approx 0.67 \pm 0.02$, considering all the three rods in the molecule and averaged over all the molecules. From the snapshot of the nematic phase looking down along z-axis (perpendicular to the wall), top right panel of the figure (4.12), a planar alignment at the wall can be observed. When the equilibrium dihedral angle differs from the planar case, the molecule adopts a chiral shape. Now a formation of a twisted nematic phase with a uniform twist around the helical axis (z-axis in this case) is expected instead of a uniform nematic. A snapshot, with z-axis running along the page, of a twisted nematic is presented in the bottom left panel of figure (4.12) for the system with $\gamma_{\text{eq}} = -150^0$. Comparing this to the snapshot of the system with higher twisting molecules, $\gamma_{\text{eq}} = -120^0$, in the bottom right panel, an increase of the twist of the bulk phase can be observed upon increasing the twist of the individual molecule.

To quantify the effect of molecular twist on the twist of the bulk phase, the simulation box was divided into layers with thickness of $1.7\sigma_0$ along the z-axis. A

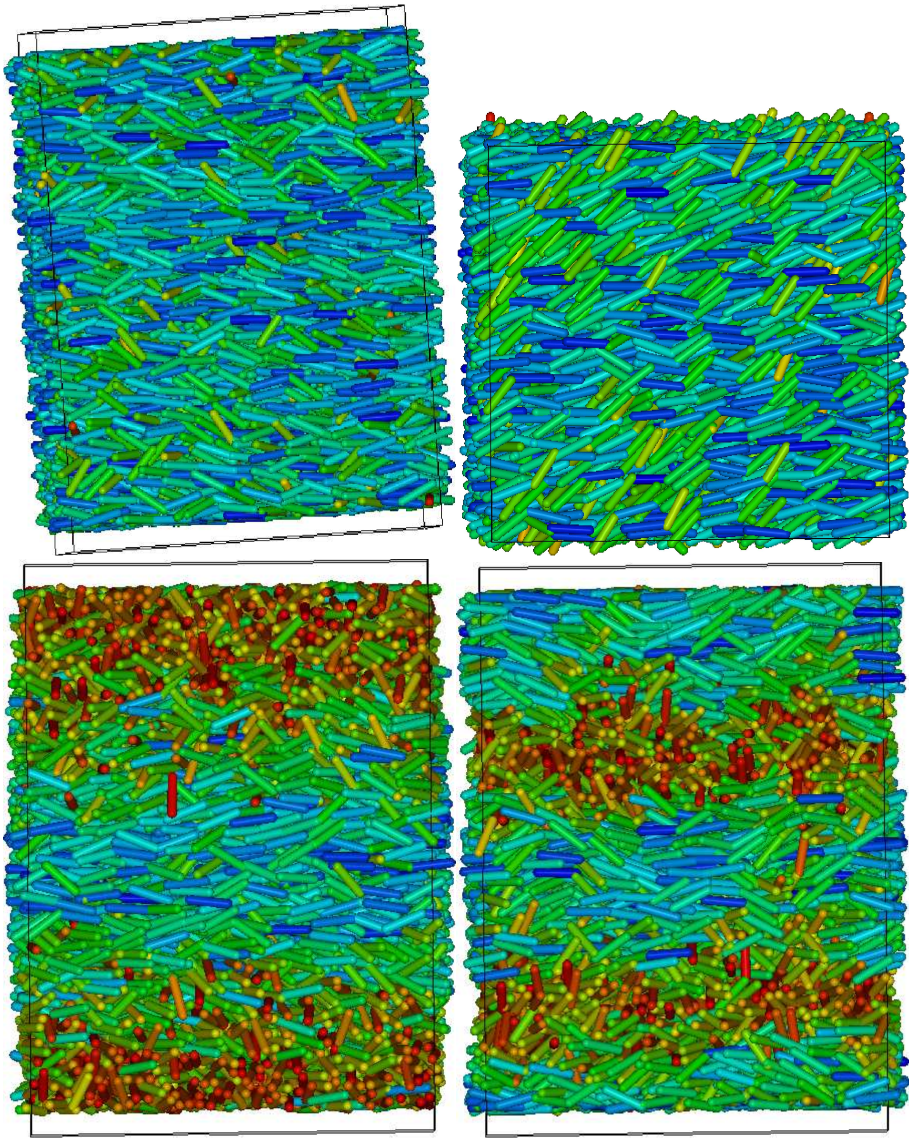

Figure 4.12: Snapshots obtained from, $N = 4000$, simulations of model bent-core molecules. Achiral nematic phase with the molecular equilibrium dihedral angle of $\gamma_{\mathrm{eq}} = 180^0$, side view (top left) and top view showing planar alignment at the surface (top right). Chiral nematic phase with $\gamma_{\mathrm{eq}} = 150^0$ (bottom left) and $\gamma_{\mathrm{eq}} = 120^0$ (bottom right).

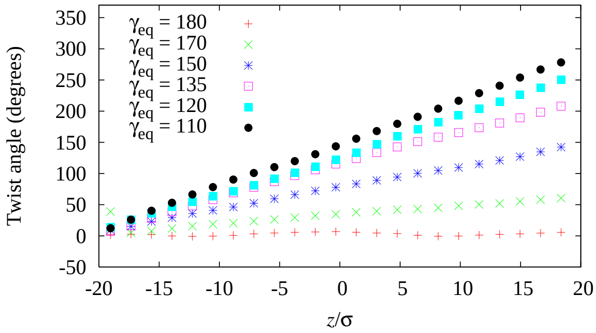

Figure 4.13: The angle between a reference nematic director, $\mathbf{n}_{\text{ref}}$, at the bottom the simulation box and a local nematic director, $\mathbf{n}_{\text{layer}}$, for a corresponding layer. The results are presented for the six systems considered with equilibrium dihedral angle in the range $\gamma_{\text{eq}} = 180^0 \ldots 110^0$.

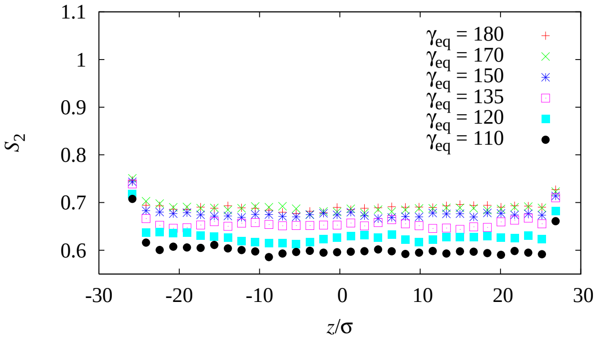

Figure 4.14: Orientational order parameter, S_2, for the layers along the helical, z, axis for the six systems considered, with equilibrium dihedral angle in the range of $\gamma_{\text{eq}} = 180^0 \ldots 110^0$.

local nematic director was used for each layer, $\mathbf{n}_{\text{layer}}$. This allowed the calculation of the twist angle, $\phi(z/\sigma_0)$, between a reference director close to the bottom of the box and a local director of the layer along the z-axis (Figure 4.13). The effect of conformational (molecular) chirality on the bulk twist is clearly present. The overall twist is seen to increase from, $\phi \approx 0$, for the planar (achiral) molecules with $\gamma_{\text{eq}} = 180^0$ to $\phi \approx 278^0$ for the highest chiral strength with $\gamma_{\text{eq}} = -110^0$. The linear nature of the twist angle, $\phi(z/\sigma_0)$, between the local directors allows the bulk pitch, p, to be obtained from a linear fit, $\phi(z^*) = az^* + b$, as $p = 2\pi/a$.

The local nematic order parameter, S_2, for the layers is presented in figure 4.14. All the systems considered are well in the nematic region. When averaged over all the layers, a limiting values can be identified as $S_2 \approx 0.67 \pm 0.02$ for the achiral system and $S_2 \approx 0.604 \pm 0.004$ for the the most twisting system with $\gamma_{\text{eq}} = -110^0$.

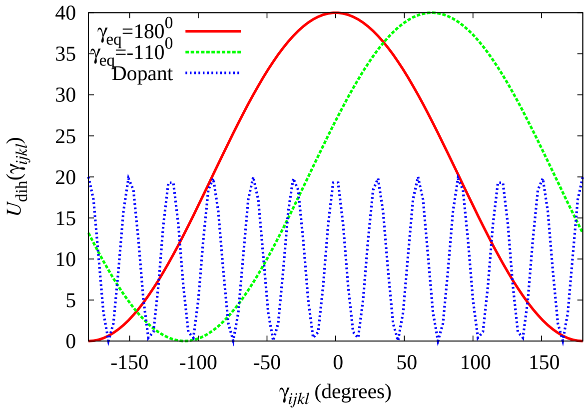

Figure 4.15: Examples of dihedral potentials used in simulations. Achiral model with $\gamma_{\text{eq}} = 180^0$, equation (4.2) with $A = 20.0,\ n = 1,\ \gamma_0 = 0$ (solid line); chiral model with $\gamma_{\text{eq}} = -110^0$, equation (4.2) with $A = 20.0,\ n = 1,\ \gamma_0 = 70.0$ (dashed line); achiral dopant with 12 wells, equation (4.2) with $A = 10.0,\ n = 12,\ \gamma_0 = 0$.

A small effect due to the aligning wall can be seen from the extreme values, z_{min} and z_{max}, of S_2, where a small increase (a maximum) of approximately 0.1 occurs. This increase disappears rapidly with S_2 being within the statistical error of the bulk value for adjacent layers.

4.2.4.2 Systems with dopants

To study the effect of the host phase on the structure of a flexible achiral dopant molecule, two host systems with $\gamma_{\text{eq}} = 180^0$ and $\gamma_{\text{eq}} = -110^0$ were doped with flexible dopant molecules, by replacing 10% of the molecules in the already equilibrated systems by dopant molecules. This kept the total number of molecules constant, $N = 4000$, and resulted in $N_{\text{solvent}} = 3636$ and $N_{\text{dopant}} = 364$. The dopant molecules were modelled exactly as the solvent, but their dihedral angle potential was modelled with equation (4.2), choosing $A = 10.0,\ n = 12,\ \gamma_0 = 0$, resulting, on average, in an achiral structure, with 12 equally spaced wells (figure 4.15) corresponding to different twists. Both systems were then run for 3 million MD steps.

In this very simplified case, the effect of the host phase on the structure of the dopant molecules can be directly assessed by calculating the dihedral angle distribution, $f(\gamma_{ijkl})$. This is presented in figure 4.16 for the solvent (solid line) and dopant molecules (dashed line). For the dopant molecules in an achiral host

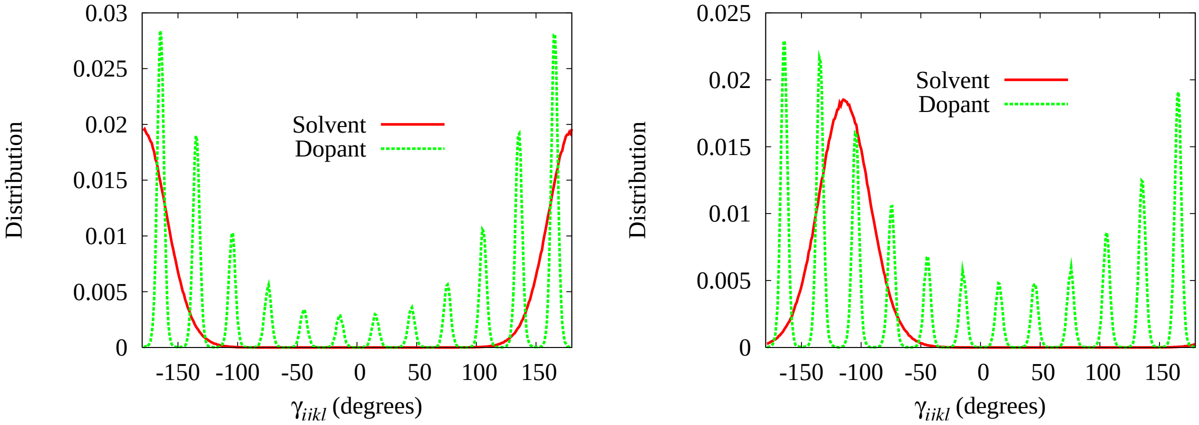

Figure 4.16: A dihedral angle distribution calculated from MD simulations for systems with 10 % of doping, $N_{\text{Solvent}} = 3636$ and $N_{\text{Dopant}} = 364$, with an achiral dopant with 12 evenly distributed wells (Figure 4.15). Achiral solvent with $\gamma_{\text{eq}} = 180^0$ (left) and chiral solvent $\gamma_{\text{eq}} = -110^0$ (right).

phase (left panel) the solvent dihedral angle distribution is symmetric around the equilibrium value of $\gamma_{\text{eq}} = 180^0$. The distribution for the dopant molecules shows a symmetric distribution of 12 peaks around $\gamma_{ijkl} = 0$, showing that the dopant molecules are indeed achiral in a nematic reference field. Interestingly, the dopant molecules prefer conformations similar to the host phase, which is shown by the growth of the peaks close to $\gamma_{ijkl} = 180^0$ and suppression of peaks close to $\gamma_{ijkl} = 0$, relative to the unperturbed gas phase distribution, which can be assumed to be a Boltzmann inversion of the potential energy function (dotted line in figure 4.15), with all peaks having an equal area. This conformational selectivity is apparent also in the chiral host phase (right panel). Here the dihedral angle distribution for the solvent is symmetric around $\gamma_{\text{eq}} = -110^0$, but the dopant molecules now become chiral with a preferential selection of conformations which are twisted in the same direction as the host phase (right panel in figure 4.16).

To study the chiral induction further, dopant molecules with only two equilibrium dihedral angles, were considered, corresponding to states which are characterised by equal but opposite chirality. Marking the molar fraction of these molecules in left- and right-hand conformations by n_L and n_R, respectively. It must be true that $n_L + n_R = 100\%$. Further, in an achiral phase, such as the gas phase, an isotropic liquid or an uniform nematic phase, the relation $n_L = n_R$ must hold. For this

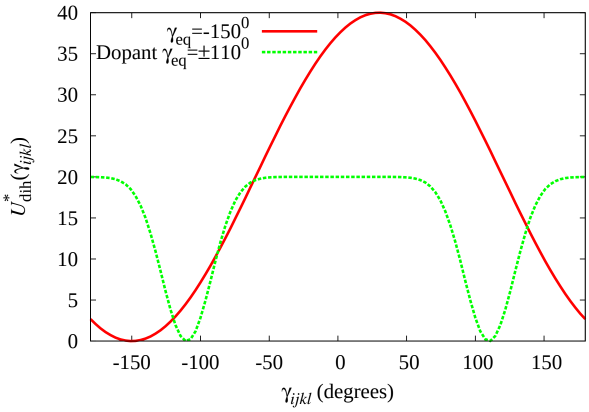

Figure 4.17: Dihedral potentials for chiral solvent with $\gamma_{\text{eq}} = -150$ (solid line) and achiral dopant molecule with two equal but opposite chiral conformations, $\gamma_{\text{eq}} = \pm 110$ (dashed line).

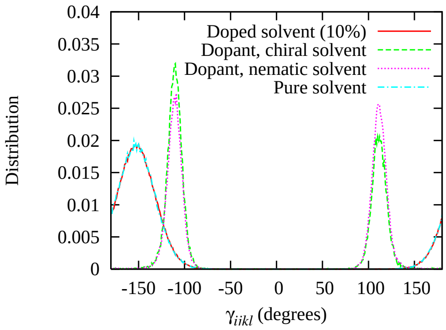

Figure 4.18: Dihedral angle distributions from MD simulations. Doped solvent (solid line), dopant in a chiral solvent (dashed line), dopant in a nematic solvent (dotted line) and solvent without dopant molecules (dot-dashed line).

dopant molecule, a dihedral potential of form equation (4.3) with parametrisation $A = 20$, $n = 40$ and $\gamma_0 = 55$ was employed. Leading to two symmetrical wells at $\gamma_{\text{eq}} = \pm 110$ separated by a barrier of height $20\epsilon_0$ (dashed line in figure 4.17). Two host systems with 10% doping were considered: an achiral host phase and a chiral host phase with $\gamma_{\text{eq}} = -150^0$ (solid line in figure 4.17). Systems were constructed as in the previous case and run for 4 million MD steps.

Again, the conformational chirality of the dopant molecules was estimated by calculating the dihedral angle distribution function. This is presented in figure 4.18 for the dopant molecules in the nematic host phase (dotted line) and in the chiral nematic host phase (dashed line). The relative populations, n_L and n_R, can be calculated by integrating the area under the corresponding peak. This was done nu-

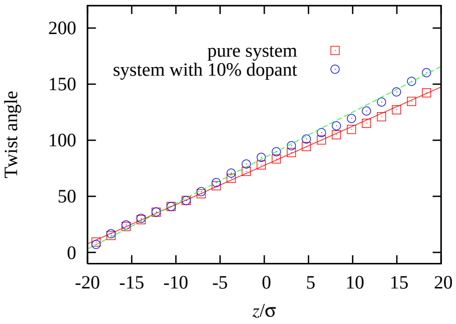

Figure 4.19: Bulk twist angle, $\phi(z)$, for local directors along the helical, z, axis for the system with $\gamma_{\text{eq}} = -150^0$ for two cases: A pure melt (squares) and system with 10% doping (dopant molecules had two equal but opposite chiral conformations, $\gamma_{\text{eq}} = \pm 110$) (circles). The lines are least-squares fits of linear functions, $f(z) = az + b$, to the data.

merically using the trapezium method. In the nematic phase, the equality $n_L \approx n_R$ is true within statistical error, for the dopant molecules. However, when the dopant molecules are placed in the chiral host phase, (as seen before) a preferential selection of conformations with twist in the same direction as the host phase occurs. Relative populations of 59.3±0.5% and 40.7±0.5% were obtained for the conformations twisting the same direction and opposite direction as the host phase. These preferentially selected conformations, centred around $\gamma_{ijkl} = -110^0$, are higher twisting than the host phase, resulting in a higher twisting power as can be depicted from results for the bulk twist angles for the molecules with different level of twist, as presented in figure 4.13.

Figure 4.19 shows an increase of the bulk twist angle, $\phi(z/\sigma_0)$, for the system with 10% dopant molecules when compared to the pure melt. From the slope of the linear fit to the $\phi(z/\sigma_0)$, the pitch, p, of the chiral nematic phase can be calculated. The pitch was found to be $p = (88.5 \pm 1.0)\sigma_0$ and $p = (103.2 \pm 0.7)\sigma_0$ for the doped and pure systems, respectively. This shows an approximate 17% increase of the bulk twist when the systems was doped with an achiral dopant. This seems quite a large increase. To check the results another simulation of 4 million MD steps was performed for the pure system. This time it was found that $p = (89.6 \pm 1.3)\sigma_0$, resulting in a more modest increase of approximately 1.2% of the bulk twist. A crucial requirement for this analysis is the linear behaviour of the $\phi(z/\sigma_0)$, which

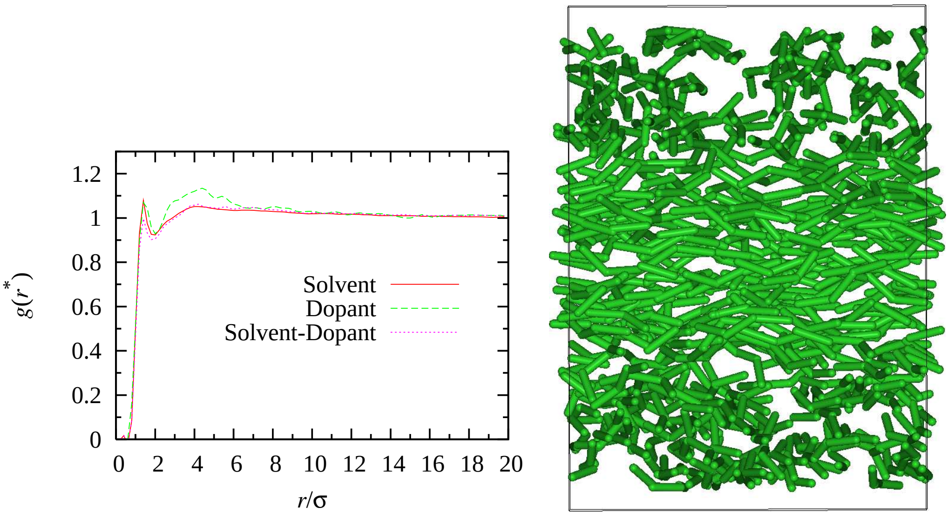

Figure 4.20: Radial distribution functions, $g(r^*)$, for solvent molecules (solid line), dopant molecules (dashed line) and solvent-dopant cross distribution (dotted line) on the left panel. Snapshot of the dopant molecules, where solvent molecules are removed for clarity, right panel. Results are for the solvent system with $\gamma_{\text{eq}} = -150^0$ doped with achiral dopant molecules with $\gamma_{\text{eq}} = \pm 110^0$.

is fulfilled for the systems shown in figure 4.19, but was less so for the second pure melt. The most probable reason for this is due to the aligning walls in the z-direction, leading to $\phi(z/\sigma_0)$ adopting a slightly less linear form. Despite these limitations, the simulations do demonstrate that a preferential selection of high twisting dopant conformers with a twist in the same directions as the host phase, can lead to an increase of the bulk twist of the chiral nematic system upon doping with an achiral dopant molecules. Moreover, these findings help to explain the experimental findings of Thisayukta *et al.* [193] that an achiral dopant can increase the twist of a bulk chiral nematic phase.

Considering the mechanism of how preferential selection of the dopant conformations lead to an increase of the bulk twist, three scenarios arise: firstly, dopant molecules could phase separate to form a highly twisting cluster leading to an increase in overall twist. Secondly, dopant molecules could affect the chirality of the solvent molecules (dihedral angle distribution, in this highly coarse grained case) making the solvent molecules more chiral and thirdly, dopant molecules are distributed evenly in the system but their preferentially selected high twisting conformations lead to an increase of the bulk twist.

To check these hypotheses for this system, the distribution of the dopant molecules was assessed in the terms of pair distribution functions, $g(r^*)$. Comparing the dopant molecules $g(r^*)$ (left panel of figure 4.20) to the solvent and solvent-dopant $g(r^*)$ it can be seen that that all of them have a nearest neighbour peak separation at approximately $r^* \approx 1.3$. For larger separations the solvent and solvent-dopant pair distribution functions quickly reach a constant value of 1, indicating liquid like order. The dopant $g(r^*)$ shows the growth of slight shoulder between separations of $r^* \approx 2.4$ and $r^* \approx 6.0$, indicating a slight preference for forming small clusters. For separation larger than $r^* > 6.0$ the $g(r^*)$ goes to constant value of 1. A similar picture can be seen from a snapshots of dopant molecules, where the solvent molecules have been removed for clarity. The dopant molecules are uniformly distributed across the simulation box, apart from some evidence for formation of very small clusters (right panel of figure 4.20). Figure 4.18 shows the calculated dihedral angle distributions for the solvent with 10 % doping (solid line) and for the pure solvent (dot-dashed line). These are in agreement within the line width, thus it can be concluded that the doping does not change the chirality of the solvent. The increase of the bulk twist arises almost entirely from the preferential selection of high twisting conformations of uniformly distributed dopant molecules.

4.2.4.3 Chiral segregation in nematic phase

A recent experimental study by Görtz *et al.* [195] of achiral bent-core *bis*-(phenyl)-oxadiazole derivatives, reported unusual properties in the nematic phase, including evidence of segregation into domains of opposite handedness. In figure 4.21 a snapshot of a uniform nematic phase is shown with colour coding according to the handedness of individual molecules. From this it can be seen how locally the molecules prefer the same handedness as their neighbours leading to segregation into small domains with opposite handedness. Here however, the chiral domains are quite small as opposed to the findings in [195]. It is an interesting and currently open question as to whether preferential selection of chiral conformations in an achiral nematic phase can lead to true "phase separation" of large scale macroscopic (μm) domains with opposite handedness.

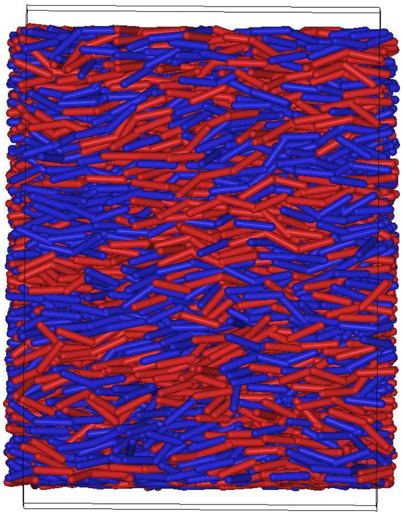

Figure 4.21: A snapshots showing chiral segregation in a uniform nematic phase ($\gamma_{\mathrm{eq}} = 180^0$) where the colour coding has been applied as blue for "left"-handed and red for "right"-handed conformations.

4.2.5 Conclusion for chiral induction

Chiral induction was studied using a coarse grained model constructed from three anisotropic sites, modelled as soft-core spherocylinders, connected together using harmonic bonds and angles. A dihedral potential describing rotation around the middle spherocylinder was introduced to control the conformational chirality of individual coarse grained molecules. The simulation showed that when an achiral equilibrium structure was set, the bulk system formed a uniform nematic phase. When conformational chirality was introduced a twisted nematic phase was formed with the twist of the bulk phase increasing upon increasing the twist of the individual molecules. Further, simulations demonstrated an increase in bulk twist, through the preferential selection of high twisting conformations, when the system was doped with on average achiral dopant molecules. Finally, an evidence of a local segregation into domains with opposite handedness was observed in a uniform nematic phase.

4.3 Conclusions

In this chapter the new soft-core model developed in chapter 3 was applied to two different systems. The first simulation study, presented in section 4.1, consisted of mapping an approximate phase diagram for a main chain liquid crystalline polymer as a function of the volume fraction for the mesogenic unit. Simulations also demonstrated a rich phase behaviour corresponding to the formation of nematic and lamellar phases for large rod volume fractions. In the middle of the phase diagram, a large lamellar stability was observed. For small rod volume fraction some evidence for formation of cylindrical micelles was present and for intermediate values the formation of a gyroid phase was observed.

In the second study, presented in section 4.2, chiral induction was studied by considering flexible dopant molecules within a chiral nematic solvent. Here, results demonstrated that dopant conformers preferred twisting the same direction as the host phase. Moreover, evidence was obtained, this preferential selection leading to an increase of overall twist of the host phase. Finally, evidence of chiral segregation in an achiral nematic phase was seen. These result demonstrate, that these highly coarse grained models, used in meaningful ways, can provide results of experimental interest and to help to explain experimental observations.

Chapters 3 and 4 have introduced and used the new anisotropic soft-core model within conventional MD framework. In the remaining three chapters (5, 6 and 7), three different advanced simulations methods, will be considered. In chapter 5 coarse grained surfactant system is studied. The solvent interactions are modelled using Stochastic Rotational Dynamics method, introduced in section 2.2.5, this allows for a computationally very efficient description of the solvent-solvent interactions, with the further advantage that SRD conserves momentum leading to correct hydrodynamics on large time and length scales. In chapter 6 the new anisotropic model is combined with a relatively new advanced simulation method, Statistical Temperature Molecular Dynamics (STMD). STMD allows the construction of microcanonical temperature (as a function of internal energy) for a given temperature range in a single simulation. This provides the possibility of constructing relevant thermodynamic variables such as entropy and free energy. Finally in the chapter 7, Hamiltonian Replica Exchange Molecular Dynamics (HREMD) is applied to a Gay-Berne system bridging the isotropic-nematic phase transition.

Chapter 5

Stochastic rotational dynamics simulations of surfactant self-assembly

5.1 Introduction

The ability of surfactant molecules to aggregate in solution to form micelles and other ordered phases is due to the amphiphilic nature of the molecules, *i.e.* each molecule consists of hydrophobic and hydrophilic parts. The ability of surfactant aggregates to change size, shape and topology under different physical or chemical conditions (for example temperature, solvent quality or salt concentration), is an important phenomena in biology and also in industry. Important quantities for a micellar solution include the average size of micelles, the micelle size distribution, the kinetics of micelle formation and disintegration and pathways for aggregate formation and rearrangement. For example understanding fusion and fission of surfactant aggregates would be a key element for targeted drug delivery [196]. Many of these phenomena are non-equilibrium in nature and involve complex molecular level processes. In an attempt to understand the kinetic pathways and physical mechanisms involved, various theoretical efforts have been tried previously, including coarse grained computer simulations. The time and length scales involved possess a great challenge for computer simulations. References [197–199] include three recent reviews of CG simulations of biological systems, including surfactants.

In a series of coarse grained studies, Pool and Bolhuis studied the free energies of micelle formation [200], critical micelle concentrations [201], kinetics of micelle fusion and fission [202] using conventional simulation techniques such as MC and MD in combination with advanced free energy techniques. They also suggested a new autocatalytic replication mechanism for micelle formation [203]. Recently, kinetics of formation and disintegration of spherical micelles have also been studied by a combination of MD and stochastic modelling [204].

To bridge the length and time scales an implicit solvent model for surfactants have been developed by using soft-core models in a dissipative particle dynamics framework [198, 205] and with tunable attraction [206]. Recently, Schmid *et al.* developed a generic model for lipids by using Lennard-Jones and Weeks-Chandler-Andersen potentials, coupled to a computationally very efficient “phantom solvent”. The latter, interacted repulsively with the lipids, but had no self-interaction [207, 208]. This model was used in series of Monte Carlo studies [207–210] of lipid monolayers and bilayers.

In this chapter simulations studies of model CG surfactant will be performed where the system is coupled to a phantom solvent modelled by stochastic rotational dynamics (section 2.2.5 in chapter 2). This model has the advantage of a computationally very cheap representation of the solvent interactions, while still maintaining the correct hydrodynamics, which is an essential requirement for studying non-equilibrium phenomena. The simulations were carried out by the thesis author while visiting the University of Pittsburgh for 8 weeks in spring 2008. All the simulations were performed using Pitt. Molecular Modelling (pmm) package developed in Prof. David J. Earl’s research group in the University of Pittsburgh. All the relevant implementations of SRD within pmm were carried out by Dr Christopher Adam Hixson from the University of Pittsburgh.

5.2 Computational details

The studies of surfactants in a mesoscopic water-like solvent were carried out by using a coarse grained (CG) surfactant model consisting of a hydrophilic head bead, (h), connected to hydrophobic tail beads (t). Each solvent particle, s, was represented by a single site. Non-bonded interactions were modelled using a Lennard-Jones potential

$$u^{\mathrm{LJ}}(r_{ij}) = 4\epsilon_{ij}\left[\left(\frac{\sigma_{ij}}{r_{ij}}\right)^{12} - \left(\frac{\sigma_{ij}}{r_{ij}}\right)^{6}\right], \tag{5.1}$$

where ϵ_{ij} is the potential well depth, σ_{ij} is the interaction range between particles i and j calculated from the sizes as $\sigma_{ij} = 1/2(\sigma_i + \sigma_j)$ and r_{ij} is the distance between particles i and j. To allow the potential to go smoothly to zero, the potential was truncated at a cutoff distance r_{cut} and shifted

$$u(r_{ij}) = \begin{cases} u^{\mathrm{LJ}}(r_{ij}) - u^{\mathrm{LJ}}(r_{\mathrm{cut}}) & \text{if} \quad r_{ij} \leq r_{\mathrm{cut}} \\ 0 & \text{if} \quad r_{ij} > r_{\mathrm{cut}} \end{cases}, \tag{5.2}$$

using a cutoff radius $r_{\mathrm{cut}} = 2.5\sigma_0$. Purely repulsive interactions were modelled using Weeks-Chandler-Andersen potential (WCA) [211]

$$u^{\mathrm{WCA}}(r_{ij}) = \begin{cases} 4\epsilon_{ij}\left[\left(\frac{\sigma_{ij}}{r_{ij}}\right)^{12} - \left(\frac{\sigma_{ij}}{r_{ij}}\right)^{6}\right] + \epsilon_{ij} & \text{if} \quad r_{ij} < 2^{(1/6)}\sigma_{ij} \\ 0 & \text{if} \quad r_{ij} \geq 2^{(1/6)}\sigma_{ij} \end{cases}. \tag{5.3}$$

The consecutive beads were connected through a harmonic spring potential

$$u^{\mathrm{bond}}(r_{ij}) = \frac{k_{\mathrm{bond}}}{2}\left(r_{ij} - r_0\right)^2, \tag{5.4}$$

where k_{bond} is the spring constant and r_0 is the equilibrium bond length. The chain rigidity was controlled through a harmonic angle potential for angle, θ_{ijk}, between three consecutive beads i, j and k

$$u^{\mathrm{angle}}(\theta_{ijk}) = \frac{k_{\mathrm{angle}}}{2}\left(\theta_{ijk} - \theta_0\right)^2. \tag{5.5}$$

The solvent was modelled using stochastic rotational dynamics (SRD) introduced in

Table 5.1: Non-bonded parameters employed in simulations for the head h, tail t and solvent s pair interactions. The epsilon, ϵ_{ij}, for the Lennard-Jones interaction was chosen as $\epsilon_{ij} = 1.0\epsilon_0$ unless stated otherwise[a].

Interaction		h	t	s	σ_i/σ_s
Model A	h	WCA	WCA	WCA	1.1
	t	WCA	LJ	WCA	1.0
	s	WCA	WCA	SRD	1.0

Interaction		h	t	s	σ_i/σ_s	ϵ_{ij}/ϵ_0[a]	h
Model B	h	WCA	WCA	LJ	2.0	s_1	1.0
	t	WCA	LJ	WCA	1.0	s_2	0.75
	s	LJ	WCA	SRD	1.0	s_3	0.5
						s_4	0.25

SRD	collision time step	rotation angle α	unit box length a_0
	$5 \times \Delta t_{\mathrm{MD}}$	90	1.0

section 2.2.5 of chapter 2. The SRD solvent was coupled to the CG-surfactants by a hybrid MD scheme (section 2.2.5) with the interaction modelled by LJ and WCA potentials. The non bonded interaction parameters are summarised in table 5.1.

In all the simulations the mass of each bead was set to $m = 1$ and the equations of motion were integrated using a Nosè-Hoover thermostat and the velocity-Verlet algorithm with timestep $\delta t = 10^{-3}\tau$, where $\tau = \sqrt{m\sigma_s/\epsilon}$ is the reduced time unit.

5.3 Self-assembly of lipid bilayers

For studying the applicability of a SRD solvent for the formation of self assembled lipid bilayers a simulation study of a coarse grained lipid model was carried out. Each lipid consisted of a head bead h bonded to chain of 6 tail beads ($\mathrm{h}_1\mathrm{t}_6$). Harmonic bond and angle potentials were employed with force constants $k_{\mathrm{bond}} = 100.0/\ (\epsilon_0\ \sigma_s^{-2})$, $k_{angle} = 4.7\ /(\epsilon_0\ \mathrm{rad}^{-2})$ with an equilibrium bond length $r_0 = 0.7\sigma_{ij}$ and an equilibrium angle $\theta_0 = 180.0^0$ for the bond and angle potentials respectively. For the non-bonded interactions an attractive Lennard-Jones and repulsive WCA-potential were used. The non-bonded parameters are summarised in table 5.1 as model A. The coarse grained lipid model is very similar to one used previously in Monte Carlo studies of Langmuir monolayers [209], and in studying the formation of rippled phase in a lipid bilayer system [210], where it was coupled with a phantom solvent [207, 208]. It must be noted that the interaction potentials used in this study, intra- as well as intermolecular, differ slightly from those used in references [207–210].

Initially the system of $N = 512$ lipid molecules were placed in three different sized cubic simulation boxes with box lengths $L = 18,\ 19$ and 20σ. Each system was then run for 500 000 MD steps in the NVT ensemble with a fairly high reduced temperature, $T^* = 3.0$, to ensure an isotropic starting configuration for the SRD simulations. The SRD solvent particles were inserted in the void of the isotropic (gas) phase of the lipids minimising the overlap between solvent particles and lipid monomers. The SRD solvent parameters are given in table 5.1. 2 SRD particle per unit box, $V_0 = a_0^3$, were used giving solvent free density of $\rho_{\mathrm{s}}^{\mathrm{free}} = 2.0$.

Given that the state point, temperature T^* and density ρ^*, are favourable, the lipids will self assemble into a stable bilayer. The important quantity in simulation of the bilayers is the area across the simulation box perpendicular to one of the axes, as the bilayer is stabilised with its periodic image along this cross section. Further, the surface tension of the bilayer should be zero as a biological membrane when being free of any external constraints adopts a configuration in which it is tensionless [212]. This could be achieved by altering the area of the bilayer such a way that the total volume of the simulation box remains constant [205]. Another possibility would be to use an iterative scheme, *i.e.* run multiple simulations with different cross section and choose the one where the area per lipid is such that the bilayer adopts a stress free configuration. In references [213, 214] this method was used.

Changing box dimensions is a non-trivial exercise with the current state of SRD algorithm. In this study the aim was to test if the SRD solvent could be used to drive the isotropic lipid system to self-assemble into a bilayer rather than to rigorously study of phase changes between different bilayer phases where a condition of the bilayer being tensionless is an essential requirement for reliable data. For the system with a simulation box length of $L = 18\sigma_s$, the system quickly self-assembled into a bilayer in the yz-plane after approximately 300 000 MD steps. The equilibrium temperature of the system settled at $T^* \approx 2.1$. The system was monitored for

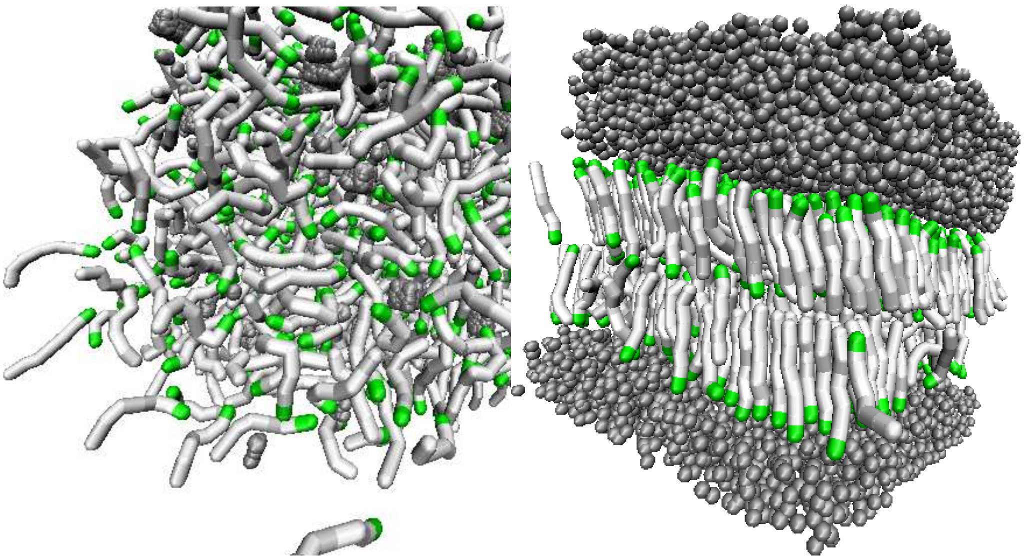

Figure 5.1: Snapshots from simulations of $N = 512$ lipid molecules, head groups (h) are coloured green and tails (t) white, in a SRD solvent with solvent free density $\rho_s^{\mathrm{free}} = 2.0$ with simulation box size $L = 18\sigma_s$. An isotropic starting configuration (left) where SRD solvent particles are inserted in voids minimising the overlap with lipid molecules. Self-assembled bilayer (right) where the lipid molecules are organised as a bilayer with, on average, the hydrophobic tails shielded from the solvent by hydrophilic head groups.

a further 700 000 MD steps during which the bilayer diffused along x-axis. The snapshot of the initial configuration and self-assembled bilayer are presented in the figure 5.1.

5.4 Formation of micelles

The formation and kinetics of micelles in a SRD solvent was studied using a $\mathrm{h}_1\mathrm{t}_4$ surfactant with fairly large, $\sigma_{\mathrm{h}} = 2\sigma_{\mathrm{s}}$, head group connected to four tail beads $\sigma_{\mathrm{t}} = \sigma_{\mathrm{s}}$. Consecutive beads, i and j, were bonded to each other through a harmonic spring potential with an equilibrium bond length $r_0 = 0.7\sigma_{ij}$ and a force constant $k_{\mathrm{bond}} = 5000\ \epsilon_0\sigma_s^{-2}$. No angle potentials were used. The non-bonded interaction parameters are summarised in table 5.1 as model B.

Initially $N = 676$ surfactant molecules were placed into a cubic simulation box with $L = 30\sigma_{\mathrm{s}}$ and run in a NVT ensemble at reduced temperature of $T^* = 3.0$ for 500 000 MD steps to ensure an isotropic starting configuration for the SRD simulations. 16200 SRD solvent particles were then inserted into the voids between

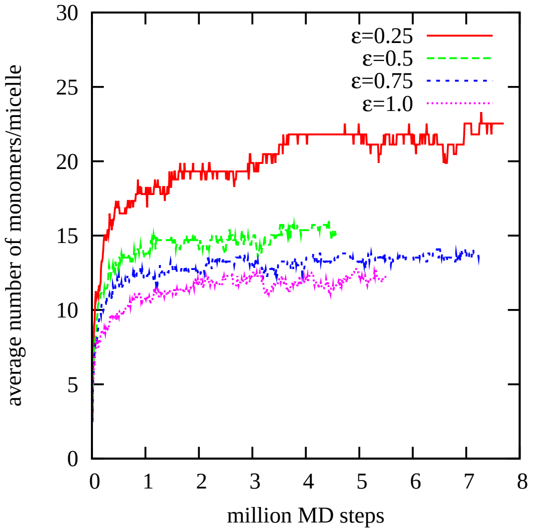

Figure 5.2: The average number of monomers in an individual micelle as a function of molecular dynamics steps obtained from SRD simulations of $N = 676$ model h_1t_4 surfactants. The results are presented for four different systems with different attraction between the solvent (s) beads and the head groups (h) with well depths $\epsilon_{sh} = 1.0,\ 0.75,\ 0.5$ and $\epsilon_{sh} = 0.25$.

surfactant molecules, resulting in a solvent free density of $\rho_{\mathrm{s}}^{\mathrm{free}} = 16200/30^3 \approx 0.6$ and to (surfactant) bead number density $\rho^* = N_b/V \approx 0.125$. The system was left to equilibrate and evolve in time, keeping the reduced temperature at $T^* \approx 1.03$. For analysing micelle growth and dynamics snapshots were written to disk every 10000 MD steps. Two molecules were deemed to belong to the same micelle if their terminal tail beads were within a cut-off distance of $r_{\mathrm{cut}} = 2.5\sigma_s$.

5.4.1 Isotropic starting configuration

For studying solvation effects on micelle growth four different solvents were considered with attractive interaction between solvent beads (s) and the the large head beads (h) with well depths $\epsilon_{sh} = 1.0,\ 0.75,\ 0.5$ and $\epsilon_{sh} = 0.25$. The average micelle size, *i.e.* the number of monomers per individual micelle as a function of MD steps is presented in figure 5.2. Initially the micelles are formed by free monomers aggregating into micelles. Since the simulated systems are far above the critical micelle concentrations ($\rho^{\mathrm{CMC}}/\rho_s \approx 10^{-6}$ [200, 201] for this kind of surfactant models) aggregation occurs very quickly. The average micelle size was calculated averaging over the final 500 000 MD steps of the simulation. It was ob-

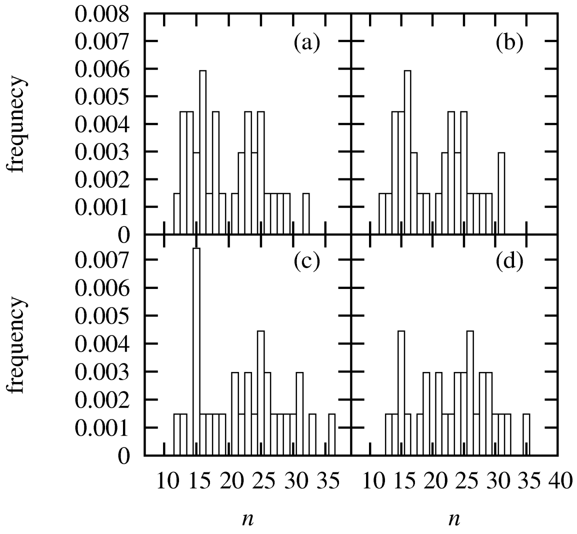

Figure 5.3: Time time evolution of the micelle size distribution from the system with the well depth for solvent and head group interaction $\epsilon_{sh} = 0.25$ calculated at four different simulation stages: (a) averaged between 1.9-2.0 million steps, (b) 2.9-3.0 million steps, (c) 4.9-5.0 million steps and (d) between 6.9-7.0 million steps.

served to be $\langle N_m \rangle \approx 12.13 \pm 0.03$, $\langle N_m \rangle \approx 13.70 \pm 0.03$, $\langle N_m \rangle \approx 15.51 \pm 0.04$ and $\langle N_m \rangle \approx 22.46 \pm 0.04$ for the systems with $\epsilon_{sh} = 1.0,\ 0.75,\ 0.5$ and $\epsilon_{sh} = 0.25$ respectively.

Interestingly, the system with the smallest well depth, $\epsilon_{sh} = 0.25$, between the solvent and the head group, displays a noticeable jump of the average micelle size between 3 and 4 million MD steps. This suggest that there also exists a secondary process by which micelles grow. To study this further a micelle size distribution was calculated at different points during the simulation for the system with $\epsilon_{sh} = 0.25$. From the figure 5.3 it can be observed how the distribution of number of monomers per individual micelle changes over the course of simulation despite lack of small aggregation number aggregates.

These observed changes could happen through multiple pathways; a single monomer could escape from an existing micelle, it would then quickly aggregate into another micelle. For micelles close to the equilibrium size, this seems quite unlikely since the free energy barrier for removing a single surfactant and from an existing micelle is quite high [200,201]. Recently, Pool and Bolhuis suggested an autocatalytic replication mechanism for micelle formation [203] in which a micelle grows by adding single monomers by diffusion. When reaching critical size the micelle becomes unstable

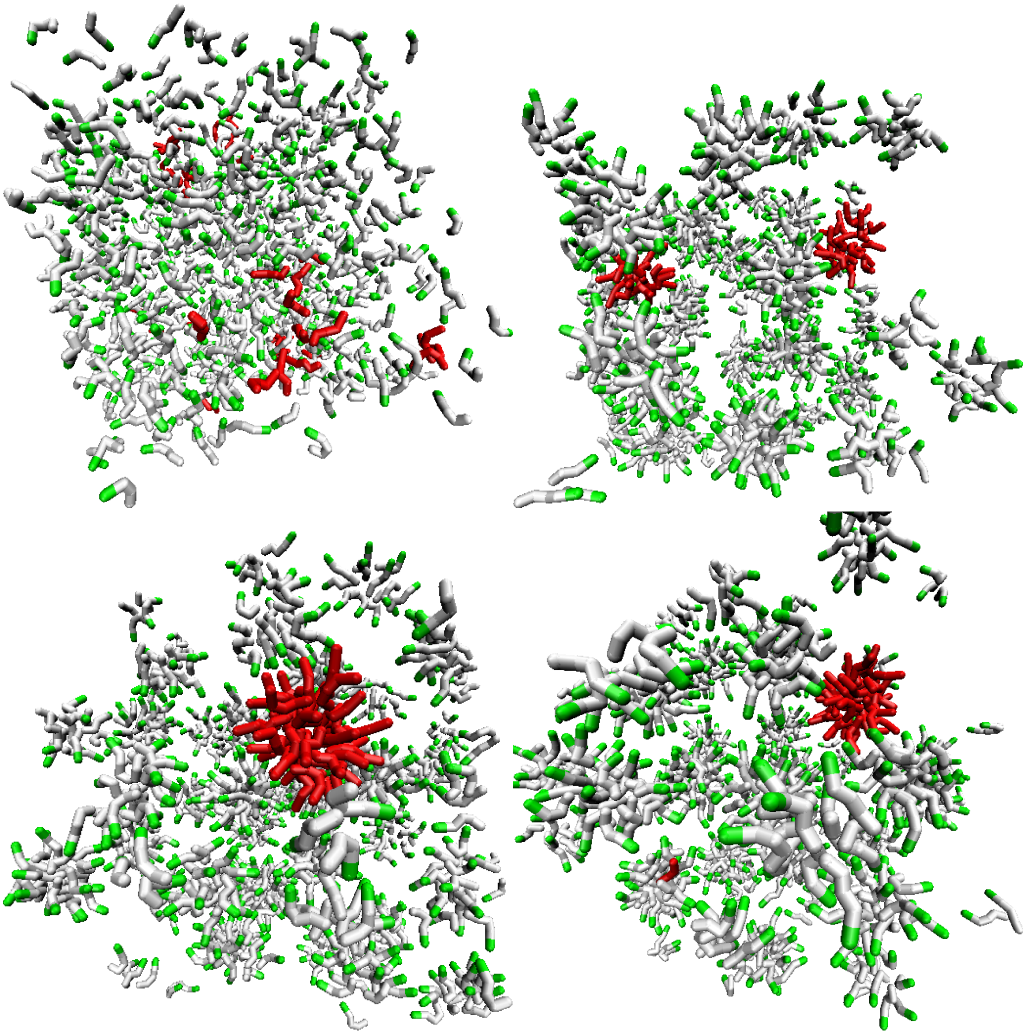

Figure 5.4: Snapshots from four different stages of the simulation: Top left isotropic starting configuration. Top right free monomers have aggregated into micelles of variable size after approximately 2 million MD steps. Bottom left, the two smaller red coloured micelles have fused together to form a large micelle after approximately 4 million MD steps. Bottom right, the end configuration. One monomer has escaped from the large red coloured micelle and joined into another micelle.

and it splits into two daughter micelles. Naturally in order to facilitate detailed balance a reverse reaction *i.e.* fusion of two micelle should be possible. The kinetics of the micelle fusion and fission transition was recently studied [202] for similar models to those considered here. It was found that the fusion rate is a factor 10 higher than the fission rate for h_1t_4 surfactant molecule with head to tail size ratio 1.5:1 where micelle/s of aggregation number $n = 50$ were considered. The fusion of two micelles was also recently reported in united atom simulations of DeTAB surfactants [215].

In figure 5.4 a series of snapshots is presented for the system with $\epsilon_{sh} = 0.25$ from different stages of the simulation to highlight one observed micelle growth mechanism. At top left the isotropic starting configuration is presented with the solvent beads removed for clarity. The monomers quickly aggregate into variable sized micelles. On top right a snapshot of the system after approximately 2 million MD steps is presented. Now the monomers highlighted in red have self-assembled into two micelles with aggregation numbers of $n = 14$ and $n = 22$, respectively. After approximately 4 million MD steps the two red micelles have fused together to form a large “supermicelle” with aggregation number of $n = 36$ (figure 5.4 bottom left). This can also be observed from the shrinking of the bars corresponding to the aggregation numbers of $n = 14$ and $n = 22$ between the micelle size distribution calculated at 2.9-3.0 and 4.9-5.0 million MD steps as shown in figure 5.3(b,c) as well as the appearance of the bar at the aggregation number $n = 36$ in figure 5.3(c). The end configuration of the simulation is presented in bottom right of the figure 5.4. It can be seen that the supermicelle highlighted in red has lost one monomer which has then aggregated into another micelle. This is also evident from the shifting of the bar at aggregation number $n = 36$ to $n = 35$ between the graphs 5.3(c) and 5.3(d). This mechanism where two smaller micelles fuse together into a large “supermicelle” which then decays to smaller more stable micelle by stepwise removal of monomers, as presented in snapshots in figure 5.4, might be particularly important in adsorption kinetics of micellar solutions [216].

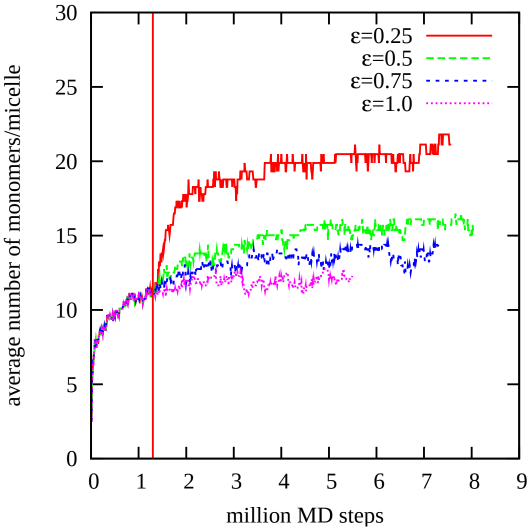

Figure 5.5: The average number of monomers in individual micelle as function of molecular dynamics steps obtained from SRD simulations of $N = 676$ model h_1t_4 surfactants. Initially the system was run with well depth between the solvent s beads and the head groups h as $\epsilon_{sh} = 1.0$. After 1.3 million MD steps the well depth was set to $\epsilon_{sh} = 0.75,\ 0.5,\ 0.25$. The change in solvent quality is marked with the vertical line.

5.4.2 Micelle saturated starting configuration

As the starting configuration for the simulations with solvent (s) head group (h) well depths $\epsilon_{sh} = 0.75,\ 0.5$ and $\epsilon_{sh} = 0.25$ a configuration with averaged micelle size $\langle N_m \rangle \approx 11.14 \pm 0.06$ was used. This configuration was achieved by running a simulation with $\epsilon_{sh} = 1.0$ for 1.3 million MD steps starting from an isotropic configuration. The time evolution of the average micelle size for these systems is shown in figure 5.5 where the change in solvent quality after 1.3 million MD steps is marked by a vertical line. The systems quickly relaxed, giving the average number of monomers per micelle (averaged over the last 500 000 MD steps) $\langle N_m \rangle \approx 13.82 \pm 0.05$, $\langle N_m \rangle \approx 15.82 \pm 0.05$ and $\langle N_m \rangle \approx 21.19 \pm 0.08$ for the systems with $\epsilon_{sh} = 0.75,\ 0.5$ and $\epsilon_{sh} = 0.25$ respectively.

The curve of the average micelle size for the system with $\epsilon_{\mathrm{sh}} = 0.25$ shows a rapid rise between 1.3 to 2.0 million MD steps after which, it continues to rise at more slowly arriving at $N_m \approx 20.0$ after approximately 4 million MD steps. To study the micelle growth process, the size distribution of the micelles was calculated at different times along the simulation trajectory. This is shown in figure 5.6. Comparing

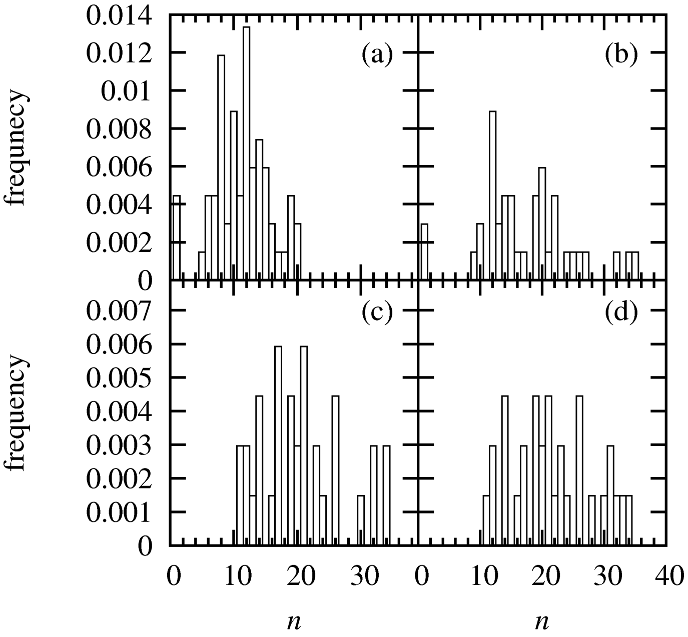

Figure 5.6: The time evolution of the micelle size distribution of the system with $\epsilon_{sh} = 0.25$. (a) The starting configuration for the simulations with $\epsilon_{sh} = 0.25$ (as explained in the text) calculated between 1.2-1.3 MD steps, (b) between 1.9-2.0 million MD steps, (c) between 4.9-5.0 million MD steps and (d) between 6.9-7.0 million MD steps.

the starting configuration for the simulation with $\epsilon_{\mathrm{sh}} = 0.25$, figure 5.6(a), to the distribution calculated between 1.9-2.0 million MD steps, 5.6(b), it can be seen how the distribution shifts towards larger micelles including the disappearance of the bars at aggregation number $n = 5,\ 6,\ 7$ and $n = 8$ and the appearance of the large super micelles at aggregation numbers $n = 34$ and $n = 35$. At a later stage, averaged between 4.9-5.0 million MD steps, the distribution shows growth of the bars at aggregation numbers $n = 32$ and 34 as well as shrinkage of the bar at aggregation number $n = 10$ (figure 5.6(c)). There is also a notable difference between 5.6(c) and 5.6(d) which have been calculated between 6.9-7.0 million MD steps. This suggests that even when the average micelle size, as show in figure 5.2, stays relative constant the size distribution itself evolves despite the lack of free monomers.

5.5 Conclusions

A coarse grained (CG) simulation model to study the formation of bilayer and micelles has been developed by coupling a stochastic rotational dynamics (SRD) solvent to a CG surfactant model. The results demonstrated formation of a bilayer when the density and the temperature were favourable. The formation of micelles was studied in a variety of different solvent qualities. The results showed, that the average micelle size was increased when the attraction between the hydrophilic head beads and solvent was reduced. Experimentally, this would correspond to adding ions (salt) to the solution leading the ions to screen the electrostatic repulsion between head beads. The pathways for surfactant aggregation were monitored both visually and by calculating the micelle size distributions at various points along the simulation trajectory. These showed how the size distribution evolves despite the lack of small aggregation number aggregates, suggesting a secondary process in micellar growth. One such a process, namely a fusion of two micelles, was directly observed in the simulations.

Due to the low computational cost of the solvent-solvent interaction and at least partly the lack of solvent structure, combined with correct hydrodynamics, the approach presented shows promise for future simulation of large scale non-equilibrium process, such as the merger of two vesicles.

Chapter 6

Statistical-Temperature Molecular Dynamics simulations of self-organising fluids

6.1 Introduction

The simulation work presented in chapters 3 and 4 highlighted some of the difficulties associated with predicting the phase behaviour of self-organising complex liquids. Typically, the potential energy landscape of a complex system is characterised by multiple local minima separated by potential energy barriers. For fairly simple systems at low density and high temperature, conventional MC and MD methods provide sufficient sampling of phase space. Moving to more complex systems at high density or low temperature, potential energy barriers can easily prevent conventional MC or MD simulations accessing all the relevant configurations within reasonable computational time. This leads to a failure in the correct sampling of the phase space. A second problem with conventional molecular simulation techniques are, that thermodynamic quantities such as entropy and free energy are not readily available.

In addition to the soft-core potentials and SRD presented earlier in this thesis, a range of different techniques have been proposed to specifically tackle the difficulties of sampling phase space in complex systems. A histogram reweighting technique [217, 218] where results of multiple MC simulations could be combined to increase the total accuracy. Parallel tempering or replica exchange [219, 220] methods, where large number of replicas, with for example different temperatures, are considered simultaneously and the replicas are changed among each other. The thermodynamic quantities for intermediate temperatures can be calculated by histogram reweighting [217, 218] (Hamiltonian replica exchange method will be considered in the next chapter.) These techniques still rely on conventional canonical sampling of the phase space.

Another class of techniques are flat-histogram or uniform sampling methodologies, where the system under study is sampled with a non-Boltzmann weight (often referred as Multicanonical (MUCA) weights or more generally non-Boltzmann sampling (NBS)), such that uniform sampling in respect to a chosen order parameter is achieved [221]. The main problem here is in choosing these sampling probabilities. The original work on the MUCA method [222] and a follow up on entropic sampling [223], showed that the distribution yielding flat energy histogram can be constructed iteratively. Recently published Wang-Landau (WL) sampling method (also known as density-of-states MC) [224] showed how the density of states estimate can be dynamically updated during the simulation, leading to uniform sampling of the energy space. Originally, WL-sampling was tested on a 2D-Ising model [224]. It has been generalised for continuum systems with continuous potential energy as well as for isobaric-isothermal (NPT) and grand canonical (μVT) ensembles [225, 226], where the vapour-liquid coexistence of Lennard-Jones system was studied. Later it was successfully applied to the glass transition in binary Lennard-Jones system [227], protein folding in vacuo and implicit solvent [228, 229], helical polymers [230] and complex liquids including the isotropic-nematic phase transition of Gay-Berne mesogens by sampling density space at fixed temperature [231].

Despite these success stories, problems still exist for the simulation of continuous and large systems and some non-trivial modifications are needed [232–236]. In their studies of the isotropic-nematic phase transition of the Lebwohl-Lasher liquid crystal model, Jaysri *et al.* [233] discovered a critical slowing down of dynamics with 216 or more spins, non-trivial modifications were needed to overcome this barrier.

Another obstacle for using WL-sampling for simulation of complex system, where no effective MC moves are present, is that it is based only upon MC. To overcome these problems a new methodology, Statistical Temperature Molecular Dynamics (STMD), was recently proposed [76]. It relies on the connection between the statistical temperature and density of states, $1/k_BT = (\partial \ln \Omega / \partial E)_{N,V}$, effectively combining multicanonical MD [237, 238] and WL-sampling as will be shown in next section. STMD has been successfully applied to the Ising model, a Lennard-Jones liquid, and to biomolecules [76, 239–241].

Next section, 6.2, introduces the theory behind the STMD method. The connection between WL-sampling and multicanonical MD will be discussed and a practical simulation approach will be presented. Results for STMD simulations of single-site system and model diblock copolymer melt will be presented in sections 6.3.1 and 6.3.2, respectively.

6.2 Theory

6.2.1 Statistical Temperature Molecular Dynamics algorithm

6.2.1.1 Wang-Landau sampling

Considering the density of states $\Omega\left(N, V, E\right)$, for a number of particles N, volume V and energy E, the microcanonical probability of a state (s) occurring is [37]

$$P_{\mathrm{s}} = \frac{1}{\Omega\left(N_{\mathrm{s}}, V_{\mathrm{s}}, E_{\mathrm{s}}\right)}. \tag{6.1}$$

Now considering two energy states of discrete energy space, E_1 and E_2, generated in a MC simulation, the detailed balance criteria can be written

$$\frac{1}{\Omega\left(N, V, E_1\right)} p(E_1 \rightarrow E_2) = \frac{1}{\Omega\left(N, V, E_2\right)} p(E_2 \rightarrow E_1), \tag{6.2}$$

where $p(E_1 \rightarrow E_2)$ is transition probability from state E_1 to state E_2. The acceptance criteria for the transition can now be written [224]

$$p(E_1 \rightarrow E_2) = \min\left[\frac{\Omega\left(N, V, E_1\right)}{\Omega\left(N, V, E_2\right)}, 1\right]. \tag{6.3}$$

At the beginning of a random walk the density of states $\Omega\left(N, V, E\right)$ is unknown. The idea behind WL-sampling [224] is to represent the density of states as a histogram, $\Omega(E)$. Initially the density of states, $\Omega(E)$, for all energies, E, is set to $\Omega(E) = 1$. Then a random walk is conducted using acceptance criteria of equation (6.3) to move between states. At each visit to a particular energy E, the density of states estimate is updated as

$$\Omega(E) = \Omega(E) \times f, \tag{6.4}$$

where f is a modification factor with constraint, $f > 1$, and the energy histogram, $H(E)$, is accumulated. The random walk is continued, with constant f, until the energy histogram, $H(E)$, is sufficiently flat. Then the modification factor, f, is reduced and the energy histogram is set to zero. The simulation can be stopped when the modification factor f has become sufficiently close to unity. In the original implementation of the method the choice for the initial modification factor, f_0, reduction function and stopping criteria, f_{final}, were $f_0 = e^1 \approx 2.718$, $f_{i+1} = \sqrt{f_i}$ and $f_{\text{final}} = \exp(10^{-8})$ [224].

Due to the dynamic updates for density of states the detailed balance condition, equation (6.2), is satisfied only within an accuracy proportional to $\ln(f)$. Every time when the flat energy histogram, $H(E)$, is recovered the density of states estimate, $\Omega(E)$, is converged to its true value within accuracy of $\ln(f)$.

6.2.1.2 Generalised ensemble MD

Considering a separable probability distribution for the momentum, $\mathbf{p}$ and position, $\mathbf{q}$, the probability distribution for the reference temperature, $k_B T_0 = 1/\beta_0$, takes the form [242]

$$P(\mathbf{p}, \mathbf{q}) = A(\mathbf{p})B(\mathbf{q}) \propto \exp[-\beta_0 K_{\text{eff}} - \beta_0 V_{\text{eff}}]. \tag{6.5}$$

This leads to an effective Hamiltonian

$$H_{\text{eff}} = K_{\text{eff}} + V_{\text{eff}}, \tag{6.6}$$

where the effective kinetic energy, K_{eff}, and the effective potential energy, V_{eff}, can be given within a constant by

$$K_{\text{eff}}(\mathbf{p}) = -\frac{1}{\beta_0}\ln A(\mathbf{p}),\ V_{\text{eff}}(\mathbf{q}) = -\frac{1}{\beta_0}\ln B(\mathbf{q}). \tag{6.7}$$

Barth *et al.* [242] showed how these generalised distributions can be realised in molecular dynamics simulations using the Nosé-Hoover (and Nosé-Poincaré) formalism. In the special case where K_{eff} takes the standard form for the canonical distribution, the only difference to the standard Nosé-Hoover formalism is in the derivation of the forces from $V_{\text{eff}}(\mathbf{q})$ [242]

$$\tilde{\mathbf{f}} = -\nabla_{\mathbf{q}} V_{\text{eff}}(\mathbf{q}). \tag{6.8}$$

In the multicanonical ensemble [237, 238] the momenta distribution is the same as in the canonical, const-NVT, ensemble. The configurational distribution takes the form [237, 238]

$$P_{\text{MUCA}}(U[\mathbf{q}]) = e^{-S(U[\mathbf{q}])/k_B}, \tag{6.9}$$

where S is the entropy of the state with potential energy U and $U[\mathbf{q}]$ is a continuous potential energy. This leads to an effective potential of

$$V_{\text{eff}}(\mathbf{q}) = \frac{1}{k_B\beta_0} S(U[\mathbf{q}]). \tag{6.10}$$

Now the forces can be solved

$$\begin{aligned} \tilde{\mathbf{f}} &= -\frac{\partial V_{\text{eff}}(\mathbf{p})}{\partial \mathbf{q}} = -\frac{1}{k_B\beta_0}\frac{\partial S(U[\mathbf{q}])}{\partial \mathbf{q}} \\ &= -\frac{1}{k_B\beta_0}\frac{\partial S(U)}{\partial U}\frac{\partial U[\mathbf{q}]}{\partial \mathbf{q}}, \end{aligned} \tag{6.11}$$

where $-\partial U[\mathbf{q}]/\partial \mathbf{q}$ is a normal force term which is rescaled by the derivative of the entropy. Substituting $1/\beta_0 = k_B T_0$ into equation (6.11), the sampling of configurations according to the weight $\mathrm{e}^{-S(U)}$, can now be realised in molecular dynamics simulation with Nosé-Hoover thermostat by maintaining the kinetic energy at the reference temperature T_0 and scaling the forces with the energy dependant term

$$\mu(U) \equiv T_0 \frac{\partial S(U)}{\partial U}. \tag{6.12}$$

6.2.1.3 Dynamic update scheme for the statistical temperature estimate

The idea behind STMD [76] is to combine WL-sampling with multicanonical MD such a way that the weights, $\mu(U) = T_0 \frac{\partial S(U)}{\partial U}$, needed to integrate the equations of motion can be constructed dynamically. For a constant number of particles, N, and volume, V, the statistical temperature (taking $k_\mathrm{B} = 1$) is defined as [37]

$$\beta(U) = \frac{1}{T(U)} = \frac{\partial S(U)}{\partial U}, \tag{6.13}$$

with the relation between the entropy, $S(U)$ and density of states, $\Omega(U)$

$$S(U) = \ln\left[\Omega(U)\right]. \tag{6.14}$$

Now considering an equally spaced energy grid, $U_j = \mathrm{int}[U/\Delta U]\Delta U$, substituting equation (6.14) into the WL-update scheme (6.4) one arrives at an update scheme for the entropy [76]

$$S_j \rightarrow S_j + \ln f. \tag{6.15}$$

A dynamic update scheme for the inverse temperature can be realised by approximating equation (6.13) with the central difference [76]

$$\beta_j = \frac{1}{T_j} \approx (S_{j+1} - S_{j-1})/2\Delta U \tag{6.16}$$

and using the update scheme for the entropy (6.15). Substituting $j \rightarrow j+1$ in to equation (6.16) and using (6.15)

$$\beta_{j+1} = \frac{S_{j+2} - S_j}{2\Delta U} = \frac{S_{j+2} - S_j - \ln f}{2\Delta U} = \beta_{j+1} - \delta f, \tag{6.17}$$

where $\delta f = \ln f/2\Delta U$, and similarly for $j-1$, a general update scheme for the inverse temperature is recovered [76]

$$\beta_{j\pm 1} = \beta_{j\pm 1} \mp \delta f. \tag{6.18}$$

Writing this in terms of temperature [76]

$$T_{j\pm 1} = \alpha_{j\pm 1} T_{j\pm 1}, \tag{6.19}$$

with

$$\alpha_{j\pm 1} = \frac{1}{1 \mp \delta f T_{j\pm 1}}. \tag{6.20}$$

This operation defines the statistical temperature, $T(U)$, at the discrete grid points U_j. However, the energy dependent force scaling factor (6.12) requires a continuous description of $T(U)$. In the original work [76] two different interpolation schemes between the grid points were discussed: staircase interpolation and linear interpolation. In the linear temperature estimate the successive grid points are connected linearly. For potential energy $U \in [U_j, U_{j+1}]$ the temperature estimate $T(U)$ becomes

$$T(U) = T_j + \lambda_j (U - U_j), \tag{6.21}$$

where the slope connecting $[U_j, T_j]$ and $[U_{j+i}, T_{j+1}]$ is

$$\lambda_j = \frac{(T_{j+1} - T_j)}{\Delta U}. \tag{6.22}$$

Now the multicanonical scaling factor (6.12) combined with dynamic estimate of the temperature (6.20) yields the statistical temperature molecular dynamics (STMD), with forces scaled with energy dependent term as [76]

$$\tilde{\mathbf{f}}_i = \mu(U)\mathbf{f}_i = T_0 \frac{\partial S(U)}{\partial U} \mathbf{f}_i = \frac{T_0}{T(U)} \mathbf{f}_i, \tag{6.23}$$

where the $\mathbf{f}_i$ is the unscaled force on particle i derived from the pair potential as in usual MD.

6.2.2 Integrating the entropy estimate and calculation of ensemble averages

Given the canonical probability distribution function is known, a canonical ensemble average for observable A can be calculated as a weighted average

$$\langle A(T)\rangle = \sum_j \frac{\Omega(U_j)e^{-U_j/k_\mathrm{B}T}}{\sum_j \Omega(U_j)e^{-U_j/k_\mathrm{B}T}}A(U_j) = \sum_j \frac{e^{S(U_j)-U_j/k_\mathrm{B}T}}{\sum_j e^{S(U_j)-U_j/k_\mathrm{B}T}}A(U_j). \tag{6.24}$$

When the simulation has converged, the temperature estimate with smoothing (6.21) can be integrated to give a continuum estimate of the entropy $S(U)$. Applying analytic integration [76]

$$\begin{aligned} S(U) &= \int_{U_l}^{U} \beta(U^{'})dU^{'} = \int_{U_l}^{U} \frac{1}{T_j + \lambda_j\left(U' - U_j\right)}dU^{'} \\ &= \sum_{j=l+1}^{i^*} \frac{\ln\left[1+\lambda_{j-1}\left(U_j - U_{j-1}\right)/T_{j-1}\right]}{T_{j-1}} + \frac{\ln\left[1+\lambda_i\left(U-U_i\right)/T_i\right]}{T_i}, \end{aligned} \tag{6.25}$$

where the limits of summation are defined by which bin i the energy U belongs, as $i^* = i-1$ for $U \in [(U_{i-1}+U_i)/2, U_i]$ and $i^* = i$ for $U \in [U_i, (U_{i+1}+U_i)/2]$ and U_l is an arbitrarily defined lower integration limit. Now using equation (6.24) the average of observable A can be calculated for the desired temperature T.

In practice using equation (6.24) is problematic due to the huge range of $S(U)$ and U leading to numerical instabilities when trying to calculate exponential terms. To circumvent this, it has been suggested [239] that these problems can be avoided by assuming that the distribution function is a gaussian centred about a fixed point in energy $U^\dagger$, with $T = T(U)$. This is the equivalent of assuming a canonical sampling with temperature T. Then the averaging can be done with modifying the exponents by subtracting the maximum value $F_\mathrm{max} = S(U^\dagger) - \beta U^\dagger$ [239]

$$\langle A(T)\rangle = \sum_j \frac{e^{F(U_j)-F_\mathrm{max}}}{\sum_j e^{F(U_j)-F_\mathrm{max}}}A(U_j). \tag{6.26}$$

6.2.3 Practical simulation approach

The STMD method can be implemented in an existing molecular dynamics program via force scaling, equation (6.12), and linear interpolation, equation (6.20). It might be useful to note, that the potential energy, U, considered is the total potential energy of the system *i.e.* it includes all the interactions (non-bonded, bond, angle, etc.), so the scaling should be applied after all the different force components are added together. Therefore a natural "place" for implementing the scaling is after all the forces have been calculated and just before the equations of motion are integrated. The running temperature estimate can be achieved by having a histogram representing the statistical temperature $T(U)$ estimate and modifying it with equation (6.20) for bin j corresponding to each visit in the potential energy $\mathrm{int}(U_j/\Delta U)\Delta U$ (int taking the nearest integer), at every MD step.

A practical STMD simulation can be summarised as [239]:

- Determine the desired temperature range with upper and lower bounds T_h, T_l and the reference temperature T_0, normally it is chosen to be $T_0 = T_h$. Choose the energy bin size ΔU and initial modification factor f_0.

- Set the initial temperature estimate $T(U) = T_h$ and zero the energy histogram $H(U) = 0$.

- Perform the STMD simulation by using the temperature, equation (6.20) and force scaling, equation (6.12), and accumulate energy histogram $H(U)$.

- During the initial stage of the simulation a low energy flattening can be applied to the temperature estimate as $T(U) = T_{\min}$ for $U < U_{\min}$ where $U_{\min}$ is the lowest visited energy and $T_{\min} = \min(T(U))$. During the initial stage of the simulation the energy histogram, $H(U)$, is not accumulated.

- The end points of the temperature range can be enforced by restricting the updates of T_j at range $T_g \in [T_l, T_h]$ and setting $T_j = T_l$ and $T_j = T_h$ beyond lower and upper temperature limits T_l and T_h. This is the equivalent of confining the WL-sampling into a desired energy range [243].

- When a flat energy histogram is found, the convergence factor is reduced, $f_{i+1} = \sqrt{f_i}$, and the energy histogram is set to zero, $H(U) = 0$. The simulation is continued from the current temperature estimate $T(U)$. Simulation can be stopped when the modification δf is sufficiently small, for example 10^{-8}.
- After the simulation the thermodynamic properties can be calculated using equation (6.26).

The low energy flattening, applied in the initial stage of the simulation is not compulsory, but it has been seen to speed up the initial sampling speed. For 110 Lennard-Jones particles in the fluid region of the phase diagram, a speed up of approximately 2.5 times was found when comparing to system a without low energy flattening [239]. There is no universal way of determining when the energy histogram $H(U)$ is sufficiently flat. In the original STMD formulation [76, 239], it was taken that $H(U)$ was sufficiently flat when fluctuations were less than 20% from the average value

$$\left| \frac{H(U) - \overline{H(U)}}{\overline{H(U)}} \right| < 0.2, \tag{6.27}$$

where $\overline{H(U)}$ is the average of the histogram $H(U)$.

6.3 Simulations of phase transitions

6.3.1 Simulation of Isotropic-Nematic phase transition

6.3.1.1 Simulation details

The applicability of the STMD method for first order like phase transition was studied for a bulk system consisting $N = 512$ spherocylinders (SCS). The SCS interaction were modelled with equation (3.1) as the model B in chapter 3, using parameters $U^*_{\mathrm{max}} = 25.0$, $U^*_{\mathrm{attr}} = 150.0$, $\epsilon_1 = 12.0$, $\epsilon_2 = 0.0$ and with elongation $L/D = 3.0$. This parametrisation destabilises T and cross configurations relative to the side-by-side and end-to-end configurations and it has been seen exhibit a large nematic region (section 3.4.2 in chapter 3). The simulations were run with a timestep, $\Delta t^* = 0.01$, at reduced number density $\rho^* = N/V^* \approx 0.34$, in which the system in known to have a isotropic-nematic phase transition in the temperature range $T \in [3.5, 4.0]$.

All the simulations were started with initial modification factor, $f_0 = 1.0005$, but four different energy bin sizes, $\Delta U = 16,\ 32,\ 64,\ 128$, were considered. The temperature range was chosen from $T_l = 2.8$ to $T_h = 4.6$ with the reference kinetic temperature maintained at $T_0 = T_h = 4.6$ by applying a Nosé-Hoover thermostat. A linear temperature estimate (6.21) between the grid points was used.

Initially the temperature estimate was set to $T(U) = T_h$ and low energy flattening, $T(U) = T_{\min}$ for $U < U_{\min}$, was applied every 10^5 MD steps, until $T_{\min}$ reached T_l. After $T_{\min}$ had reached T_l the flatness of the energy histogram $H(U)$ was checked (6.27) every 10^5 MD steps. When a flat energy histogram was recovered the modification factor was reduced $f_{i+1} = \sqrt{f_i}$ and simulation was continued with the current running estimate of $T(U)$. Simulations were terminated when the modification factor reached $\log(f) < 10^{-8}$.

6.3.1.2 Results

In figure 6.1, the evolution of the statistical temperature estimate $T(U)$ for the SCS system studied is presented for the simulation with energy bin size $\Delta U = 64$. It takes approximately 2.5 million MD steps for the system to reach T_l which is then followed by a fairly uniform sampling of the temperature range. On the bottom part of figure 6.1, the evolution of the total potential energy U^* for the system is presented. From this it can be seen that a large energy range of approximately $U^* \in [-500, 3000]$ was sampled uniformly during the STMD simulation. Comparing both top and bottom parts of the figure 6.1, connection between the temperature and the potential energy can be observed. The low temperature regions (top) correspond to the low energy regions (bottom) and similarly for high temperature and energy regions, giving a mapping of (T, U) phase space.

The simulations were considered as being converged when the modification factor had become sufficiently small, i.e. $f_d = f - 1 = 10^{-8}$ [76]. The converged temperature estimates $T(U)$ for the systems with energy bin sizes $\Delta U = 16,\ 32,\ 64,\ 128$ are presented in figure 6.2. They are indistinguishable apart from a small rugged-

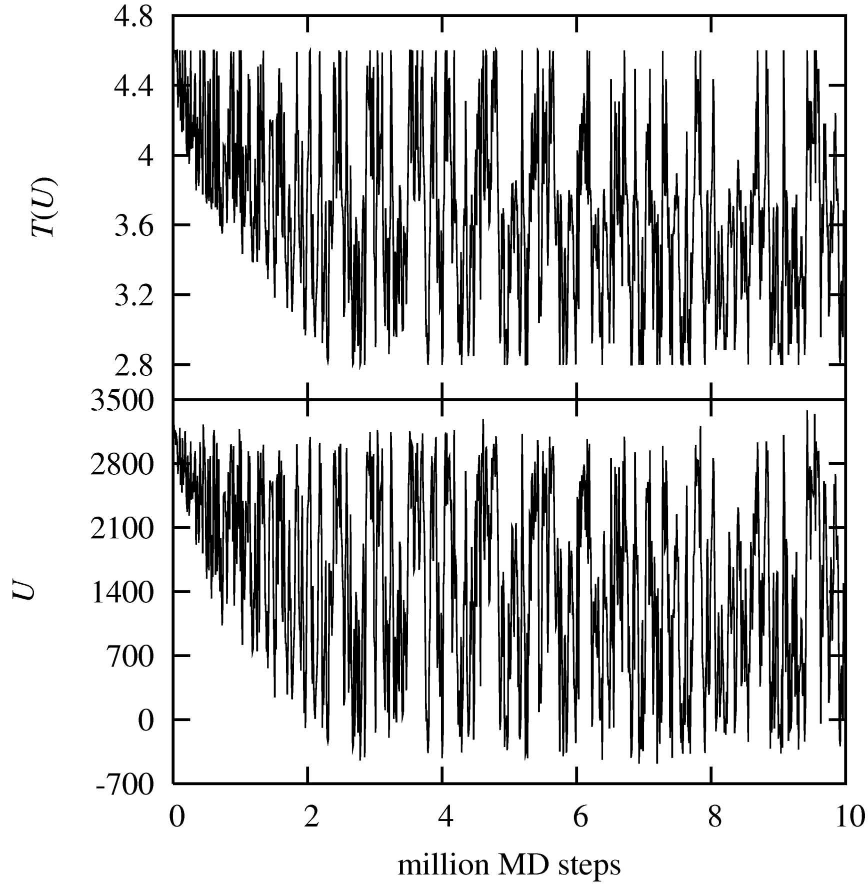

Figure 6.1: (top) The evolution of the temperature estimate, $T(U^*)$, (bottom) the evolution of the reduced potential energy U^* as a function of MD steps for 512 spherocylinders system with energy bin size $\Delta U = 64$.

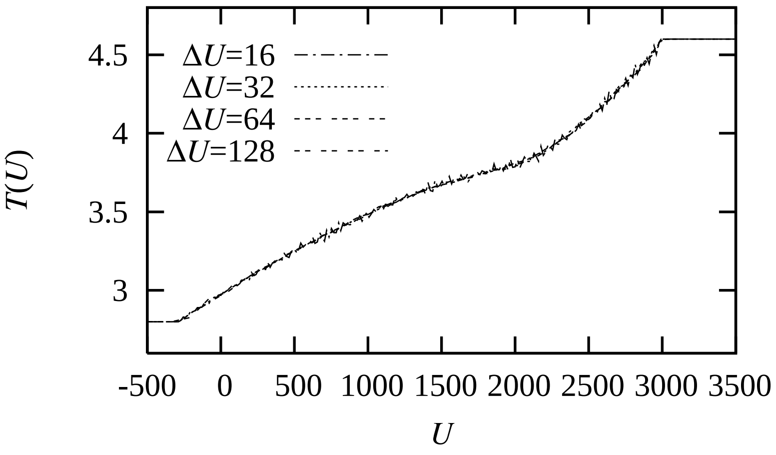

Figure 6.2: Convergent temperature estimate $T(U)$ for 512 SCS systems as a function of the potential energy U for systems with energy bin size, $\Delta U = 16, 32, 64, 128$.

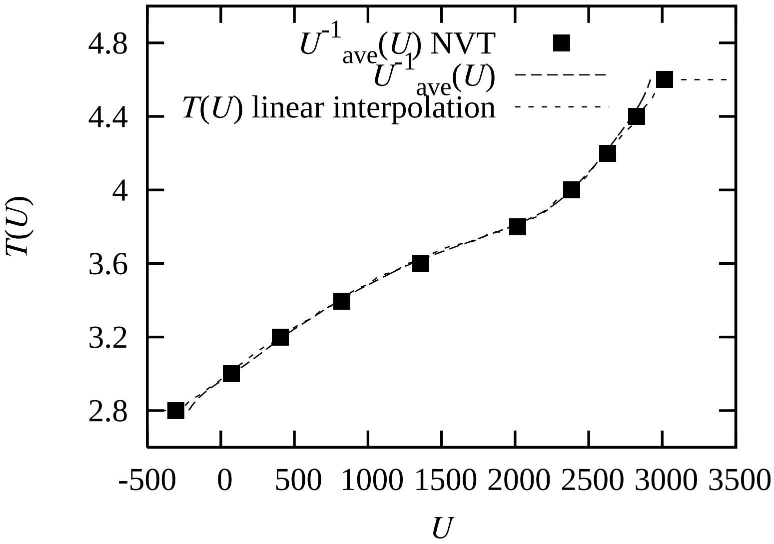

Figure 6.3: The temperature estimate $T(U)$, the inverse of reweighted average energy $U^{-1}_{\text{ave}}(U)$ and inverse average energy from NVT simulations (squares) as a function of potential energy U. The STMD simulation results are from the system with energy bin size $\Delta U = 32$. The NVT results are from simulations of 1000 SCS and are weighted as, $U_{512} = (512/1000) \times U_{1000}$ to give correspondence to the system of 512 SCS used in the STMD simulations.

ness for the estimate using the smallest energy bin size $\Delta U = 16$. There can be observed a change in curvature in the energy region $U^* \in [1000, 2000]$ corresponding to temperatures $T \in [3.5, 4.0]$ suggesting a phase transition.

The convergent temperature estimate can be integrated, equation (6.25), to give an entropy estimate $S(U)$, which can then be used to construct the weights needed to calculate canonical ensemble averages using equation (6.24) or (6.26). The average reweighted potential energy $U_{\text{ave}}(T)$ was calculated using equation (6.26). It can be compared to the statistical temperature estimate through the relation $T(U) \equiv U^{-1}_{\text{ave}}(U)$. In figure (6.3) the temperature estimate $T(U)$ generated in STMD simulations with $\Delta U = 32$, inverse reweighted average energy $U^{-1}_{\text{ave}}(U)$ and inverse average energy from NVT simulations are compared. It can be observed that the results from STMD simulations agree very well with those from conventional canonical simulations including the end points. The inverse reweighted average energy $U^{-1}_{\text{ave}}(U)$ shows small deviations at low and high energy ends.

The reweighting (6.26) can be also applied to structural quantities or snapshots as long as their distribution as a function of energy is known for the desired en-

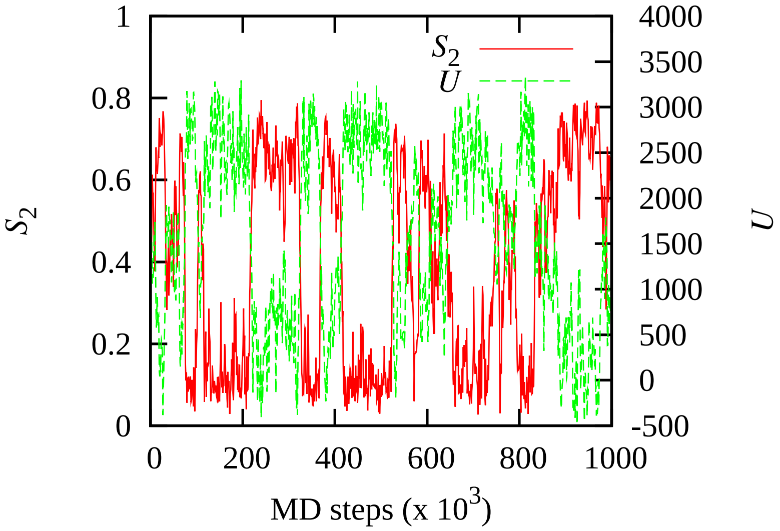

Figure 6.4: The evolution of orientational order parameter $S_2 = \langle P_2 \cos(\hat{\mathbf{e}}_i, \mathbf{n}) \rangle$ and potential energy U as a function of MD steps for a system with $\Delta U = 32$ and $f_d = 10^{-7}$.

ergy range. To generate data points, a production run of 1 million MD steps was performed for the system with $\Delta U = 32$ using the converged temperature estimate $T(U)$ with modification factor $f_d = f - 1 = 10^{-7}$. The configurations were written to disk every 1000 steps.

The evolution of the orientational order parameter, S_2, and the potential energy, U, from the production run is presented in figure 6.4. From this, it can be observed how the system samples both the isotropic phase with higher potential energy U and vanishing orientational order, $S_2 \approx 0$, and the nematic region with lower potential energy and non-zero orientational order parameter $S_2 \neq 0$. It is also apparent how the system changes continuously between these two regions, leading to uniform sampling of the potential energy space.

The ensemble average of the orientational order parameter $\langle S_2(T) \rangle$ was calculated by reweighting (6.26) from the configurations generated in the production run. The results for $\langle S_2(T) \rangle$ and average potential energy $U_{\text{ave}}(T)$ from the STMD simulations are compared to the results from conventional canonical simulation in figure 6.5. There can be seen that a change in curvature of the potential energy curve, $U_{\text{ave}}(T)$, occurs approximately at the temperature range $T \approx 3.75 \ldots 3.6$, and on the same temperature range the orientational order parameter grows from $\langle S_2 \rangle \approx 0.15$ to

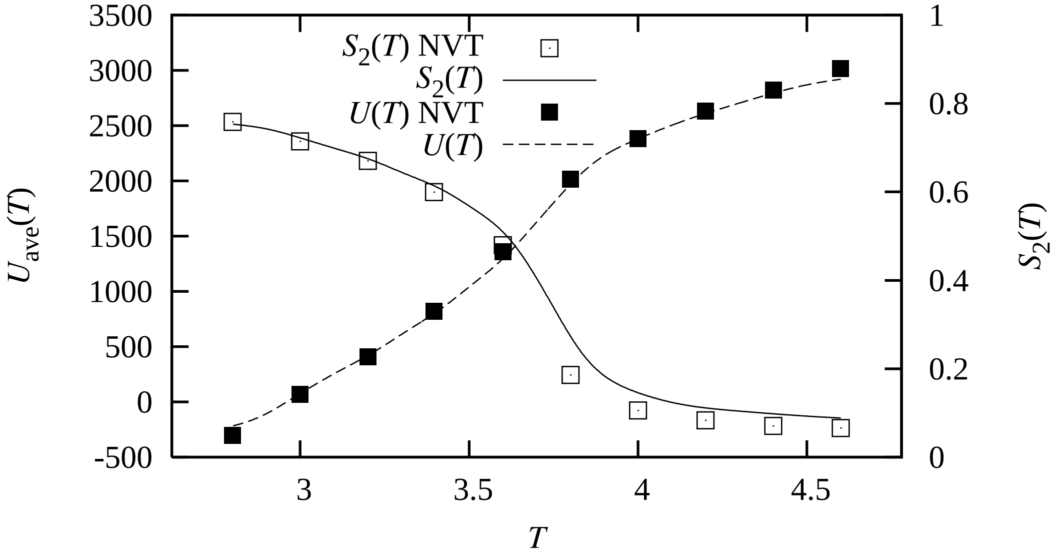

Figure 6.5: The ensemble average for potential energy U and orientational order parameter, $S_2 = \langle P_2 \cos(\hat{\mathbf{e}}_i, \mathbf{n})\rangle$, from STMD simulations with $\Delta U = 32$ and $f_d = 10^{-7}$ compared to results obtained for conventional NVT simulations of 1000 SCS (the energy weighted as $U_{512} = (512/1000) \times U_{1000}$).

$\langle S_2 \rangle \approx 0.6$ signalling a phase transition from an orientationally disordered isotropic liquid to a uniaxial nematic phase. Comparing the results from the conventional canonical simulation, both the reweighted energy $U_{\text{ave}}(T)$ and the orientational order parameter $\langle S_2(T)\rangle$ are in very good agreement, including the isotropic nematic phase transition point.

The thermodynamics quantities such as the entropy, $S(T)$, and free energy, $F(T)$, as a function of the temperature, T, are available through the construction of the statistical temperature, equation (6.13) and reweighting, equation (6.26). Entropy as a function of potential energy is known from the integration of the statistical temperature estimate and linear interpolation, equation (6.25). $S(T)$ can then be calculated by reweighting. The free energy, $F(T)$, can be calculated using the reweighted values for the entropy $S(T)$ and internal energy $U(T) \equiv U_{\text{ave}}(T)$ for desired temperatures T as $F(T) = U(T) - TS(T)$ [37]. The heat capacity of the system can be calculated from the energy fluctuations as [37] $C_{UU}(T) = \frac{\langle(\delta U)^2\rangle}{T^2} = \frac{\langle U^2\rangle - \langle U\rangle^2}{T^2}$, where reweighted averages $\langle U\rangle_T = U_{\text{ave}}(T)$ are used.

Entropy $S(T)$, free energy $F(T)$ and heat capacity, C_{UU}, are presented in figure 6.6 for the temperature range $T \in [2.8, 4.6]$. The heat capacity can be observed

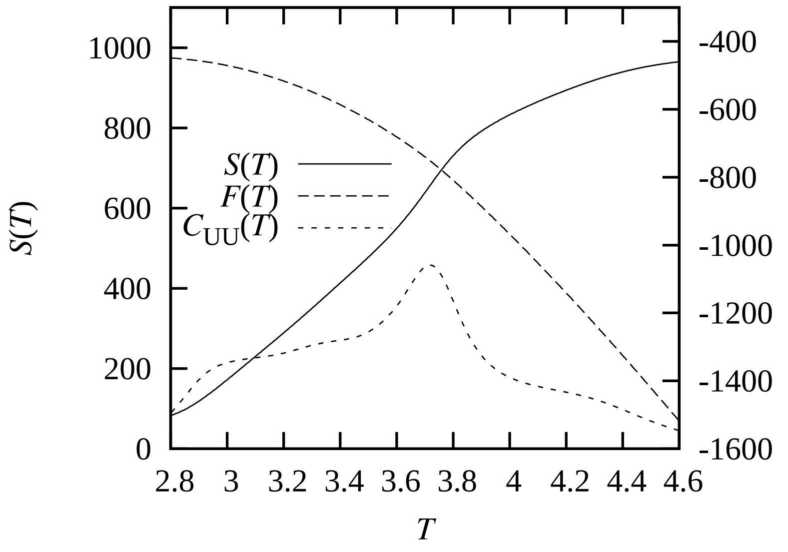

Figure 6.6: Entropy $S(T)$ (left axis), free energy $F(T)$ (right axis) and heat capacity C_{UU} (no units) calculated from STMD simulations with $\Delta U = 32$.

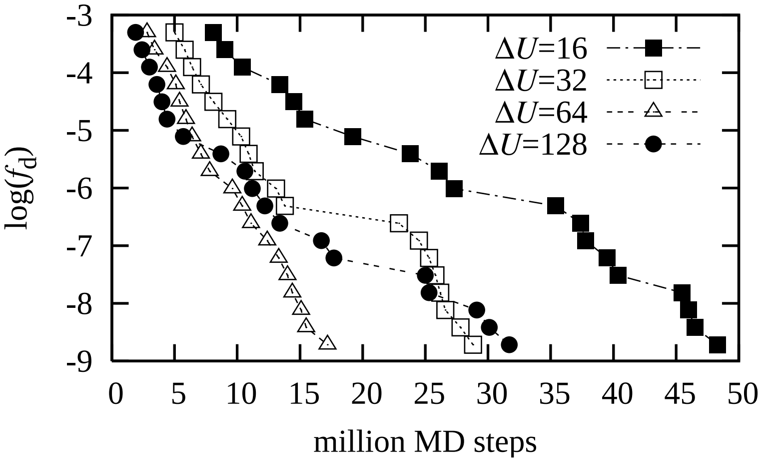

Figure 6.7: Convergence of the STMD simulations: The logarithm of the modification factor $\log(f_d)$, $f_d = f - 1$, against MD steps for the systems with potential energy bin width $\Delta U =$ 16, 32, 64, 128.

to have a peak at $T \approx 3.72$ marking the phase transition between isotropic and nematic phases. The entropy curve shows a change in curvature at the same point, being consistent with the expectations in a first order-like phase transition for a finite size system. It must be noted that for infinitely large systems at a first order phase transition the heat capacity, C_{UU}, would go to infinity and the entropy, $S(T)$, would have a discontinuity. These changes are damped through effects of the fairly small system size ($N = 512$). Despite the finite size effects the expected behaviour for entropy, free energy and heat capacity is recovered.

For understanding the effects of the energy bin size, ΔU, for the convergence times, the evolution of the modification factor, f, was analysed for each of the systems with the energy bin sizes $\Delta U =$ 16, 32, 64, 128. It is useful to note that the CPU time for each MD step is independent of the choice of ΔU. In figure 6.7, the logarithm of the modification factor f_d (remembering $f_d = f - 1$) is plotted against MD steps for the systems with bin sizes $\Delta U =$ 16, 32, 64, 128. A speed up can be seen in convergence of approximately 1.7 times and 2.8 times moving from $\Delta U = 16$ to $\Delta U = 32$ and to $\Delta U = 64$ respectively. This behaviour is similar to the findings for a 110 particle Lennard-Jones system in the liquid region [239]. Interestingly, the system with the largest energy bin size $\Delta U = 128$ shows initially only a fractionate speed up compared to $\Delta U = 64$ and then the convergence slows down finishing equal to the $\Delta U = 32$ system. This result implies that there exists a critical energy bin size, after which the sampling speed will slow down. This can be partly understood through the modification of the statistical temperature estimate, equation (6.20), where the modification factor used is $\delta f = \ln(f)/2\Delta U$. The use of a very large bin size also increases the individuals length of the linear interpolations between grid points. This can also affect the convergence times. It must be noted that all the converged temperature estimates, figure (6.2), were very similar, so no obvious effect of the energy bin size, ΔU, on the accuracy of the temperature estimate, $T(U)$, was seen.

6.3.2 Simulation of the isotropic-lamellar phase transition of model diblock copolymer

6.3.2.1 Simulation details

The isotropic-lamellar phase transition of a model soft-core diblock copolymer system of $N = 512$ polymers was studied using the STMD method. An individual polymer was constructed by tethering a chain of 5 spheres (sp) onto a spherocylinder (SCS) resulting to total number of interaction sites as 3072. The SCS pair interaction, equation (3.1), was modelled with parameters $U^*_{\text{max}} = 100.0$, $U^*_{\text{attr}} = 1200.0$, $\epsilon_1 = 60.0$ and $\epsilon_2 = -60.0$ and taking the spherocylinder elongation $L/D = 4$ with $D = \sigma_0 = \sigma_{\text{sp}}$. The SCS-sp and sp-sp interactions where modelled with purely repulsive potential, setting $\epsilon^* = 0$ in equation (3.1), and using $U^*_{\text{max}} = 100.0$. Harmonic bond and bond angle potentials (equations (3.23) and (3.24)) were used for intramolecular interactions between consecutive particles with equilibrium bond length and angle $l_0/\sigma = 1$ and $\theta_0 = 0.0$, with force constants $k_{\text{bond}} = 50.0/(\epsilon_0 \ \sigma_0^{-2})$ and $k_{\text{angle}} = 2.5/(\epsilon_0 \ \text{rad}^{-2})$ for bonds and angles respectively.

The simulations were run with an initial modification factor $f = 1.0005$ and energy bin sizes $\Delta U = 64, \ 128, \ 256$ over the temperature range $T_l = 2.0$ to $T_h = 3.0$ with the reference temperature set to $T_0 = T_h = 3.0$. A time step of $\delta t = 0.01$ was used and the system was kept at a reference temperature by using a Nosé-Hoover thermostat [81]

6.3.2.2 Results

The simulations were run for 240, 223 and 194 million MD steps and flat energy histogram (using the criteria of equation (6.27)) were found 8, 6 and 7 times for the systems with $\Delta U = 64, \ 128$ and $\Delta U = 256$, respectively. In figure 6.8 the generated statistical temperature (or microcanonical temperature), $T(U)$, and averaged potential energy as function of temperature, $U_{\text{ave}}(T)$, is presented for all the systems and compared to conventional NVT simulations. All the system are in very good agreement with each other and the NVT simulations on both sides of the phase transition. However, in the phase transition region, $T \in [2.5, 2.3]$, the temperature

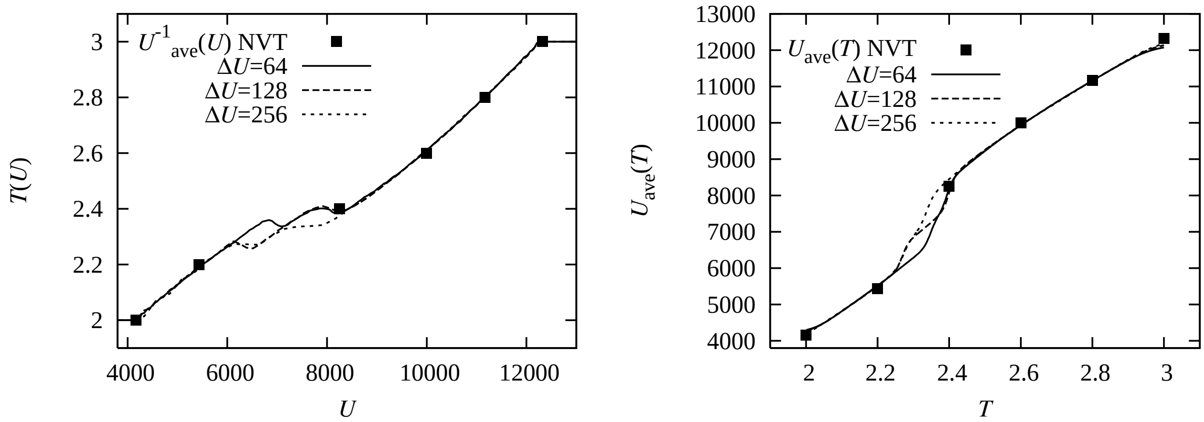

Figure 6.8: Generated temperature estimate, $T(U)$, (left) and calculated average potential energy, $U_{\text{ave}}(T)$, (right) compared to normal canonical MD for the three systems considered $\Delta U = 64,\ 128,\ 256$.

estimates and calculated averages differ from each other. Typically, in finite size systems, the microcanonical temperature would exhibit a back bending behaviour (Van der Waals loop) at a first order-like phase transition [244–248]. Evidence of this can be seen from the $T(U)$ curves (left panel in figure 6.8). The curves seem to show two of, instead of one, back bending regions, suggesting two phase transitions or two separate processes in the phase transition region. Similarly the heat capacity (left panel figure 6.9) shows the peak splitting into two peaks. This behaviour was unexpected. It could be due to poor sampling in the phase transition region. In this system the free energy barrier between the two phases is relatively high, leading to the system preferentially sampling one of the two phases and only occasionally bridging through the phase transition. This is highlighted in the temperature trajectory (right panel in figure 6.9) for the system with $\Delta U = 64$. From this, it can be seen how the system samples states above and below the approximate phase transition temperature, $T \approx 2.4$, but only bridges through the phase transition region approximately 17 times during the 240 million MD step simulation run.

To try to enhance the sampling of the phase transition region, two more simulations were performed, for the systems with $\Delta U = 64$ at the temperature windows of $T \in [2.3, 2.5]$ and $T \in [2.25, 2.45]$. The flat energy histogram was found 10 and 7 times within 85 million and 153 million MD steps, for the systems with $T \in [2.3, 2.5]$ and $T \in [2.25, 2.45]$, respectively. The $T(U)$ curve for the $T \in [2.3, 2.5]$ shows only

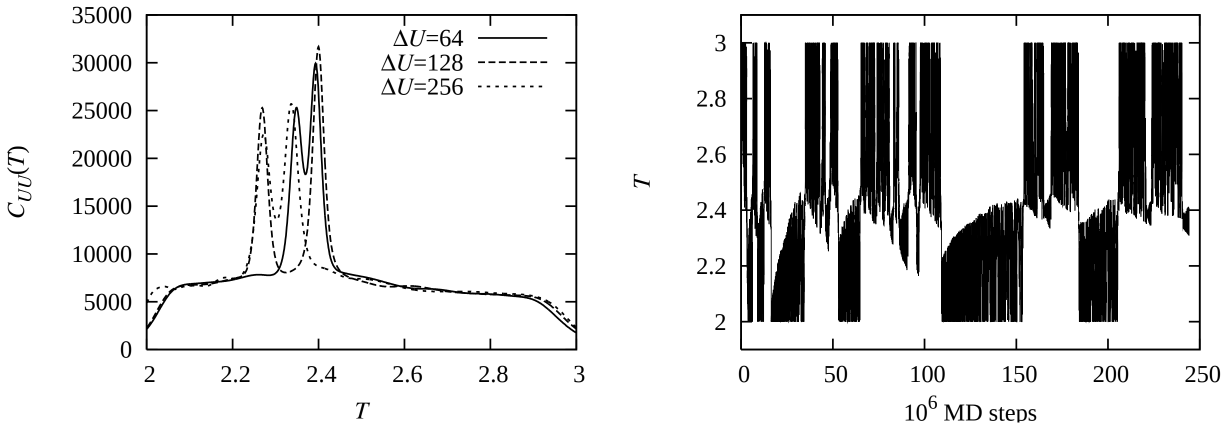

Figure 6.9: Heat capacity, $C_{UU}(T)$, for the three systems with $\Delta U = 64,\ 128,\ 256$ (left) and an example of the temperature trajectory, for the system with $\Delta U = 64$ as a function of the number of molecular dynamics steps (right).

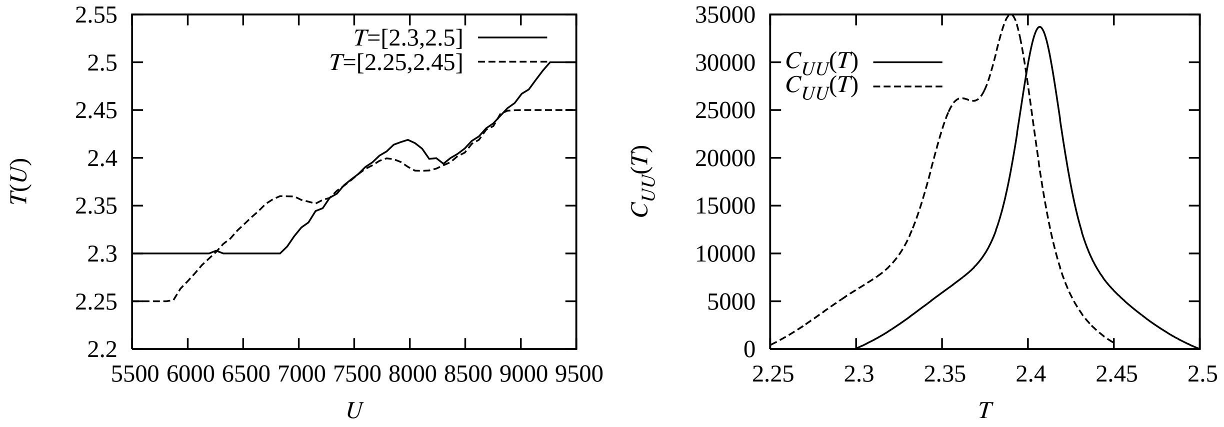

Figure 6.10: Temperature estimate (left) and heat capacity (right) for two systems with short temperature ranges of $T \in [2.3, 2.5]$ and $T \in [2.25, 2.45]$ bridging the isotropic lamellar phase transition, with $\Delta U = 64$.

one back bending region, while the system in $T \in [2.25, 2.45]$ shows two (left panel in figure 6.10). The heat capacity (right panel in figure 6.10) tells a similar story, with the system in $T \in [2.3, 2.5]$ showing only one peak at approximately $T \approx 2.407$ and the system in $T \in [2.25, 2.45]$ showing two clear peaks at temperatures approximately $T \approx 2.390$ and $T \approx 2.361$. The slight difference between the location of the first peak between the two systems is not understood.

The two back bending regions in the $T(U)$ are separated by a linear decrease of the microcanonical temperature. This strongly suggests the presence of two independent first order-like phase transitions. This is quite surprising. One could speculate that the higher temperature (energy) transition could correspond to a phase separation of the two components (rods and spheres) and the second lower temperature transition would correspond to the orientational ordering of the rods in the lamellar layers. Previous microcanonical studies of melting transitions of Lennard Jones clusters [244,248] and peptide aggregation processes [246] suggests that phase separation would lead to a back bending behaviour of the temperature. Phase coexistence (for example formation of nematic clusters in the nematic isotropic phase transition) within a first order phase transition for finite size systems, would not lead to two back bending regions but would be a part of the same region in microcanonical temperature [245,247]. These would suggest that if the results presented here are indeed accurate, it then would have to correspond to the occurrence of two separate first order-like phase transitions. However, to gain full confidence of this result, further (and longer) simulations need to be performed.

One intriguing possibility would be to use the very recently proposed replica exchange statistical temperature Monte Carlo [248], by the original authors of the STMD method. This reference showed a 4 orders of magnitude increase in bridging through the phase transition region when benchmarked against conventional replica exchange Monte Carlo method for the melting of Lennard-Jones cluster of $N = 55$ particles.

6.4 Conclusions

The recently developed statistical temperature molecular dynamics (STMD) algorithm [76] has been applied to the simulation of the isotropic-nematic and the isotropic-lamellar phase transition of two anisotropic bulk systems; a single site soft-core spherocylinder system and a multi-site rod-coil model diblock copolymer melt. In both cases, STMD was able to successfully bridge the phase transition and achieve a uniform sampling of potential energy space for a very large range of energies: $U \in [-500, 3000]$ and $U \in [4200, 14200]$ for the single-site system and diblock copolymer system respectively. Results for the temperature evolution of the potential energy and the orientational order parameter were compared to conventional const-NVT MD simulations for the single site spherocylinder system and found to be in excellent agreement. Moreover, the thermodynamic quantities such as entropy, free energy and heat capacity were readily available from the STMD simulations.

It should be noted also that STMD can be efficiently implemented in existing parallel molecular dynamics codes, since the force, $\mathbf{f}$ appearing on the right hand side of equation (6.12) is the total force acting on a particle, including all the contributions from the non-bonded and the bonded interactions. Therefore the "natural" place to implement the energy dependent scaling is after all the force terms have been added together and prior of the integration of the equations of motion. In this work, STMD was implemented within a parallel replicated data MD program but it possible also for the algorithm to be used within a domain decomposition molecular dynamics (DD-MD) approach with minor modifications to a typical DD-MD code.

Chapter 7

Hamiltonian replica exchange simulations of soft-core Gay-Berne potential

7.1 Introduction

For liquid crystalline systems, a major simulation cost is associated with taking a simulation through a phase transition to a more ordered phase. Often long simulations are required to first nucleate the more ordered phase and then to grow a uniform domain across a simulation box. The time for this grows with system size and (often) with the complexity of the coarse-grained model used (e.g. several coarse-grained sites joined together). Consequently, even for simplified potential models, such as the Gay-Berne, it would be highly desirable if it was possible to speed up this process.

One simulation method, which has received much attention is replica exchange [249]. In its conventional form of parallel tempering, several simulations are run at different temperatures and "replica exchange Monte Carlo moves" take place to "swap" coordinates between ensembles. The net result (in principle) is improved configurational sampling at each temperature [250]. However, for liquid crystals, parallel tempering to bridge across a phase transition is not a sensible option. The major change in configurational space at the transition means that it is very difficult to bridge temperatures spanning a phase transition, even if the position of the phase transition is known *a priori*.

Another possibility is to use Hamiltonian replica exchange molecular dynamics (HREMD) [77, 78], where the Hamiltonian of the system is varied over the different replicas instead of the temperature. If replicas are chosen in such a way that the free energy landscape is simplified, this can allow a faster sampling of the configurational phase space. Potentially, this can lead to a significant speed up in the equilibration of the lowest unperturbed replica in comparison to conventional simulation. Originally HREMD was applied to proteins dissolved in implicit solvents or vacuum [78]. The results showed that a scaled hydrophobicity led to considerably better sampling efficiency compared to standard replica exchange. It has also been used in simulations of biomolecules in explicit water [251, 252]. Recently HREMD was applied to studies of GTP and 8-Br-GTP molecules using soft-core interactions [253].

In this chapter, a soft core variant of the Gay-Berne potential developed by Dr Roberto Berardi and Prof. Claudio Zannoni in university of Bologna, is introduced and showed that, through the use of Hamiltonian replica exchange, this potential can be used to speed up the process of equilibration of a liquid crystalline phase. Additionally, it is demonstrated that the new soft core potential itself, works effectively as an alternative coarse-grained potential for the study of liquid crystalline systems. The development, implementation and pure melt simulations of the soft-core Gay-Berne potential was carried carried out solely by Prof. Zannoni's research group mainly by Dr Roberto Berardi. The thesis author was responsible to the implementation and simulation of the Hamilton replica exchange method. Vast majority of this work was carried out while thesis author was visiting the University of Bologna and Cineca super computer centre for 4 weeks in autumn 2008 as HPC-Europa fellow.[1]

---

[1] The results of this chapter have been submitted to publication in J. Chem. Phys. as: A soft–core Gay–Berne model for the simulation of liquid crystals by Hamiltonian replica exchange. R. Berardi, C. Zannoni, J. S. Lintuvuori and M. R. Wilson.

7.2 Soft-core Gay-Berne model

The model used in this work in this work is a soft-core variant of the standard Gay-Berne pair potential (section 2.1.1), developed by the Bologna group[2]

$$U^{\mathrm{GBS}} = [1 - f(r_{ij}, \boldsymbol{\omega})]\, U^{\mathrm{GB}}(r_{ij}, \boldsymbol{\omega}) + f(r_{ij}, \boldsymbol{\omega})\, U^{\mathrm{SC}}(r_{ij}, \boldsymbol{\omega}). \tag{7.1}$$

In this context, the label soft-core Gay-Berne (GBS) means that the $U^{\mathrm{GBS}} < 0$ portion of the anisotropic energy surface (corresponding to the centre-centre separation larger than the anisotropic contact distance, $\sigma(\boldsymbol{\omega})$ (equation 2.4), with $\boldsymbol{\omega} \equiv (\hat{\mathbf{r}}_{ij},\ \hat{\mathbf{u}}_i,\ \hat{\mathbf{u}}_j))$ is given by the GB potential U^{GB} (equation 2.3), while the $U^{GBS} \geq 0$ part is replaced with a soft core with linear repulsion with slope $-m$ for all the orientations

$$U^{SC}(r_{ij}, \boldsymbol{\omega}) = m\, [r_{ij} - \sigma(\boldsymbol{\omega})], \tag{7.2}$$

The switching between the Gay-Berne potential and soft core was achieved by employing a switching function $f(r_{ij}, \boldsymbol{\omega})$ of sigmoidal shape

$$f(r_{ij}, \boldsymbol{\omega}) = \exp[k\,(r_{ij} - \sigma(\boldsymbol{\omega}))]/(1 + \exp[k\,(r_{ij} - \sigma(\boldsymbol{\omega}))]). \tag{7.3}$$

The parameter k controls the "steepness" at the inflection point located at the anisotropic contact distance $r_{ij} = \sigma(\boldsymbol{\omega})$. For $k < 0$ the switching function tends asymptotically to 0 for increasing values of r_{ij}, while for $r < \sigma(\boldsymbol{\omega})$ it goes to unity. The forces and torques can evaluated from the derivatives $\mathbf{D}U^{\mathrm{GBS}} = [1-f]\,\mathbf{D}U^{\mathrm{GB}} + f\,\mathbf{D}U^{\mathrm{SC}} + [U^{\mathrm{SC}} - U^{\mathrm{GB}}]\,\mathbf{D}f$, where $\mathbf{D}$ stands for the gradient $\nabla_{\mathbf{r}}$ or the angular momentum $\mathbf{L}_i$ operators, using standard procedure for anisotropic potentials [139].

In figure 7.1 the mixed soft core Gay-Berne potential is plotted for the Gay-Berne parametrisation of $\kappa \equiv \sigma_e/\sigma_s = 3$, $\kappa' \equiv \epsilon_s/\epsilon_e = 5$, $\mu = 1$ and $\nu = 3$ *i.e.* GB(3,5,1,3) [4] with parameters for the soft core, $k = -100.0$ and $m = -70$, for the strength of the switching and for the slope of the repulsion, respectively.

To obtain this generic picture of the effects of softness on the mesogenic properties

---

[2] Dr Roberto Berardi and Prof. Claudio Zannoni. Department of Industrial Chemistry, University of Bologna, Italy.

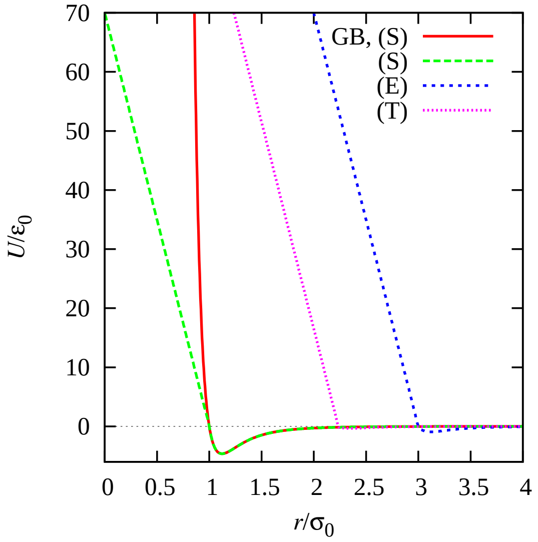

Figure 7.1: Soft core Gay-Berne potential used in this study for three orientations, side-by-side (S), tee configuration (T) and end-to-end (E). A normal Gay-Berne potential for side-by-side orientation is provided for comparison.

of a GB liquid crystal Dr Roberto Berardi performed a preliminary exploration of the phase diagram of the GB(3,5,1,3) model. He used MD simulations in the NVT ensemble with a velocity-Verlet integrator [41, 68] and a weak-coupling Berendsen thermostat [254] to study an $N = 1024$ sample at dimensionless density $\rho^* \equiv N\sigma_0^3/V = 0.3$ [4]. The time–step was $\Delta t^* = (\epsilon_0/\sigma_0^2 m_0)^{1/2}\Delta t = 0.001$, steepness $k = -70\ \sigma_0^{-1}$ and for slope m three different values $m = -30\ \epsilon_0\sigma_0^{-1}$, -40 and $m = -60$ were considered. The results for the orientational order parameter $\langle P_2\rangle$ are given in figure 7.2. From these it can be seen that the steeper soft-repulsive energy barrier, $m = -60\ \epsilon_0\sigma_0^{-1}$, enhances the stability range of ordered phases: the I-N transition shifts to a higher temperature. The soft-core samples also show larger values of the average order parameter, $\langle P_2\rangle$, with respect to the standard GB over the entire temperature range considered. The weaker repulsive barrier, $m = -30\ \epsilon_0\sigma_0^{-1}$, impairs the anisotropy of the GB model: the I-N transition shifts to a lower temperature, and average $\langle P_2\rangle$ values are now systematically lower. Finally, the intermediate barrier, $m = -40\ \epsilon_0\sigma_0^{-1}$, closely follows the phase diagram of the standard GB in the smectic and nematic regions, and deviates only in giving a higher I-N transition temperature.

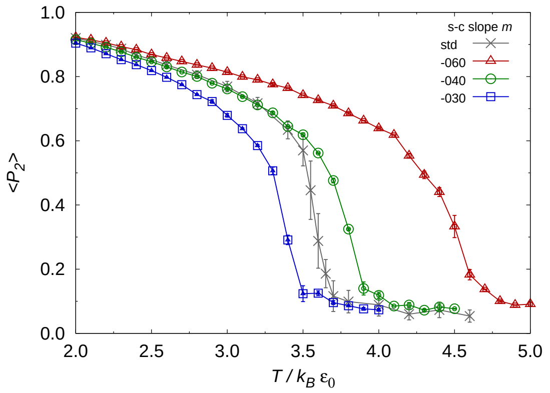

Figure 7.2: The orientational order parameter $\langle P_2 \rangle$ for the soft-core GB potential with logistic function steepness $k = -100\ \sigma_0^{-1}$, and soft-core slopes $m = -60$, -40, and $-30\ \epsilon_0 \sigma_0^{-1}$. The state points are from MD simulations in the NVT ensemble for an $N = 1024$ sample at dimensionless density $\rho^* = 0.3$. The reference points from the NVT simulation of the standard GB(3,5,1,3) model [4] are given by grey points. Figure and Simulations by Dr Roberto Berardi, University of Bologna.

7.3 Hamiltonian replica exchange

The Hamiltonian replica exchange algorithm [77,78] uses several simulations running simultaneously over a range of different Hamiltonians, corresponding to potential energies $U_n(X_n)$ of each independent replica. An attempt to exchange configurations between the different pairs is carried out periodically.

The acceptance probability for the Hamiltonian replica exchange can be realised (See for example refs. [78] and [251]) by considering two replicas with different Hamiltonians $E_n(X_n)$ and $E_m(X_m)$ where X_n and X_m represents the configurational coordinates for the replicas n and m, respectively. The equilibrium probability (Boltzmann distribution) for the nth replica can be written

$$P_n = \frac{1}{Z_n} \exp\left[-\beta E_n(X_n)\right], \tag{7.4}$$

with $\beta \equiv 1/(k_B T)$. Now considering the transition probability, $T(X_n, E_n; X_m, E_m)$ that the configuration X_n in the nth replica exchanges with the configuration X_m in the mth replica, the detailed balance condition can be written

$$P_n(X_n)P_m(X_m)T(X_n, E_n; X_m, E_m) = P_n(X_m)P_m(X_n)T(X_m, E_n; X_n, E_m). \tag{7.5}$$

Substituting (7.4) into (7.5) the ratio of the transition probabilities can be realised

$$\frac{T(X_n, E_n; X_m, E_m)}{T(X_m, E_n; X_n, E_m)} = \exp(-\Delta_{nm}), \tag{7.6}$$

where

$$\Delta_{nm} = \beta \left\{ [E_n(X_m) + E_m(X_n)] - [E_n(X_n) + E_m(X_m)] \right\}. \tag{7.7}$$

This yields a Metropolis-type acceptance criteria for the transition

$$T(X_n, E_n; X_m, E_m) = \begin{cases} 1 & \text{if} \quad \Delta_{nm} \leq 0, \\ \exp(-\Delta_{nm}) & \text{if} \quad \Delta_{nm} > 0. \end{cases} \tag{7.8}$$

7.4 Simulation results

The molecular dynamics (MD) simulations were performed using a parametrisation GB(3,5,1,3) for the Gay-Berne potential and $k = -100.0\ \sigma_0^{-1}$, $m = -70.0\ \epsilon_0\ \sigma_0^{-1}$ for the GBS potential. The system consisted of $N = 1024$ particles in a cubic simulation box at scaled density $\rho^* \equiv N\sigma_0^3/V = 0.3$. The system was simulated in the constant NVT ensemble using velocity rescaling to keep the temperature constant. The scaled temperature was chosen to be $T^* \equiv k_B T/\epsilon_0 = 2.8$. The equation of motions were integrated using the velocity-verlet algorithm with scaled time step of $\Delta t^* = 0.001$. For the GB(3,5,1,3) parametrisation at a given state point the Gay-Berne system is know to be well into the nematic region with an orientational order parameter $\langle P_2 \rangle \approx 0.821 \pm 0.004$ [4]. For the soft core system a slightly higher orientational order parameter $\langle P_2 \rangle \approx 0.850 \pm 0.009$ was observed, which is in agreement with the phase diagram results presented earlier. For the Hamiltonian replica exchange simulations a high temperature isotropic configuration was used as the starting configuration. Two different systems were considered; one with both GB and soft core replicas using the same time step $\Delta t^* = 0.001$ and an other where a timestep of $\Delta t^* = 0.01$ was used for the soft core replica. An attempt to exchange the configurations was carried out every 50, 100 and 500 MD steps using the acceptance criteria of equation (7.8). To obtain an estimate of the average speed-up of the equilibration when using the HREMD in respect to the standard MD, a total of 10 independent HREMD

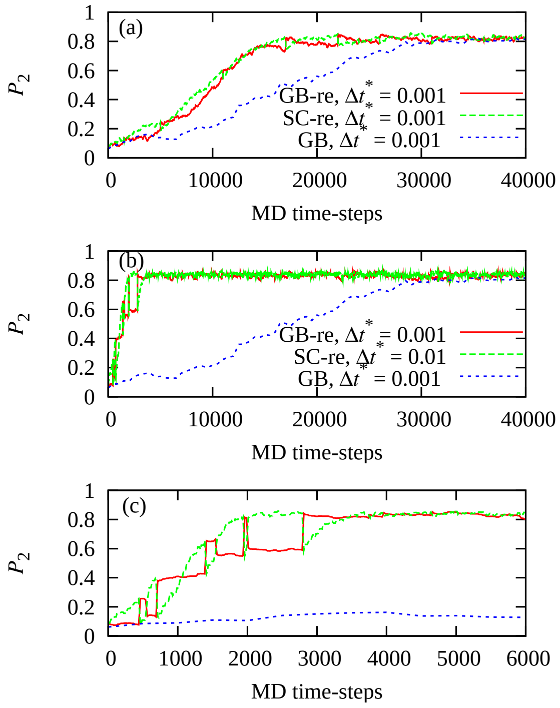

Figure 7.3: The instantaneous order parameter P_2 for the Hamiltonian replica exchange simulations. Bold line GB replica; dashed line GBS replica; dotted line standard GB simulation with $\Delta t^* = 0.001$ (provided for comparison). Plate (a) both GB and GBS replicas are run with same time–step $\Delta t^*_{\mathrm{GBS}} = \Delta t^*_{\mathrm{GB}} = 0.001$; plate (b) GBS replica with time–step $\Delta t^*_{\mathrm{GBS}} = 0.01$, and GB replica with $\Delta t^*_{\mathrm{GB}} = 0.001$; and plate (c) enlargement of the first 6000 MD time–steps from the system with $\Delta t^*_{\mathrm{GBS}} = 0.01$ and $\Delta t^*_{\mathrm{GB}} = 0.001$ of plate (b).

simulations were carried out in each case.

The orientational order parameter, P_2, as a function of MD steps is presented in figure 7.3 over the isotropic nematic phase transition, for the HREMD simulations, Gay-Berne replica (bold line), soft core replica (dashed line) and for normal Gay-Berne system (dotted line), to provide comparison. In the system where both replicas used the same timestep $\Delta t^* = 0.001$, figure 7.3(a), a conservative speed up of approximately 20 % for equilibrating the nematic phase was observed. This is due to the soft-core potential simplifying the underlying free energy landscape, allowing the soft-core replica to sample the relevant phase space more quickly than the normal Gay-Berne potential. This enhances the sampling of the relevant phase space for the Gay-Berne replica through frequent exchanges of the configurations between the two replicas.

To check the advantage of using longer time-step in the integration of the equations of motion for the soft-core potential, additional replica exchange simulations were carried out employing a timestep $\Delta t^*_{GBS} = 0.01$ for the soft-core replica while attempting the exchange of the configurations every $N_{\mathrm{ex}} = 50$ or $N_{\mathrm{ex}} = 100$ MD time-steps. The HREMD simulation results were compared with those for standard GB simulations, where the onset of the nematic phase took place on average (considering ten independent equilibration runs) between 21000 MD time-steps in the best case and 45000 MD time-steps in worst one. In the two H–REMD simulations cases a nematic order was achieved within a range of 3600–7600 and 4000–9600 MD time-steps, leading to speed-up of approximately 2.8–12.5 and 2.2–11.3, for the systems with $N_{\mathrm{ex}} = 50$ and $N_{\mathrm{ex}} = 100$, respectively. (It must be noted that one of the HREMD simulation with $N_{\mathrm{ex}} = 100$ failed to attain a stable nematic organisation within the 10000 MD time–steps window allowed for the experiments.) The average acceptance probabilities for exchanging the replicas were $\langle \Delta^{50}_{\mathrm{GBS-GB}} \rangle \approx 0.212 \pm 0.006$ and $\langle \Delta^{100}_{\mathrm{GBS-GB}} \rangle \approx 0.23 \pm 0.01$.

7.5 Conclusions

The simple soft-core variant of the Gay-Berne potential developed in the university of Bologna and introduced in this chapter, combined with Hamiltonian replica exchange, leads to considerable speeds up in the equilibration of a Gay-Berne system. This is illustrated by a reduced number of molecular dynamics steps required to pass through an isotropic-nematic phase transition. It should also be noted, that the soft-core coarse-grained potential used here can have potential applications in its own right for the study of liquid crystalline systems e.g. as a potential for the simulation of very large systems of mesogens (for example in studying the interaction of a liquid crystal with fields), as a reference nematic solvent (for use with atomistic potentials), or in a multi-site coarse-grained model for use with liquid crystalline macromolecules, similarly to the systems considered in the chapters 3 and 4.

Chapter 8

Conclusions

The main aim of the work presented in this thesis, was to develop and apply novel models and methods to gain improvement in simulation of molecular materials; with a special emphasis on tackling the time scale problem associated with self-organisation of complex systems.

In chapter 3, a new anisotropic soft-core model, based on a spherocylinder, with tunable attractive interactions, was developed. The new model has a number of nice qualities. The attractive interactions can be tuned to favour different configurations between the pairs of particles thus allowing different mesophases to be stabilised. It is, by construction, continuous and goes smoothly to zero, making it usable in molecular dynamics simulations. Moreover, this new model benefits from the possibility of using a timestep, which is approximately an order of magnitude larger than the one required for molecular dynamics simulations of conventional anisotropic models (such as the Gay-Berne potential or the soft repulsive spherocylinder).

Initially, the anisotropic soft-core spherocylinder model, was tested by simulations of two different single site systems, one with particles strongly favouring side-by-side configuration (model A) and the other with T and cross configurations de-stabilised with respect to side-by-side and end-to-end configurations (model B), in the isobaric-isothermal (const-NPT) ensemble. The results demonstrated a rapid equilibration, giving an isotropic and a smectic A phase (model A) and an isotropic, nematic and low temperature smectic phases (model B). The phase behaviour of model B was studied further by multiple cooling simulations along different isobars.

From these, an increase of nematic stability upon increasing the pressure was observed which is similar to results obtained for Gay-Berne systems with similar well depth ratios. The results also confirmed, that the soft-core models are not universally as nice as the Gay-Berne or the Gay-Berne-Kihara models, due to unphysical particle overlaps at high densities. As a second test case, the new model was used as the mesogenic part of a coarse grained multipedal liquid crystalline molecule. Bulk simulations of, $N = 125$, of these molecules showed spontaneous self-assembly of a smectic A phase over approximately 30 hours of simulation time on a single processor computer. Further, these simulation demonstrated that there exists a strong coupling between the structure of the phase itself and structure of the individual molecule; such that the molecules adopt a rod-like shape on the transition to the ordered mesophase.

Chapter 4 demonstrated two different applications of the new potential model. In the first case, the new spherocylinder model was used as the mesogenic unit of a main chain liquid crystalline polymer. This model allowed relatively quick equilibration and control over the volume occupied by the rigid mesogenic unit by varying the spherocylinder elongation, L/D. Molecular dynamics simulations were used to map out an approximate phase diagram in constant occupied volume fraction as a function of the rod volume fraction. The results obtained, demonstrated a rich phase behaviour with a large area of lamellar stability for approximately equal volume fractions for the rods and coils. In going from longer rods to shorter, the following sequence of phases was observed: nematic-lamellar-gyroid-lamellar with cylindrical micelles, for very short rods.

Chiral induction was studied in the second part of chapter 4. Here, a minimal computationally efficient model with control over conformational chirality was developed from three connected anisotropic building blocks, modelled by the new spherocylinder model. When flexible achiral dopant molecules were used as a solute in a chiral nematic host phase, the results showed a preferential selection of dopant conformations with a “molecular” twist in the same direction as the host phase. Moreover, the results demonstrated that the preferential selection of chiral conformations can lead to an increase in the bulk twist of the host phase. Thus, helping to explain the experimental findings of Thisayukta *et al.* [193] that an achiral dopant can increase the twist of a bulk chiral phase. In addition, evidence of chiral segregation of domains with left and right handed conformations was observed in an achiral nematic phase. These results benefitted from the exceptionally good sampling of chiral conformations provided by the use of the new soft core simulation model developed in the course of this research project.

A Stochastic Rotational Dynamics (SRD) solvent was coupled with a simple coarse grained surfactant model in chapter 5. This allowed for a relatively cheap model for solvent-solvent interactions, while still maintaining the correct hydrodynamics. Simulation of model surfactants solvated in the "phantom" SRD solvent, showed a spontaneous self-assembly of a bilayer and spherical micelles. The average micelle size was studied as a function of the solvent quality, controlled by altering the attraction between the hydrophilic head beads and the solvent beads. The results demonstrated an increase in the average number of monomers per micelle when the the attraction between the head bead and solvent was reduced. The calculations of micelle size distributions as a function of time, revealed that the size distribution can evolve over time, despite the lack of small aggregation number aggregates. This result, suggests that there exists a secondary process for micelle growth in addition to the addition of a single monomer. One such process, namely merger of two micelles into a fairly large supermicelle, was directly observed in the simulations.

In chapter 6, a relatively new simulation methodology, Statistical Temperature Molecular Dynamics (STMD) developed recently by Kim *et. al.* [76], was introduced. STMD effectively combines the Wang-Landau Monte Carlo method with Multi-Canonical molecular dynamics, in such a way that the weights needed to integrate the equations of motions are constructed on the fly. STMD was applied to the isotropic-nematic phase transition of a single site system and to the isotropic-lamellar phase transition of a model rod-coil diblock copolymer melt. In both cases, the STMD simulations were compared to conventional molecular dynamics simulations. The results showed very good agreement. The advantages of the STMD method are that the convergent simulations show the true phase behaviour of the system for the simulated temperature range for very high precision, and the thermodynamic quantities, such as the entropy and the free energy, are readily available. Interestingly, the STMD simulations of the rod-coil diblock copolymer melt, suggested that there exists not one, but two separate first-order like phase transitions. It could be speculated, that *if* this is indeed true, the mechanism of the isotropic-lamellar phase transition could consist of two separate process with the likely candidates being, phase separation and orientational ordering of the rods. Further, this behaviour should be true for many more if not all the rod-coil systems going through an isotropic-lamellar phase transition. If system of flag poles tethered with chain of footballs would exhibit isotropic-lamellar phase transition, it should occur the same way.

Finally in chapter 7, a Hamiltonian Replica Exchange Molecular Dynamics (HREMD) simulation of soft-core Gay-Berne potential was presented. These results showed up to an order of magnitude speed up in equilibration of the nematic phase when compared to conventional simulations of the Gay-Berne potential.

Overall, the studies presented here, demonstrate that meaningful results can be achieved using highly coarse grained models, provided that the problem and model are formulated sensibly. The work here points towards many interesting suggestions for future studies.

The new anisotropic soft core potential of chapters 3 and 4 is efficient to simulate. Consequently, there are number of interesting soft matter systems which would be beneficial to study using it. In particular, it may be useful for CG simulations of biological systems (for example proteins and membranes), where interesting phenomena occur at large time and length scales. It may may also be very useful for further studies of liquid crystalline polymers and dendrimers, where equilibration of existing models is very difficult to achieve.

The SRD model used in chapter 5 is also computationally efficient. Further studies of large systems of amphiphiles would be interesting, in terms of studying the time scales involved in the formation of self-assembled structures, such as micelles and vesicles. To obtain reliable results for the kinetics, several independent simulations would need to be performed. There exists also a number of interesting non-equilibrium phenomena, such as the fusion of two vesicles or pore formation in membranes, which are very difficult to study via conventional simulations because of the time scale issues.

The STMD simulation technique is very new, but the results in chapter 6 suggest that it may be possible to use this strategy in further CG studies of soft matter systems. One very interesting possibility would be to test the replica exchange statistical temperature Monte Carlo [248], developed this year by the original authors of the STMD method, to self-assembling soft matter systems. Another possible extension, to what has been presented here, would be to try to combine the STMD work of chapter 6 with the HREMD strategy of chapter 7. The combination of the highly efficient simulation model (chapters 3 and 4) and two advanced simulation methodologies (chapters 6 and 7) could make a major difference to the future of soft matter modelling; making it possible to study systems and problems which have so far proved inaccessible to CG simulations.

Lastly, the chirality results presented in chapter 4 are of fundamental interest. Further studies of chirality transfer in chiral systems would be possible using the model of chapters 3 and 4. Also, of an interest here are suggestions of chiral segregation into large scale chiral domains of opposite handedness in nematic phase formed by achiral bent-core molecules.

Bibliography

[1] X. Li, J. Guo, Y. Liu, and H. Liang, J. Chem. Phys. **130**, 074908 (2009).

[2] J. Goodby, G. Mehl, I. Saez, R. Tuffin, G. Mackenzie, R. Auzely-Velty, T. Benvegnu, and D. Plusquellec, Chem. Comm. **19**, 2057 (1998).

[3] A. T. Gabriel, T. Meyer, and G. Germano, J. Chem. Theory Comput. **4**, 468 (2008).

[4] R. Berardi, A. P. J. Emerson, and C. Zannoni, J. Chem. Soc., Faraday Trans. **89**, 4069 (1993).

[5] G. R. Luckhurst, R. A. Stephens, and R. W. Phippen, Liq. Cryst. **8**, 451 (1990).

[6] F. Jensen, *Introduction to Computational Chemistry*, chapter 14. 2nd edition (Wiley, 2007).

[7] P. G. de Gennes, *The physics of liquid crystals*, chapter 1 (Oxford University Press, 1974).

[8] P. G. de Gennes and J. Prost, *The physics of liquid crystals*, chapter 1 (Oxford University Press, 1993).

[9] C. M. Care and D. J. Cleaver, Rep. Prog. Phys. **68**, 2665 (2005).

[10] R. A. L. Jones, *Soft Condensed Matter.* (Oxford University Press, 2002).

[11] T. A. Witten and P. A. Pincus, *Structured Fluids.* (Oxford University Press, 2004).

[12] M. W. Matsen and C. Barrett, J. Chem. Phys. **109**, 4108 (1998).

[13] G. Friedel, Ann. Physique **18**, 273 (1922).

[14] L. A. Madsen, T. J. Dingemans, and M. Nakata, Phys. Rev. Lett. **92**, 145505 (2004).

[15] K. S. Acharya BR, Primak A, Phys. Rev. Lett. **92**, 145506 (2004).

[16] V. J. Merkel K, Kocot A, Phys. Rev. Lett. **93**, 237801 (2004).

[17] F. C. Bawden, N. W. Pirie, J. D. Bernal, and I. Fankuchen, Nature (London) **138**, 1051 (1936).

[18] E. Grelet and S. Fraden, Phys. Rev. Lett. **90**, 198302 (2003).

[19] M. Baron, Pure Appl. Chem. **73**, 845 (2001).

[20] D. Stewart and C. T. Imrie, J. Mater. Chem. **5**, 223 (1995).

[21] K. Lorenz, D. Hoter, B. Stuhn, R. Mulhaupt, and H. Frey, Adv. Mat. **8**, 414 (1996).

[22] C. Z. Cai and Z. U. Chen, Macromolecules **30**, 5104 (1997).

[23] S. Bauer, H. Fischer, and H. Ringsdorf, Angew. Chem. Int. Ed. Engl. **32**, 1589 (1993).

[24] I. Saez and J. Goodby, Liq. Cryst. **26**, 1101 (1999).

[25] K. Yonetake, K. Suzuki, T. Morishita, R. Nagahata, and M. Ueda, High Perform. Poly. **10**, 373 (1998).

[26] V. Percec, G. Johansson, D. Schlueter, J. Ronda, and G. Ungar, Macromol. Symp. **101**, 43 (1996).

[27] H. Meier and M. Lehmann, Angew. Chem. Int. Ed. **37**, 643 (1998).

[28] J. Cameron, A. Facher, G. Latterman, and S. Diele, Adv. Mater. **9**, 398 (1997).

[29] M. A. Perez, E. Longo, and C. A. Taft, Theochem-J. Mol. Struct. **507**, 97 (2000).

[30] I. Saez and J. Goodby, J. Mater. Chem. **15**, 26 (2005).

[31] I. Saez and J. Goodby, J. Mater. Chem. **11**, 2845 (2001).

[32] L. M. Stimson and M. R. Wilson, J. Chem. Phys. **123**, 034908 (2005).

[33] L. Cavallo and F. Fraternali, Chem. Eur. J. **4**, 927 (1998).

[34] T. Cagin, G. F. Wang, R. Martin, G. Zamanakos, N. Vaidehi, D. T. Mainz, and W. A. Goddard, Comput. Theor. Polym. Sci. **11**, 345 (2001).

[35] K. Karatasos, D. B. Adolf, and G. R. Davies, J. Chem. Phys. **115**, 5310 (2001).

[36] Z. E. Hughes, M. R. Wilson, and L. M. Stimson, Soft Matter **1**, 436 (2005).

[37] D. Chandler, *Introduction to Modern Statistical Mechanics.* (Oxford University Press, 1987).

[38] P. Huang and E. A. Carter, Annu. Rev. Phys. Chem. **59**, 261 (2008).

[39] M. Kalweit and D. Drikakis, J. Comput. Theor. Nanosci. **5**, 1923 (2008).

[40] M. McCullagh, T. Prytkova, S. Tonzani, N. D. Winter, and G. C. Schatz, J. Phys. Chem. B. **112**, 10388 (2008).

[41] M. P. Allen and D. J. Tildesley, *Computer Simulation of Liquids.* (Oxford University Press, 1989).

[42] M. L. Klein and W. Shinoda, Science **321**, 798 (2008).

[43] J. G. Gay and B. J. Berne, J. Chem. Phys. **74**, 3316 (1981).

[44] C. M. Care and D. J. Cleaver, Rep. Prog. Phys. **68**, 2665 (2005).

[45] M. P. Allen and D. J. Tildesley, *Computer Simulation of Liquids*, chapter 1 (Oxford University Press, Oxford, 1987).

[46] M. R. Wilson, Chem. Soc. Rev. **36**, 1881 (2007).

[47] P. A. Lebwohl and G. Lasher, Phys. Rev. A **6**, 426 (1972).

[48] G. R. Luckhurst, R. A. Stephens, and R. W. Phippen, Liq. Cryst. **8**, 451 (1990).

[49] G. Luckhurst, P. Simpson, and C. Zannoni, Liq. Cryst. **2**, 313 (1987).

[50] M. A. Bates and G. R. Luckhurst, J. Chem. Phys. **110**, 7087 (1999).

[51] E. J. de Miguel, E. M. del Rio, and F. J. Blas, J. Chem. Phys. **121**, 11183 (2004).

[52] I. M. Withers, C. M. Care, and D. J. Cleaver, J. Chem Phys **113**, 5078 (2000).

[53] A. P. J. Emerson, G. R. Luckhurst, and S. G. Whatling, Mol. Phys. **82**, 113 (1994).

[54] M. A. Bates and G. R. Luckhurst, J. Chem. Phys. **104**, 6696 (1996).

[55] J. Vieillard-Baron, Molec. Phys. **28**, 809 (1974).

[56] S. C. McGrother, D. C. Williamson, and G. Jackson, J. Chem. Phys. **104**, 6755 (1996).

[57] P. Bolhuis and D. Frenkel, J. Chem. Phys **106**, 666 (1997).

[58] K. M. Aoki and T. Akiyama, Molec. Cryst. Liq. Cryst. **299**, 45 (1997).

[59] D. J. Earl and M. R. Wilson, J. Mater. Chem. **11**, 2672 (2001).

[60] Z. E. Hughes, L. M. Stimson, H. Slim, J. S. Lintuvuori, J. M. Ilnytskyi, and M. R. Wilson, Comp. Phys. Comm. **178**, 724 (2008).

[61] D. Frenkel and B. M. Mulder, Phys. Rev. Lett. **52**, 287 (1984).

[62] O. Hahn, L. D. Site, and K. Kremer, Macromol. Theory Simul. **10**, 288 (2001).

[63] L. Paramonov and S. N. Yaliraki, J. Chem. Phys. 194111 (2005).

[64] S. C. McGrother, D. C. Williamson, and G. Jackson, J. Chem. Phys. **104**, 6755 (1996).

[65] J. Vieillard-Baron, J. Chem. Phys. **56**, 4729 (1972).

[66] D. J. Earl, J. Ilnytskyi, and M. R. Wilson, Mol. Phys. **99**, 1719 (2001).

[67] B. Martinez-Haya, A. Cuetos, S. Lago, and L. F. Rull, J. Chem. Phys. **122**, 24908 (2005).

[68] D. Frenkel and B. Smit, *Understanding Molecular Simulations: From Algorithms to Applications, 2nd edition.* (Academic Press, 2001).

[69] N. Metropolis, A. W. Rosenbluth, M. N. Rosenbluth, A. H. Teller, and E. Teller, J. Chem. Phys. **21**, 1087 (1953).

[70] M. I. Manousiouthakis and M. W. Deem, J. Chem. Phys. **110**, 2753 (1999).

[71] D. C. Rapaport, *The Art of Molecular Dynamics Simulation*, chapter 1 (Cambridge Univeristy Press, 1995).

[72] M. P. Allen and D. J. Tildesley, *Computer Simulation of Liquids*, chapter 3 (Oxford University Press, Oxford, 1987).

[73] L. Verlet, Phys. Rev. **159**, 98 (1967).

[74] W. Swope, H. C. Andersen, P. H. Berens, and K. R. Wilson, J. Chem. Phys. **76**, 637 (1982).

[75] J. Ilnytskyi and M. R. Wilson, Comp. Phys. Comm. **148**, 43 (2002).

[76] J. Kim, J. E. Straub, and T. Keyes, Phys. Rev. Lett. **97**, 050601 (2006).

[77] Y. Sugita, A. Kitao, and Y. Okamoto, J Chem. Phys. **113**, 6042 (2000).

[78] H. Fukunishi, O. Watanabe, and S. Takada, J. Chem. Phys. **116**, 9058 (2002).

[79] H. J. C. Berendsen, J. P. M. Postma, W. F. VanGunsteren, A. DiNola, and J. R. Haak, J. Chem. Phys. **81**, 3684 (1984).

[80] H. Andersen, J. Chem. Phys. **72**, 2384 (1980).

[81] W. G. Hoover, Phys. Rev. A **31**, 1695 (1985).

[82] S. Toxvaerd, Phys. Rev. E **47**, 343 (1993).

[83] P. Hoogerbrugge and J. Koelman, **19**, 155 (1992).

[84] I. Vattulainen, M. Karttunen, G. Besold, and J. M. Polson, J. Chem. Phys. **116**, 3967 (2002).

[85] C. Lowe, Europhys. Lett. **47**, 145 (1999).

[86] P. Espanol and P. Warren, Europhys. Lett. **30**, 191 (1995).

[87] P. Nikunen, M. Karttunen, and I. Vattulainen, Comp. Phys. Comm. **153**, 407 (2003).

[88] M. P. Allen, J. Phys. Chem. B **110**, 3823 (2006).

[89] E. A. Koopman and C. P. Lowe, J. Chem. Phys. **124**, 204103 (2006).

[90] S. D. Stoyanov and R. D. Groot, J. Chem. Phys. **122**, 114112 (2005).

[91] M. P. Allen and F. Schmid, Mol. Sim. **33**, 21 (2007).

[92] A. Malevanets and R. Kapral, J. Chem. Phys. **110**, 8605 (1999).

[93] T. Ihle and D. M. Kroll, Phys. Rev. E. **63**, 020201 (2001).

[94] T. Ihle and D. M. Kroll, Phys. Rev. E. **67**, 066705 (2003).

[95] T. Ihle and D. M. Kroll, Phys. Rev. E. **67**, 066706 (2003).

[96] K. Mussawisade, M. Ripoll, R. G. Winkler, and G. Gompper, J. Chem. Phys. **123** (2005).

[97] I. Ali and J. Yeomans, J. Chem. Phys. **123**, 234903 (2005).

[98] N. Watari, M. Makino, R. G. Kikuchi, R. G. Larson, and M. Doi, J. Chem. Phys. **126**, 094902 (2007).

[99] A. Malevanets and R. Kapral, J. Chem. Phys. **112**, 7260 (2000).

[100] J. T. Padding and A. A. Louis, Phys. Rev. E **74** (2006).

[101] M. R. Wilson, Journal of Molecular Liquids **68**, 23 (1996).

[102] M. P. Allen and D. J. Tildesley, *Computer Simulation of Liquids*, chapter 2 (Oxford University Press, Oxford, 1987).

[103] M. R. Wilson, J. Chem. Phys. **107**, 8654 (1997).

[104] C. McBride and M. R. Wilson, Molec. Phys. **97**, 511 (1999).

[105] D. L. Cheung, S. J. Clark, and M. R. Wilson, Phys. Rev. E **65**, 051709 (2002).

[106] C. Peter, L. Delle site, and K. Kremer, Soft Matter **4**, 859 (2008).

[107] R. Faller, Polymer **45**, 3869 (2004).

[108] H. Fukunaga, J. Takimoto, and M. Doi, J. Chem. Phys. **116**, 8183 (2002).

[109] D. Reith, M. Putz, and F. Muller-Plathe, J. Comput. Chem **24**, 1624 (2003).

[110] G. Milano, S. Goudeau, and F. muller plathe, J. polym. Sci. Part B: Polym. Phys. **43**, 871 (2005).

[111] J.-P. Hansen, C. I. Addison, and A. A. Louis, J. Phys.: Condens. Matter **17**, 3185 (2005).

[112] F. Muller-Plathe, Chem. Phys. Chem. **3**, 754 (2002).

[113] H. Gohlke and M. F. Thorpe, Biophys. J. **91**, 2115 (2006).

[114] F. Jensen, *Introduction to Computational Chemistry*, chapter 13. 2$^{\text{nd}}$ edition (Wiley, 2007).

[115] P. G. Bolhuis, A. A. Louis, J. P. Hansen, and E. J. Meijer, J. Chem. Phys. **114**, 4296 (2000).

[116] X. Guerrault, B. Rousseau, and J. Farago, J. Chem. Phys. **121**, 6538 (2004).

[117] R. D. Groot and T. J. Madden, J. Chem. Phys. **108**, 8713 (1998).

[118] F. J. Martinez-Veracoechea and F. A. Escobedo, J. Chem. Phys. **125**, 104907 (2006).

[119] F. J. Martinez-Veracoechea and F. A. Escobedo, Macromolecules **40**, 7354 (2007).

[120] Z. L. Zhang, M. A. Horsch, M. H. Lamm, and S. Glotzer, Nano Letters **3**, 1341 (2003).

[121] M. A. Horsch, Z. L. Zhang, and S. C. Glotzer, Phys. Rev. Lett. **95**, 056105 (2005).

[122] M. A. Horsch, Z. Zhenli, and S. C. Glotzer, J. Chem. Phys. **125**, 184903 (2006).

[123] M. A. Horsch, Z. L. Zhang, and S. C. Glotzer, Nano Lett. **6**, 2406 (2006).

[124] T. D. Nguyen, Z. L. Zhang, and S. C. Glotzer, J. Chem. Phys. **129**, 244903 (2008).

[125] D. J. Hong, E. Lee, H. Jeong, J. Lee, W. C. Zin, T. D. Nguyen, S. C. Glotzer, and M. Lee, Angew. Chem. Int. Ed. **48**, 1664 (2009).

[126] C. M. Care and D. J. Cleaver, Rep. Prog. Phys. **68**, 2665 (2005).

[127] M. R. Wilson, Int. Rev. Phys. Chem. **24**, 421 (2005).

[128] M. R. Wilson, Chem. Soc. Rev. **36**, 1881 (2007).

[129] M. A. Bates and G. R. Luckhurst, In *Structure and Bonding: Liquid Crystals*, edited by M. Mingos (Springer-Verlag, Heidelberg, 1999).

[130] M. R. Wilson and M. P. Allen, Molec. Phys. **80**, 277 (1993).

[131] G. V. Paolini, G. Ciccotti, and M. Ferraro, Molec. Phys. **80**, 297 (1993).

[132] A. Cuetos, B. Martinez-Haya, L. F. Rull, and S. Lago, J. Chem. Phys. **117**, 2934 (2002).

[133] D. Williamson and F. del Rio, J. Chem. Phys. **109**, 4675 (1998).

[134] D. Williamson and Y. Guevara, J. Phys. Chem. B **103**, 7522 (1999).

[135] M. S. Al-Barwani and M. P. Allen, Phys. Rev. E **62**, 6706 (2000).

[136] A. Cuetos, B. Martinez-Haya, and S. Lago, Phys. Rev. E **68**, 011704 (2003).

[137] M. R. Wilson, J. Chem. Phys. **107**, 8654 (1997).

[138] H. Steuer, S. Hess, and M. Schoen, Physica A **328**, 322 (2003).

[139] M. P. Allen and G. Germano, Mol. Phys. **104**, 3225 (2006).

[140] C. Vega and S. Lago, Computers Chem. **18**, 55 (1994).

[141] M. P. Allen and D. L. Tildesley, *Computer simulation of liquids*, chapter Appendix B (Oxford University Press, Oxford, 1987).

[142] J. M. Ilnytskyi and M. R. Wilson, Comput. Phys. Comm. **148**, 43 (2002).

[143] A. Cuetos, J. M. Ilnytskyi, and M. R. Wilson, Mol. Phys. **100**, 3839 (2002).

[144] E. de Miguel, E. M. del Rio, J. T. Brown, and M. P. Allen, J. Chem. Phys. **105**, 4234 (1996).

[145] B. Martínez-Haya and A. Cuetos, J. Phys. Chem. B. **111**, 8150 (2007).

[146] E. de Miguel, E. M. del Rio, J. T. Brown, and M. P. Allen, J. Chem. Phys. **105**, 4234 (1996).

[147] A. J. Vanakaras and D. J. Photinos, J. Mater. Chem. **15**, 2002 (2005).

[148] V. Percec, P. W. Chu, G. Ungar, and J. P. Zhou, J. Am. Chem. Soc. **117**, 11441 (1995).

[149] S. A. Ponomarenko, N. I. Boiko, V. P. Shibaev, R. M. Richardson, I. J. Whitehouse, E. A. Rebrov, and A. M. Muzafarov, Macromolecules **33**, 5549 (2000).

[150] M. R. Wilson, J. M. Ilnytskyi, and L. M. Stimson, J. Chem. Phys. **119**, 3509 (2003).

[151] I. W. Hamley, *The Physics of Block Copolymers.* (Oxford University Press, Oxford, 1998).

[152] M. W. Matsen, J. Phys.-Cond. Mat. **14**, R21 (2002).

[153] A. Al Sunaidi, W. K. Den Otter, and J. H. R. Clarke, Phil. Trans. Roy. Soc. London A **362**, 1773 (2004).

[154] F. J. Martinez-Veracoechea and F. A. Escobedo, Macromolecules **38**, 8522 (2005).

[155] F. J. Martínez-Veracoechea and F. A. Escobedo, Macromolecules **42**, 1775 (2009).

[156] B. D. Olsen and R. A. Segalman, Mat. Sci. Eng. R Rep. **62**, 37 (2008).

[157] C. L. Chochos, J. K. Kallitsis, and V. G. Gregoriou, J. Phys. Chem. B **109**, 8755 (2005).

[158] H. C. Lin, K. W. Lee, C. M. Tsai, and K. H. Wei, Macromolecules **39**, 3808 (2006).

[159] L. L. Qiang, Z. Ma, Z. Zheng, R. Yin, and W. Huang, Macromolecular Rapid Communications **27**, 1779 (2006).

[160] X. Yang and J. Loos, Macromolecules **40**, 1353 (2007).

[161] Y. R. Yoon, Y. B. Lim, E. Lee, and M. Lee, Chem. Comm. 1892–1894 (2008).

[162] H. M. Konig and A. F. M. Kilbinger, Angewandte Chemie-International Edition **46**, 8334 (2007).

[163] J. T. Chen, E. L. Thomas, C. K. Ober, and S. S. Hwang, Macromolecules **28**, 1688 (1995).

[164] J. T. Chen, E. L. Thomas, C. K. Ober, and G. P. Mao, Science **273**, 343 (1996).

[165] J. Song, T. F. Shi, Y. Q. Li, J. Z. Chen, and L. J. An, J. Chem. Phys. **129**, 054906 (2008).

[166] M. Lee, B. K. Cho, H. Kim, J. Y. Yoon, and W. C. Zin, J. Am. Chem. Soc. **120**, 9168 (1998).

[167] J. E. Yang, S. Samal, T. Higashihara, K. Sugiyama, N. Haraguchi, A. Matsuo, A. Hirao, and J. S. Lee, Macromolecules **39**, 3038 (2006).

[168] J. M. Ilnytskyi and M. R. Wilson, Comput. Phys. Comm. **134**, 23 (2001).

[169] M. R. Wilson, J. Chem. Phys. **107**, 8654 (1997).

[170] M. A. Horsch, Z. L. Zhang, and S. C. Glotzer, Phys. Rev. Lett. **95**, 056105 (2005).

[171] J. Z. Chen, Z. Y. Sun, C. X. Zhang, L. J. An, and Z. Tong, J. Chem. Phys. **128** (2008).

[172] A. Lyulin, M. Al-Barwani, M. Allen, M. Wilson, I. Neelov, and N. Allsopp, Macromolecules **31**, 4626 (1998).

[173] R. Berardi, D. Micheletti, L. Muccioli, M. Ricci, and C. Zannoni, J. Chem. Phys. **121**, 9123 (2004).

[174] V. Pryamitsyn and V. Ganesan, J. Chem. Phys. **120**, 5824 (2004).

[175] J. Z. Chen, C. X. Zhang, Z. Y. Sun, L. J. An, and Z. Tong, J. Chem. Phys. **127**, 024105 (2007).

[176] P. Wang, Z. Ma, Y. L. Yang, Q. L. Fan, X. F. Yu, C. Wang, W. Huang, and L. H. Wang, Phys. Chem. Chem. Phys **11**, 167 (2009).

[177] D. C. Wright and N. D. Mermin, Rev. Mod. Phys. **61**, 385 (1989).

[178] E. Grelet, B. Pansu, M.-H. Li, and H. T. Nguyen, Phys. Rev. E. **65**, 050701 (2002).

[179] J. W. Goodby, M. A. Waugh, S. M. Stein, E. Chin, R. Pindak, and J. S. Patel, Nature **337**, 449 (1989).

[180] D. H. Van Winkle, M. W. Davidson, X. W. Chen, and R. L. Rill, Macromolecules **23**, 4140 (1990).

[181] F. Tombolato, A. Ferrarini, and E. Grelet, Phys. Rev. Lett. **96**, 258302 (2006).

[182] S. Tomar, M. M. Green, and L. A. Day, J. Am. Chem. Soc. **129**, 3367 (2007).

[183] Z. Dogic and S. Fraden, Curr. Opin. Colloid. Interface Sci. **11**, 47 (2006).

[184] R. Memmer, H. G. Kuball, and A. Schonhofer, Liq. Cryst. **15**, 345 (1993).

[185] M. P. Allen and A. J. Masters, Mol. Phys. **79**, 277 (1993).

[186] M. P. Allen and A. J. Masters, J. Mater. Chem. **11**, 2678 (2001).

[187] G. Germano, M. P. Allen, and A. Masters, J. Chem. Phys. **116**, 9422 (2002).

[188] M. R. Wilson and D. J. Earl, J. Mater. Chem. **11**, 2672 (2001).

[189] R. Berardi, H.-G. Kuball, R. Memmer, and C. Zannoni, J. Chem. Soc. Faraday Trans. **94**, 1229 (1998).

[190] S. Varga and G. Jackson, Chem. Phys. Lett. **377**, 6 (2003).

[191] M. Ricci, M. Mazzeo, R. Berardi, P. Pasini, and C. Zannoni, Faraday Discuss. **144** (2010).

[192] H. H. Wensink and G. Jackson, J. Chem. Phys. **130**, 234911 (2009).

[193] J. Thisayukta, H. Niwano, H. Takezoe, and J. Watanabe, J. Am. Chem. Soc. **124**, 3354 (2002).

[194] D. Earl, M. Osipov, H. Takezoe, Y. Takanishi, and M. Wilson, Phys. Rev. E. **71**, 021706 (2005).

[195] V. Gortz, C. Southern, N. W. Roberts, H. F. Gleeson, and J. W. Goodby, Soft Matter **5**, 463 (2009).

[196] M. A. Hillmyer, Science **317**, 604 (2007).

[197] S. R. Euston, Curr. Opin. Colloid Interface Sci. **9**, 321 (2004).

[198] M. Venturoli, M. M. Sperotto, M. Kranenburg, and B. Smit, Physics Reports **437**, 1 (2006).

[199] P. J. Bond, J. Holyoake, A. Ivetac, S. Khalid, and M. S. P. Sansom, Journal of Structural Biology **157**, 593 (2007).

[200] R. Pool and P. G. Bolhuis, J. Phys. Chem. B **109**, 6650 (2005).

[201] R. Pool and P. G. Bolhuis, Phys. Chem. Chem. Phys. **8**, 941 (2006).

[202] R. Pool and P. G. Bolhuis, J. Chem. Phys. **126**, 244703 (2007).

[203] R. Pool and P. G. Bolhuis, Phys. Rev. Lett. **97**, 018302 (2006).

[204] G. Mohan and D. I. Kopelevich, J. Chem. Phys. **128** (2008).

[205] M. Venturoli and B. Smit, Phys. Chem. Comm. **10**, 45 (1999).

[206] J. D. Revalee, M. Laradji, and P. B. S. Kumar, J. Chem. Phys. **128**, 035102 (2008).

[207] O. Lenz and F. Schmid, J. Mol. Liq. **117**, 147 (2005).

[208] F. Schmid, D. Düchs, O. Lenz, and B. West, Comp. Phys. Comm. **177**, 168 (2007).

[209] D. Düchs and F. Schmid, J. Phys. Condens. Matter **13**, 4853 (2001).

[210] O. Lenz and F. Schmid, Phys. Rev. Lett. **98**, 058104 (2007).

[211] J. D. Weeks, D. Chandler, and H. C. Andersen, J. Chem. Phys. **12**, 5237 (1971).

[212] M. Kranenburg and B Smit, J. Phys. Chem. B **109**, 6553 (2005).

[213] R. Goetz and R. J. Lipowsky, J. Chem. Phys. **108**, 7397 (1998).

[214] R. Goetz, G. Gompper, and R. J. Lipowsky, Phys. Rev. Lett. **82**, 221 (1999).

[215] M. Jorge, Langmuir **24**, 5714 (2008).

[216] D. M. Colegate and C. D. Bain, Phys. Rev. Lett. **95**, 198302 (2005).

[217] A. M. Ferrenberg and R. H. Swendsen, Phys. Rev. Lett. **63**, 1195 (1989).

[218] S. Kumar, D. Bouzida, R. H. Swendsen, P. A. Kollman, and J. M. Rosenberg, J. Comp. Chem. **13**, 1011 (1992).

[219] A. P. Lyubartsev, A. A. Martsinovski, S. V. Shevkunov, and P. N. Vorontsov-Velyaminov, J. Chem. Phys. **96**, 1776 (1992).

[220] Y. Sugita and Y. Okamoto, Chem. Phys. Lett. **314**, 141 (1999).

[221] C. R. A. Abreu and F. A. Escobedo, J. Chem. Phys. **124**, 054116 (2006).

[222] B. A. Berg and T. Neuhaus, Phys. Lett. B **267**, 249 (1991).

[223] J. Lee, Phys. Rev. Lett. **71**, 211 (1993).

[224] F. Wang and D. P. Landau, Phys. Rev. Lett. **86**, 2050 (2001).

[225] Q. Yan, R. Faller, and J. J. de Pablo, J. Chem. Phys. **116**, 8745 (2002).

[226] M. S. Shell, P. G. Debenedetti, and Z. Panagiotopoulus, Phys. Rev. E **66**, 056703 (2002).

[227] Q. Yan, T. S. Jain, and J. J. de Pablo, Phys. Rev. Lett. **92**, 235701 (2004).

[228] N. Rathore, T. A. Knotts IV, and J. J. de Pablo, J. Chem. Phys. **118**, 4285 (2003).

[229] N. Rathore and J. J. de Pablo, J. Chem. Phys. **116**, 7225 (2002).

[230] V. Varshney and G. A. Carri, Phys. Rev. Lett. **95**, 168304 (2005).

[231] G. Ganzenmüller and P. J. Camp, J. Chem. Phys. **127**, 154504 (2007).

[232] M. S. Shell, P. G. Debenedetti, and A. Z. Panagiotopoulos, J. Chem. Phys. **119**, 9406 (2003).

[233] D. Jayasri, V. S. S. Sastry, and K. P. N. Murthy, Phys. Rev. E **72**, 036702 (2005).

[234] P. Poulain, F. Calvo, R. Antoine, M. Broyer, and Ph. Dugourd, Phys. Rev. E **73**, 056704 (2006).

[235] Q. Yan and J. J. de Pablo, Phys. Rev. Lett. **90**, 035701 (2003).

[236] A. Tröster and C. Dellago, Phys. Rev. E **71**, 066705 (2005).

[237] U. H. E. Hansmann, Y. Okamoto, and F. Eisenmenger, Chem. Phys. Lett. **259**, 321 (1996).

[238] N. Nakajima, H. Nakamura, and A. Kidera, J. Phys. Chem. B **101**, 817 (1997).

[239] J. Kim, J. E. Straub, and T. Keyes, J. Chem. Phys. **126**, 135101 (2007).

[240] J. kim, J. E. Straub, and T. Keyes, Phys. Rev. E **76**, 011913 (2007).

[241] J. Kim and T. Keyes, J. Phys. Chem. B **112**, 954 (2007).

[242] E. J. Barth, B. B. Laird, and B. J. Leimkuhler, J. Chem. Phys. **118**, 5759 (2003).

[243] B. J. Schulz, K. Binder, M. Müller, and D. P. Landau, Phys. Rev. E **67**, 067102 (2003).

[244] P. Labastie and R. L. Whetten, Phys. Rev. Lett. **65**, 1567 (1990).

[245] D. J. Wales and R. S. Berry, Phys. Rev. Lett. **73**, 2875 (1994).

[246] C. Junghans, M. Bachmann, and W. Janke, Phys. Rev. Lett. **97**, 218103 (2006).

[247] V. Martin-Mayor, Phys. Rev. Lett. **98**, 137207 (2007).

[248] J. Kim, T. Keyes, and J. E. Straub, J. Chem. Phys. **130**, 124112 (2009).

[249] D. J. Earl and M. W. Deem, Phys. Chem. Chem. Phys. **7**, 3910 (2005).

[250] H. A. Slim and M. R. Wilson, J Chem. Theory Comput. **4**, 1570 (2008).

[251] P. Liu, B. Kim, R. A. Friesner, and B. J. Berne, Proc. Natl. Acad. Sci. **102**, 13749 (2005).

[252] R. Affentranger, I. Tavernelli, and E. E. Di Iorio, J. Chem. Theory Comput. **2**, 217 (2006).

[253] J. Hritz and C. Oostenbrink, J. Chem. Phys. **128**, 144121 (2008).

[254] H. J. C. Berendsen, J. P. M. Postma, W. F. van Gunsteren, A. DiNola, and J. R. Haak, J. Chem. Phys. **81**, 3684 (1984).